The Formation of Lenticular Galaxies in Nearby Clusters

Evelyn J. Johnston

The University of
Nottingham

UNITED KINGDOM · CHINA · MALAYSIA

Thesis submitted to the University of Nottingham
for the degree of Doctor of Philosophy, August 2014

Twinkle twinkle little star
How I wonder what you are

– Jane Taylor (1783–1824)

Supervisors:	Prof. Alfonso Aragón-Salamanca
	Prof. Michael Merrifield
Examiners:	Prof. Roger Davies *(University of Oxford)*
	Dr. Nina Hatch *(University of Nottingham)*

Abstract

Lenticular (S0) galaxies have long been thought of as evolved spirals, in which the star formation has been suppressed, the spiral arms have faded, and the luminosity of the bulge has been built up relative to the disc. However, the sequence of events that explains these three observations and leads to the formation of the final S0 galaxy is still uncertain.

The progenitor spirals generally consist of bulges with old stellar populations surrounded by young, bright discs. Therefore, in order to explain the 'quenching' of star formation in the disc and related increase in the bulge luminosity, an understanding of the individual star-formation histories of these two components is vital. In this thesis, we present a new technique to spectroscopically decompose the light from a galaxy into its bulge and disc components, from which the stellar populations and chemical compositions of the individual components can be extracted in order to determine the sequence of events leading to the transformation.

Using spectroscopic bulge–disc decomposition, the spatial light profile in a two-dimensional galaxy spectrum can be separated wavelength-by-wavelength into bulge and disc components. This decomposition allows the construction of separate one-dimensional spectra representing purely the light from the bulge and disc, enabling studies of their individual star-formation histories with minimal contamination. This technique was applied to a sample of 30 S0s in the Virgo and Fornax Clusters, and analysis of the absorption line strengths within these spectra reveals that the bulges contain consistently younger and more metal-rich

stellar populations than their surrounding discs. This result implies that the final episode of star formation before the progenitor spirals were fully quenched occurred in their central regions. Furthermore, the similarity in the α-element abundances of the bulges and discs indicates that the final episode of star formation in the bulge was fuelled using gas that has previously been chemically enriched in the disc. Together, these results present a picture in which the galaxy starts out as a typical spiral, with an old bulge surrounded by a young, star-forming disc. At some point in its life, gas is stripped from the galaxy, suppressing the star formation in the disc and causing the spiral arms to fade without inducing significant amounts of new star formation or disrupting the overall morphology of the galaxy. As the gas is removed, a fraction is also driven into the centre of the galaxy, where it fuels a final star-formation event in the bulge. This final episode of star formation consequently increases the luminosity of the bulge as the disc is already fading, and produces a central young, metal-rich stellar population.

We have also shown that it is possible to spectroscopically decompose a galaxy using the different line-of-sight velocity distributions of kinematically distinct components. This technique was applied to NGC 4550, an unusual S0 galaxy in the Virgo Cluster with two counter-rotating stellar discs and a gaseous disc, to separate their individual stellar populations. Analysis of these stellar populations shows that the disc that co-rotates with the ionized gas is brighter and has a significantly younger mean age than the other disc, which are consistent with more recent star formation fuelled by the associated gaseous material. Therefore, the most likely formation mechanism for this galaxy is via an unusual gas accretion or merger scenario that built up a secondary stellar disc in a pre-existing S0 galaxy.

The results presented in this thesis shed new light on the sequence of events that leads to the formation of S0 galaxies in cluster environments, and clearly demonstrates the importance of understanding the star-formation histories of the individual components within these galaxies in order to reconstruct the range of mechanisms by which they formed.

Published Work

Much of the work presented in this thesis has been published or will be published in the following four papers:

i) Johnston E. J., Aragón-Salamanca A., Merrifield M. R. & Bedregal A. G., 2012, *Spectroscopic bulge-disc decomposition: a new method to study the evolution of lenticular galaxies*, MNRAS, 422, 2590.

ii) Johnston E. J., Merrifield M. R., Aragón-Salamanca A. & Cappellari M., 2013, *Disentangling the stellar populations in the counter-rotating disc galaxy NGC 4550*, MNRAS, 428, 1296.

iii) Johnston E. J., Aragón-Salamanca A. & Merrifield M. R., 2014, *The origin of S0s in clusters: evidence from the bulge and disc star formation histories*, MNRAS, 441, 333.

iv) Bundy K., . . . Johnston E. J., *MaNGA: Mapping Nearby Galaxies at APO*, Submitted to ApJ.

Papers i and iii contain much of the work that is described in Chapters 2, 3 and 4, and the contents of Paper ii are described in Chapter 5. Finally, the initial proof of concept outlined in Chapter 6 will appear in Paper iv.

The work presented in this thesis was performed by the author, with advice from the coauthors listed above. Where the material is taken from the literature, this is mentioned explicitly in the relevant chapter.

Acknowledgements

There are a great many people without whom this work would never have been achieved. My first thanks must of course go to my supervisors, Mike and Alfonso, who have supported and guided me through my PhD for the last three and a half years. Without your knowledge, honesty and encouragement, I would never have achieved so much.

I must next thank my family, both in Northern Ireland and in England, for their continuous support and welcoming homes whenever I needed a break or a friendly face. In particular I need to thank my parents for always believing in me and making me believe that I can achieve my dreams if I work hard enough. And also my brother Greg for his absolute confidence that I was making groundbreaking discoveries every day, and his constant curiosity to know what the next project/discovery will be. Boris has also been amazing, with his constant support and friendship, and for always making me laugh when I've had a bad day. You've always known how to cheer me up and showed me how to keep everything in perspective.

My thanks also go to all the Nottingham people I've had the pleasure to meet and work alongside over the last few years. You all deserve a mention, but I especially want to thank Jamie, Cat, Sophie, Alice, Kate, Stuart, Nathan, Markus, Keith, Lyndsay, Kshitija, Berta, Carl, James, Lizzie, Fernando, Julian, Adam, Dimitri, Mattia, Bruno, Ismael, Hanni, Ana ... Without all of you, the Nottingham experience would have been a lot more dull and boring, and certainly less colourful (Alice!). I also want to thank everyone I have shared an office

with for your help, advice, interesting discussions, and for putting up with me talking away to myself in the corner. I especially want to thank Lizzie for keeping me sane while writing this thesis by displaying her own craziness – I will miss our toy car races and silly conversations. And I shouldn't forget the academic staff – Omar, Meghan, Frazer, Chris, Simon, Steven and Nina – for their useful comments and discussions over the years that have led to a deeper understanding of my results. And of course Mel and Jules for generally being amazing and always willing to help, and Phil who has rescued my computer on numerous occasions when I've done something stupid.

The Inflativerse has also been a big part of my life while I've been in Nottingham. Therefore, I want to acknowledge everyone who has helped with the project throughout the last three years to help build it up and keep it running, and especially Nina, Lizzie and James who have already taken over the project and will continue to make it a success after I leave.

I've also lived with some amazing people in Nottingham. Bruno, Angeles, Jole, Dimitri and Nick – if living with all of you has taught me anything, it's that not everything has to be done on time, and in fact life becomes a lot more fun when you live spontaneously. And of course my housemates when I first moved to Nottingham – Indie, Lavan, Prince, Hope and Bridget – who helped me settle into my new life here.

Finally, I should thank Nottingham and the STFC for the financial support they've provided me with throughout my PhD and in the coming months, ESO for giving me an incentive to finish by offering me an amazing job in Chile, and Andrew, Dave, Amy and Ismael for telling me all about living in Chile. I look forward to sharing some Chilean wine and pisco sours with you when I arrive in September.

Contents

List of Figures

List of Tables

The Formation of Lenticular

Galaxies in Nearby Clusters

Chapter 1

Introduction

Our knowledge of the Universe today has been built up over thousands of years as astronomers have looked at the sky and proposed theories to explain what they saw. The invention of the telescope in 1608 by Hans Lippershey proved revolutionary in our understanding of the Universe as astronomers could observe targets in the night sky in much more detail that can be achieved by the human eye. One of the most notable discoveries with the telescope is of course the orbits of the Galilean moons around Jupiter by Galileo Galilei, proving for the first time that the Earth was not at the centre of the Universe and that moons and planets could orbit around objects other than the Sun. Another early discovery was the presence of fuzzy nebulae by Charles Messier in the 17th Century, who recorded their positions to avoid misclassifying them as comets. Following the proposal by Thomas Wright (1750) that the Milky Way consisted of a flattened disc of stars, which would explain its appearance in the sky if the Sun was located within this disc, Immanuel Kant (1755) suggested that the fuzzy nebulae were really 'island universes' similar to the Milky Way if seen from the outside. In 1845, Lord Rosse resolved the spiral arms within these objects for the first time using a six-foot reflector, the "Leviathan of Parsonstown", thus introducing the idea of 'spiral nebulae' (Rosse, 1850). An example of one of Lord Rosse's early sketches of a spiral nebula is given in Fig. 1.1, alongside a recent photograph for

Figure 1.1: *Left:* a sketch of a spiral nebula, now known to be M51, by Lord Rosse in 1845. *Right:* a composite image of M51 taken in 2005 with the Advanced Camera for Surveys on the HST. Image credits: sketch- 'The Cambridge Illustrated History of Astronomy', (Hoskin, 1997); photograph- S. Beckwith (STScI) Hubble Heritage Team, (STScI/AURA), ESA, NASA.

comparison.

As astronomical techniques progressed, astronomers have continuously attempted to accurately measure the scale of the Universe, which would not only tell them about the size of the Milky Way, but also the distances to these nebulae. With this information, they would finally be able to determine whether the nebulae were huge objects outside of our own galaxy, or smaller objects within it. By 1921, this line of research had built up to the 'Great Debate' between Harlow Shapley and Heber Curtis on the scale of the Universe and nature of the nebulae (Shapley & Curtis, 1921).

Shapley argued on behalf of the traditional view that the Universe consists of only the Milky Way, and therefore that the nebulae were simply clouds of gas within our Galaxy. Part of his reasoning was based on the idea that if the nebulae were galaxies similar to the Milky Way, then the distances to these objects were just too large to accept. Shapley had already proposed a large size for the Milky Way using distance estimates to Cepheid variables in Galactic globular clusters,

in which he agreed with Wright (1750) that the Sun did not lie in the centre of the Galaxy (Shapley, 1917). As a result of this work, his calculations put the Andromeda galaxy at ~ 300 million light years away, as opposed to 2.5 million light years away that we measure today (Riess, Fliri & Valls-Gabaud, 2012). To explain the observed luminosity of the Andromeda galaxy if it truly lay at that distance required such a high value for its absolute magnitude that it was considered unbelievable for a galaxy to emit so much energy. Furthermore, a recent nova had been observed in the Andromeda galaxy that had temporarily outshone the nucleus of the galaxy. Given the incredible luminosity Shapley's calculations had attributed to this galaxy if it truly lay outside the Milky Way, he believed it was impossible for a nova to outshine it based on their understanding of physics at the time.

Curtis on the other hand argued on behalf of the island universe theory, placing the Sun at the centre of the Milky Way, which is a small galaxy similar to the spiral nebulae. Like Shapley, Curtis had made his own estimate for the size of the Milky Way. Using a simple star-counting technique, he had found that the Milky Way was significantly smaller than Shapley's estimate, meaning that the distances to the spiral nebulae, if they were galaxies like our own, would be much smaller and appeared more reasonable. Unlike Shapley however, Curtis placed the Sun at the centre of the galaxy. He also pointed out that more novae had been detected in the Andromeda nebula than in any other part of the sky, and then challenged opponents to explain the higher frequency of detections in that small part of the sky if the whole Universe consisted of one single galaxy with the Sun at the centre. He also assumed that the novae would have similar peak luminosities, meaning that their apparent magnitude at the brightest point could be used to measure their distances from the Earth. Using this technique he found that the distances to the novae detected in the Andromeda nebula were indeed larger than his estimate for the size of the Milky Way, and therefore that the spiral nebulae were other external galaxies.

After the debate, opinions were still divided between the two arguments. It

was only in 1926 that Edwin Hubble determined the true nature of the spiral nebulae, and thus settled the debate forever. By studying the periods of Cepheid variable stars in M33 and M31, he was able to determine the distances to these galaxies to be > 200 kpc and thus that they lay outside of the Milky Way (Hubble, 1926a, 1929). With this revelation, the field of extragalactic astronomy was born. Interestingly, although this result provided proof that Curtis was correct and that the Universe is made up of multiple galaxies like our own, Shapleys calculations on the size of our Galaxy were much closer to what we measure today, as was his conclusion that the Sun is not at the centre of the Milky Way.

1.1   Classification of Galaxy Morphology

1.1.1   The Hubble Sequence

Galaxies are now known to be massive structures made up of gravitationally bound stars, gas and dust, with typical masses of $\sim 10^7 - 10^{14}$ M$_\odot$ and sizes of $\sim 1 - 200$ kpc (Carroll & Ostlie, 1996). Even back in the 1920s it was clear that they had different structures, with some displaying magnificent spiral arms while others appeared featureless. In an early attempt to understand how these different structures were related, a classification system was proposed by Hubble (1926b, 1936) to separate galaxies into three main types, as shown in Fig. 1.2. On the left of the diagram are the featureless ellipticals – old, red-and-dead galaxies which have been disrupted at some point in their histories, leading to the stars following random orbits and giving the galaxy its characteristic ellipsoidal shape. These galaxies are typically classified as E0 to E7 based on their perceived flattening, where the exact classification is calculated using the ratio of the length of the minor axis to that of the major axis.

On the right of the Hubble sequence lie the spiral galaxies, split into two forks representing barred and unbarred spirals. These galaxies contain younger stellar populations and ongoing star formation within their discs that light up the
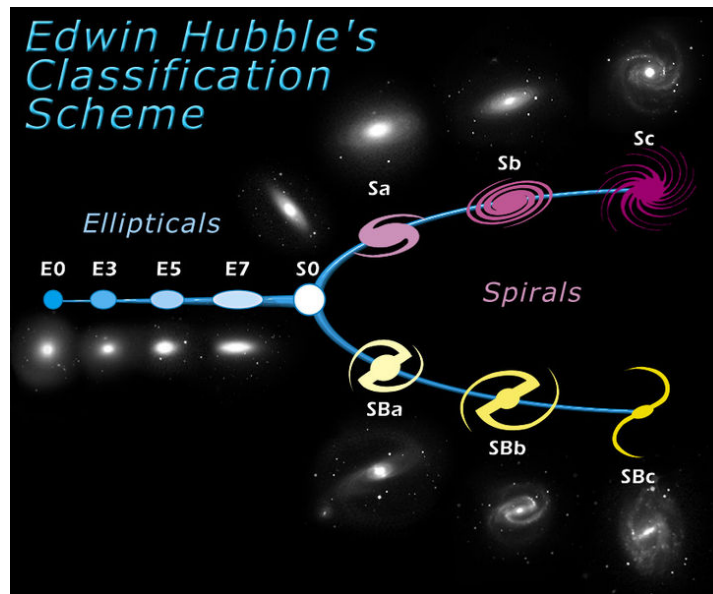
Figure 1.2: Galaxy morphology classification in the form of the Hubble sequence. Image credit: Space Telescope Science Institute

spiral arms. The spiral galaxies are further subdivided along the two forks into the Sa, Sb and Sc classes (SBa, SBb and SBc for barred spirals), where moving from Sc to Sa reflects an increase in the luminosity of the bulge relative to the disc and more tightly wound spiral arms. These variations within the spiral class can also be seen in Fig. 1.2.

The centre of the Hubble sequence, between the ellipticals and spirals, is home to the lenticular, or S0, class of galaxies. These galaxies share many of the observed properties of both ellipticals and spirals, such as the redder colours and old stellar populations of ellipticals, but with the discy morphology of spirals. As a result of these similarities, S0s were originally thought to be a transitional phase between simple-looking ellipticals and more complex spirals. Hubble (1926b) originally referred to ellipticals and S0s as early-type galaxies and spirals as late types, although it has now been determined that early type galaxies are dominated by late type stars while late type galaxies contain more early type stars. It was later stressed by Hubble (1927) that this sequence from elliptical to spiral morphologies was meant to be entirely empirical, with no implication for galaxy evolution theories. However, although it is now known that ellipticals generally

contain older stellar populations than spirals, and are thus at a later stage in their evolution, the terminology coined by Hubble has stuck.

The classification sequence proposed by Hubble (1926b) may appear simplistic in terms of the wealth of galaxy morphologies we have now observed, but it is still widely used today, forming the basis of the many variations suggested over the intervening years. Therefore, the longevity of this basic sequence suggests that it captures some basic truth about the different morphologies of galaxies.

1.1.2 The Evolution of Galaxy Classification Systems

The first significant change to the Hubble sequence was proposed by de Vaucouleurs (1959) to include the range of properties that had been observed in galaxies as astronomical techniques improved. de Vaucouleurs transformed the original tuning fork diagram into a three-dimensional model, an example of which is given in Fig. 1.3. Through the centre of the diagram runs the galaxy morphology from elliptical to S0 to spiral, echoing the Hubble sequence if the two spiral forks were collapsed into one branch. Morphologies either side of this line contain complete (r) and incomplete (s) ring structures, while above and below the line are the barred and unbarred galaxies.
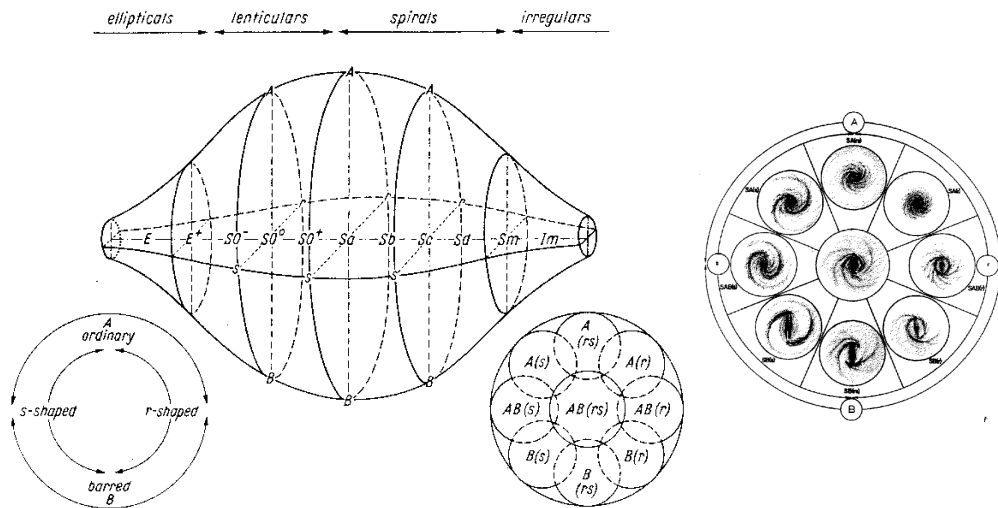
Figure 1.3: The de Vaucouleurs (1959) classification sequence on the left, with a visualisation of how the galaxy appearance changes in a slice through the diagram on the right.
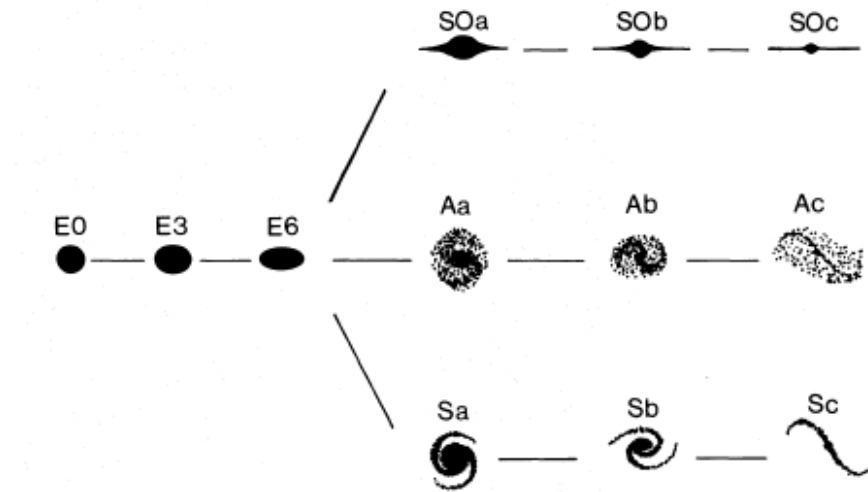
Figure 1.4: A visualisation of the van den Bergh (1976) classification sequence.

Unlike the original Hubble diagram, this diagram lists S0s as a continuous sequence from $S0^-$, which represents early-type, featureless lenticulars, to $S0^+$, which are later-type lenticulars with some faint structures such as dust-lanes, and allows them to display features such as bars. Due to the three-dimensional nature of the de Vaucouleurs sequence, the different permutations of parameters available added a new level of complexity to the classification of galaxy morphology, greater than could be achieved with the earlier Hubble sequence.

In 1976, van den Bergh proposed a further update on the Hubble sequence that built upon this idea that S0s formed a continuous sequence (van den Bergh, 1976). By this time it was known that S0s could display a range of properties similar to spirals, such as the variations in the luminosity fractions of the bulge and the presence of bars. As a result, van den Bergh combined the barred and unbarred spirals into one fork, and introduced two new, parallel forks representing S0s and anaemic (gas-poor) spirals. As can be seen in Fig. 1.4, the spiral and S0 branches still retain the a–c subclasses from the Hubble sequence. The layout of the van den Bergh sequence allowed spirals to evolve both left towards the ellipticals and upwards through the anaemic spirals to the S0s through different processes. An extension of this sequence has recently been suggested by Kormendy & Bender (2012), in which spheriodal galaxies are added at the end
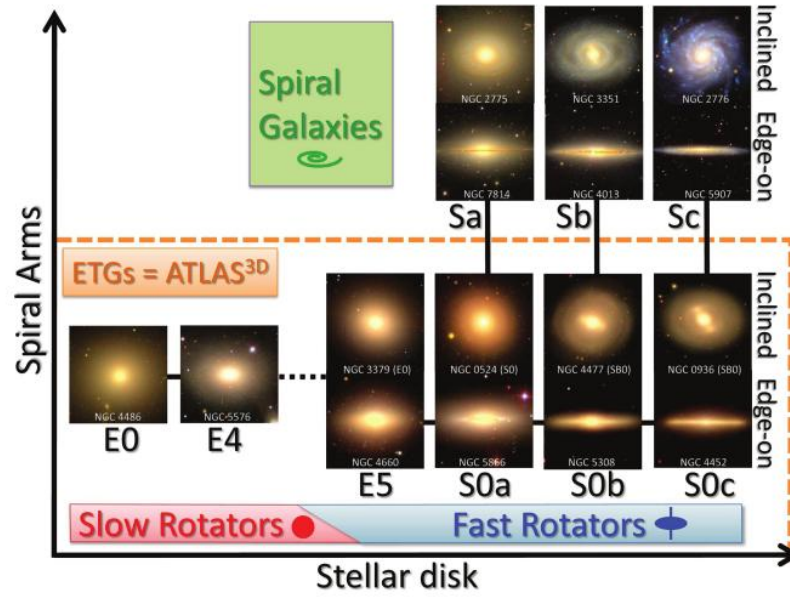
Figure 1.5: Galaxy morphology classification system based on galaxy kinematics (Cappellari et al., 2011).

of the S0 fork as an extension of such galaxies with very low bulge-to-total light ratios, and irregular galaxies located at the same point on the spiral branch.

Another recently proposed classification system that has moved away from the purely morphological Hubble classes for ellipticals and lenticulars is that of Cappellari et al. (2011). Instead, early-type galaxies are classified according to their rotation speed, with the spiral classes branching off perpendicularly from the fast rotators (discy galaxies), as in Fig. 1.5. This classification system has the benefit that it uses the kinematics of early type galaxies to determine its morphology, as opposed to visual classifications which can often prove problematic, as face-on lenticulars tend to be mainly featureless, and thus can easily be misclassified as ellipticals.

One key element that each of these systems have in common is the increasingly complex classification of S0s as more of these galaxies have been identified and their properties better understood. As a result, S0s are increasingly being seen as a distinct class of galaxy, as opposed to a short-lived transitional phase between spirals and ellipticals. In each case, though, they have remained either beside or parallel to the spiral sequence, echoing the similarities between these

two morphologies. This placing may represent a possible sequence of galaxy evolution, where S0s are quenched spirals in which the gas has been stripped out of the galaxy or used up by star formation. Since that gas is necessary to fuel further star formation, once it is gone, the star-formation rate would drop to an insignificant level, and the spiral arms would fade to leave a featureless disc galaxy. However, if this theory for the transformation of spirals into S0s is true, the exact star-formation quenching process is still uncertain. Therefore, understanding this transformation is thought to be a key stage in comprehending the evolution of galaxy morphology and the significance of the Hubble sequence.

1.2 Evidence for the Transformation of Spirals to S0s

In addition to their obvious visual similarities, plenty of more substantial evidence exists to suggest an evolutionary link between spirals and S0s. One often-cited piece of evidence is the morphology–density relation of Dressler (1980) presented in Fig. 1.6, which showed that spirals tend to dominate the less-dense outer regions of nearby clusters and the field, while ellipticals and S0s are more commonly found closer to the cores of clusters. A later study by Varela et al. (2004) found similar results, in which late-type spirals are more frequently found among isolated galaxies, while S0s appear to prefer denser environments. These findings suggest that the local environment plays a key role in the transformation of spirals to S0s, where the higher frequency of interactions in groups and clusters contribute significantly to the quenching of star formation in the progenitor spirals.

This trend has been found to hold out to $z \sim 1$ by Postman et al. (2005) and Smith et al. (2005), although it does appear to change form with redshift. For example, at higher redshifts, the fraction of early type galaxies was found to be lower than in the more local Universe, which was assumed to be due to a deficit
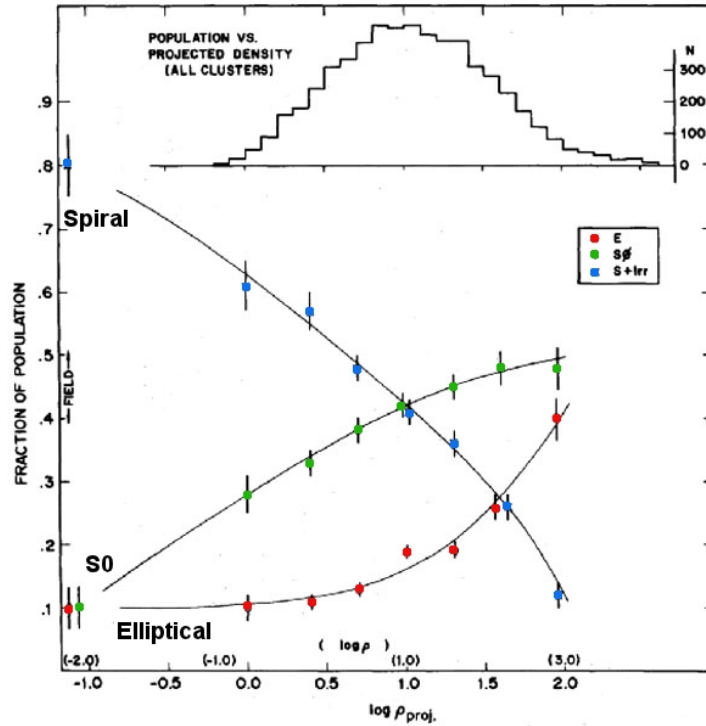
Figure 1.6: A plot from Dressler (1980) showing that towards higher density environments, the fraction of S0s and ellipticals (green and red dots respectively) increases while that of spirals (blue dots) decreases. It is interesting to note that the fraction of ellipticals is flatter than that of S0s at lower densities, then increases more rapidly at higher densities.

of S0s and an excess of spirals at higher redshifts. This assumption ties in with the morphology–redshift relation (Dressler et al., 1997; Fasano et al., 2000; Desai et al., 2007), an example of which is given in Fig. 1.7. It can clearly be seen that since $z \sim 0.65$, the fraction of S0s has increased, while that of spirals has decreased proportionally, consistent with the idea that spirals evolve into S0s over time. Similar results have been obtained by Couch & Sharples (1987), Ellingson et al. (2001) and Poggianti et al. (2006), and are thought to further reflect the truncation of star formation in these galaxies over time through galaxy mergers and interactions with other galaxies and the intracluster medium (Dressler et al., 1994; Couch et al., 1994). The Butcher–Oemler effect (Butcher & Oemler, 1984) finds that blue, star-forming galaxies appear to be increasingly common in clusters at higher redshift, providing further evidence for this scenario.

The Tully–Fisher relation (Tully & Fisher, 1977), which is a well-defined trend between the rotational velocity and luminosity of spiral galaxies, has also
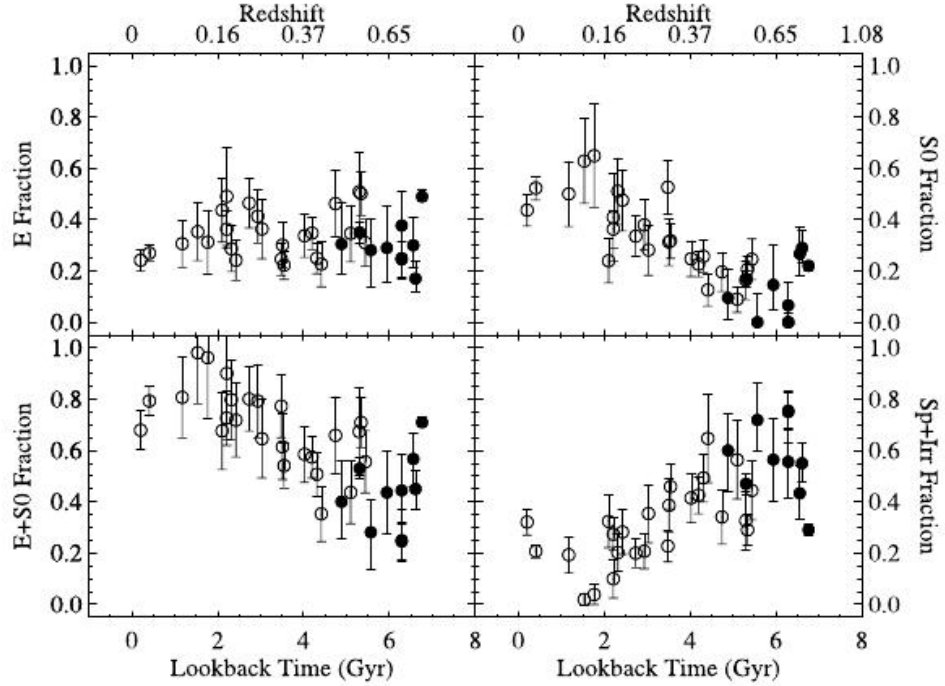
Figure 1.7: A plot from Desai et al. (2007) showing that since $z \sim 0.65$ the fraction of S0s has increased while that of spirals has decreased proportionately.

been shown to provide evidence of a link between spirals and S0s. If S0s are simply quenched spirals, they should be fainter than the progenitor spiral but with similar kinematics, and therefore would produce a similar trend to spirals, but offset in luminosity at a given rotational velocity. Many studies have claimed to find this offset, including Mathieu, Merrifield & Kuijken (2002), Bedregal, Aragón-Salamanca & Merrifield (2006) and Rawle et al. (2013), with typical values of $\sim 0.8 - 1.8$ magnitudes fainter than spirals in the I-band, or $\sim 0.8 - 1.2$ magnitudes fainter in the K_s band. Bedregal, Aragón-Salamanca & Merrifield (2006) found evidence that the magnitude of the offset for each galaxy correlated with the age of its stellar populations and therefore the time since the star formation was quenched. Furthermore, they attributed the scatter in the Tully–Fisher relation to the different periods of time since each galaxy was quenched, showing that the galaxies did not all undergo the transformation at a single epoch. However, not all studies found such convincing offsets: Neistein et al. (1999), Hinz, Rix & Bernstein (2001); Hinz, Rieke & Caldwell (2003)

and Williams, Bureau & Cappellari (2010) found small offsets that were deemed insignificant compared to the scatter in the measurements. Williams, Bureau & Cappellari (2010) attributed such contradictory findings from different studies to mass differences between spirals and S0s also affecting the location of the S0s on the Tully–Fisher relation. It is also possible that different quenching mechanisms may disrupt the kinematics of the stars to different extents, thus contributing further to the scatter in this relation (Noordermeer et al., 2008). However, even where the S0 offset from the spiral Tully–Fisher relation was found to be small in these studies, the trend between the intrinsic luminosity and rotational velocity of the galaxies was still found, further emphasising their potential evolutionary link to spirals.

If a spiral galaxy is stripped by a gentle process, such that the star formation is quenched without significantly disrupting the stellar orbits, then the number of globular clusters in the galaxy should remain constant as the galaxy fades to an S0. As a result, the globular cluster specific frequency, which is the number of globular clusters per unit luminosity of the galaxy, would be expected to increase with time since the star-formation was quenched. This trend was found to exist by Aragón-Salamanca, Bedregal & Merrifield (2006) and Barr et al. (2007), and was attributed to the gas being stripped from spirals galaxies as they entered denser environments. The photometric study of Aragón-Salamanca, Bedregal & Merrifield (2006) found that the globular cluster specific frequency increases by a factor of ~ 3 from spirals to S0s, which correlates well with the ~ 1.2 magnitude offset – or a factor of three drop in luminosity – in the Tully–Fisher relation measured by Bedregal, Aragón-Salamanca & Merrifield (2006). Similarly, they found a strong correlation with the colour of the S0 galaxy, where the globular cluster specific frequency increased in redder galaxies, while the spectroscopic study of Barr et al. (2007) identified a similar trend in S0s with older stellar populations.

A final piece of evidence is based on the stellar population differences between spirals and S0s – if S0s are truly an end-point in the evolution of spirals,

there should be detectable galaxies currently undergoing the transition. These galaxies would display no ongoing star formation, but would have evidence of recent star formation activity. Such galaxies were first detected by Dressler & Gunn (1983), and are characterized by their strong Balmer absorption features and lack of emission lines. Consequently, such systems were named 'k+a' galaxies since their spectra comprise that of young A-class stars superimposed upon an older stellar population. Recently, these galaxies have undergone a surge of interest as their possibility of being transitionary objects between spirals and S0s has been realised, and the results from these studies have helped develop this hypothesis. For example, Poggianti et al. (2009) found that, like S0s, k+a galaxies preferentially exist in clusters, and are relatively rare in the field. Similarly, in clusters, k+a galaxies tend to have discy morphologies (Caldwell, Rose & Dendy, 1999; Tran et al., 2003), and in some cases even show evidence of faint spiral arms, further contributing to the theories that they are recently quenched spirals (Poggianti et al., 1999).

Additionally, recent studies have identified red spiral galaxies as a possible transitional phase between normal spirals and k+a galaxies (Wolf et al., 2009; Masters et al., 2010). These galaxies have been found in intermediate density environments, and display ongoing star formation at a rate ~ 4 times lower than in blue spirals of similar mass (Wolf et al., 2009). Masters et al. (2010) studied a sample of face-on red spirals from the Galaxy Zoo project (Lintott et al., 2008), and identified that these galaxies are not simply dust-reddened spirals or dominated by the light from older stellar populations in their bulges. As a result, they concluded that red spirals are truly passive disc galaxies that are either currently undergoing quenching, or have recently (within ~ 1 Gyr) been quenched, and therefore have not yet had sufficient time to fade to a k+a galaxy or an S0.

Together, all of this evidence points towards spiral galaxies transforming into S0s by having their star formation quenched, where the quenching process is driven by interactions with neighbouring galaxies in higher density environments. However, to confirm this hypothesis, the quenching processes and their

effects on the star formation throughout the galaxy must first be understood.

1.3 Transformation Scenarios

Many scenarios have been proposed to explain the transformation of spirals to S0s, most of which focus on interactions with other galaxies or the intracluster medium (ICM) due to the prevalence of S0s in denser environments. Such interactions would quench the star formation in the disc, leaving the galaxy to fade and evolve passively into an S0. However, some interactions will prove more efficient at stripping the gas from a galaxy, while others would induce more disruption to the gas and trigger further starbursts within the galaxy. A systematic illustration of the different effects on the star-formation rate with time is given in Fig. 1.8, all of which would eventually quench the galaxy over different timescales and leave their own individual marks on the star-formation history of the galaxy.

One quenching scenario is *ram-pressure stripping* (Gunn & Gott, 1972), in which the cold disc gas is stripped out of the galaxy as it falls through the hot plasma in the ICM. This form of gas stripping would be very efficient, resulting in a fast quenching of star formation as $\sim 80\%$ of the disc gas is rapidly removed from the galaxy over a typical timescale of $\sim 10^7$ years for rich clusters – a small fraction of the cluster crossing time (Abadi, Moore & Bower, 1999). This scenario is depicted by the green dot-dash line in Fig. 1.8. Direct evidence of ram-pressure stripping occurring in spiral galaxies has been detected in the Virgo (Cayatte et al., 1990; Veilleux et al., 1999; Vollmer, 2003; Vollmer et al., 1999, 2004a,b; Kenney, van Gorkom & Vollmer, 2004; Crowl et al., 2005) and Coma Clusters (Bravo-Alfaro et al., 2000, 2001), and within other galaxy groups and clusters (Kemp et al., 2005; Rasmussen, Ponman & Mulchaey, 2006; Levy et al., 2007) using observations of HI gas. Such observations have shown evidence of HI deficiencies within cluster spiral galaxies, and in some cases even tails of HI gas trailing behind the galaxy as it falls through the ICM (Oosterloo &
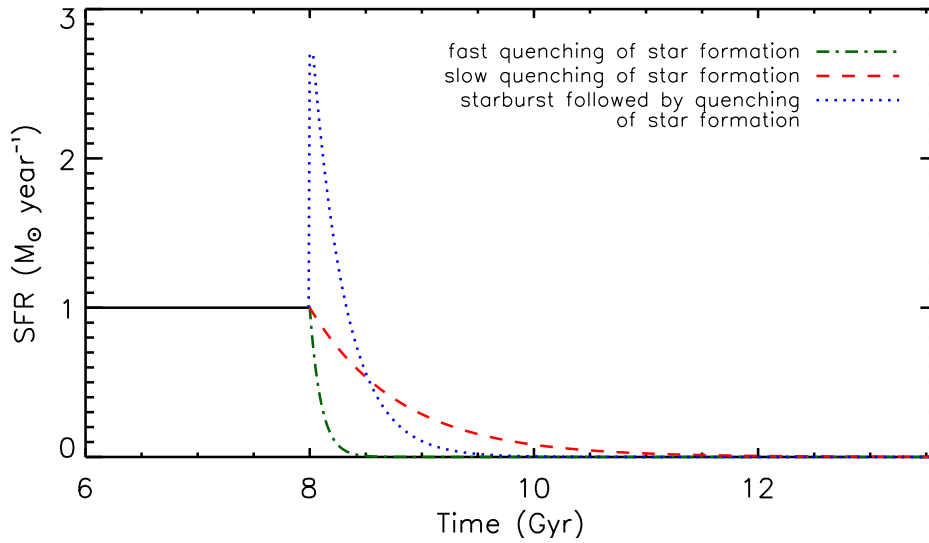
Figure 1.8: An illustration of the effect on the star formation rate of the disc by different quenching scenarios. The green dot-dashed line represents a fast quenching with no further star formation, such as ram-pressure stripping, while the red dashed line represents a slower quenching scenario with no star formation, which could be explained by starvation. Finally, the blue dotted line represents the more turbulent quenching processes, such as harrassment, unequal-mass galaxy mergers and a less gentle ram-pressure stripping scenario, in which the gas is disrupted and produces a final gasp of star formation prior to being quenched. Image adapted from Bamford (2006).

van Gorkom, 2005; Kim et al., 2008). Sun, Donahue & Voit (2007) also found evidence of bursts of star-formation in the tail of ESO 137-001 in the Abell 3627 cluster, showing that the disruption in the disc gas by ram-pressure stripping can trigger star formation within the stripped gas in addition to any star formation induced in the disc as the gas is stripped. The inclination of the galaxy as it travels through the ICM would also affect the amount of gas lost in this way, with studies such as Abadi, Moore & Bower (1999) finding that galaxies falling face on into the cluster can lose up to 50% more gas than edge-on galaxies due to the larger surface area affected by the stripping.

A variation on this stripping scenario is the *strangulation* or *starvation* model that was proposed by Larson, Tinsley & Caldwell (1980), in which the hot, diffuse gas is stripped from the halo instead. Since it is this halo gas that accretes onto the disc to replenish the gas used up in star formation, its removal leads to a slow truncation of the star formation as the galaxy consumes the remaining

gas in the disc. This slow truncation is described in Fig. 1.8 by the red dashed line. As with ram-pressure stripping, the ICM is most likely responsible for the removal of the halo gas, but in this case typically happening over $\sim 10^9$ years (Bekki, Couch & Shioya, 2002).

Interactions with neighbouring galaxies can also strip the gas from galaxies through *galaxy harassment* (Moore, Lake & Katz, 1998). Simulations by Moore, Lake & Katz (1998) and Fujita (1998) have shown that a single such interaction with another galaxy would be insufficient to strip a spiral galaxy of all of its gas. Therefore, to completely strip all the gas from a spiral galaxy and quench its star formation, multiple high-speed encounters would be necessary, especially for more luminous spirals in which this gas stripping process is less efficient (Moore et al., 1999). Additionally, the gravitational forces acting between the interacting galaxies could trigger an increased star-formation rate within the galaxy being stripped as the gas and stars within the disc are disturbed, as described by the blue dotted line in Fig. 1.8. As a result of the disruption from the gravitational forces acting on the galaxy, the velocity dispersion of the galaxy would increase, giving the galaxy a more spheroidal morphology, and gas would be dumped into the central regions of the galaxy, feeding further star formation there (Fujita, 1998).

Galaxies that interact under the right conditions may eventually collide through *unequal-mass galaxy mergers* (Mihos & Hernquist, 1994), in which the disruption to the orbits of the gas in the accreting galaxy would induce a series of starbursts throughout the disc that quenches all star formation. This scenario is also portrayed by the blue dotted line in Fig. 1.8. It was determined by Bekki (1998) that the merging galaxies being of unequal mass was important to maintain the disc structure of the final galaxy – to produce a gas-poor S0 by merging two spirals a typical mass ratio of $\sim 3 : 1$ is necessary. As the mass ratios exceed $10 : 1$, the resultant galaxy would display a small drop in the star-formation rate, and successive minor mergers of similar scales would be necessary to eventually use up all the gas and produce an S0.

It is still uncertain whether any one of these processes dominate the transformation of spirals to S0s in clusters, or if the process changes with time, environment or stellar mass. Evidence that multiple processes can contribute towards the quenching of star formation in a single galaxy has been found in recent simulations by Cen (2014). This study found that ram-pressure stripping would remove the gas from the outer disc, truncating the star formation in the disc and leaving a reservoir of gas in the central regions that feeds the in-situ star formation there. Without gas from the rest of the disc migrating inwards to fuel this residual star formation, it will then be slowly quenched by starvation as it uses up the remaining gas that was not stripped out earlier.

Further evidence that different processes can be responsible for the formation of different S0s lies in the increasingly complicated morphologies that have been detected in such galaxies. One interesting feature is the presence of counter-rotating discs – around a quarter of S0s are now known to contain gaseous components counter-rotating with respect to their stellar disc, and around 10% display counter-rotating stellar discs (Bertola, Buson & Zeilinger, 1992; Kuijken, Fisher & Merrifield, 1996; Emsellem et al., 2011). It is therefore likely that these S0s experienced a different formation history to the simpler bulge-plus-disc systems, and so, to truly understand the evolution of galaxy morphology, we need to be able to explain the formation of all the galaxies we observe, both usual and unusual.

Each of the processes outlined above would affect the star formation in different parts of a galaxy in different ways, from a gentle quenching of the star formation, to the gas being disrupted and dumped into the centre of the disc to fuel a final starburst there, to even more turbulent processes that use up all the gas rapidly in starbursts throughout the galaxy. Therefore, studying the star-formation history across an S0 galaxy and within its different components, such as the bulge and disc, can provide crucial information on the processes that formed that galaxy.

1.4 Bulge–Disc Decomposition

The first step to analysing the stellar populations of bulges and discs is to separate their light by bulge–disc decomposition. This technique separates the light from a galaxy into models of the bulge and disc, which, when combined, produces the best fit to the original galaxy image (de Vaucouleurs, 1959).

Each model component provides information on the effective size, luminosity and distribution of the light within the bulge and disc, which can help determine how the galaxy formed. One example of the use of this information is to plot the effective surface brightness of each component against its scale length to produce the Kormendy relation (Kormendy, 1977). As can be seen in Fig. 1.9 for elliptical and early-type disc galaxies, more luminous galaxies have larger scale lengths and fainter effective surface brightnesses measurements, suggesting that they are more diffuse. A later study by Hamabe & Kormendy (1987) included measurements from the bulges of spirals, and found an extension to this trend to

Figure 1.9: The Kormendy relation, linking the effective surface brightness of a galaxy with its scale length (Kormendy, 1977). Small symbols represent dwarf galaxies and larger symbols imply 'normal' galaxies. The thick solid line is the line of best fit to the galaxies, while the thin line represents the line of constant M_B for comparison. T1, T2 and T3 represent isolated, group and cluster galaxies respectively.

Figure 1.10: The Kormendy relation for the bulges of S0s from field (open triangles) and cluster (filled squares) environments (Barway et al., 2009). It is clear that the bulges of field S0s appear to follow the Kormendy relation in Fig. 1.9 while cluster S0s do not.

lower scale-lengths. By comparing the results with those in Fig. 1.9, the spiral bulges appear to overlap with the majority of the S0 sample used in Kormendy (1977), indicating that they may have experienced similar formation histories to S0s (Hamabe & Kormendy, 1987).

A more recent study of the Kormendy relation for S0s by Barway et al. (2009) found that while the bulges of field S0s also show this trend, those in cluster S0s do not, instead forming a downward scatter where the effective surface brightness drops significantly at larger scale lengths. This drop can be seen in Fig. 1.10, and is thought to be evidence of transformations induced by environmental effects such as minor mergers, ram pressure stripping or harassment. Barway et al. (2007) also found that in faint S0s, the bulge effective radius increases with the disc scale length, while in brighter S0s it decreases with increasing disc scale length. Secular evolution of spirals into lenticulars predicts the former trend since the passive fading of the bulge and disc would conserve their relative scale sizes, while the latter correlation would be expected from a more turbulent tran-

sition. Therefore this variation suggests a further dependence on the local environment of a galaxy when deriving its evolutionary history.

Other studies of the Kormendy relation have looked at differences in the relation for bulges and discs of spirals and S0s. These studies have found that as you move from S0s to late-type spirals, the effective size of the bulge decreases while its effective surface brightness decreases, whereas discs were found to display much less variation between morphologies (de Jong, 1996; Graham, 2001; Möllenhoff & Heidt, 2001; Trujillo et al., 2002; Aguerri et al., 2004; Laurikainen et al., 2007; Graham & Worley, 2008; Oohama et al., 2009). As a result, it is becoming apparent that the increase in the bulge-to-total light ratio observed in early-type disc galaxies, such as S0s, is driven by the evolution of the bulge.

Additional information on the formation histories of the bulges and discs can be derived by comparing their stellar populations. The analysis of multi-waveband photometry makes it possible to compare the bulge and disc colours as a proxy for their stellar populations since higher metallicities and older stellar populations strengthen the redder light from the galaxy. Such comparisons have found, for example, that in both spirals and S0s, the discs are bluer than the bulges (Bothun & Gregg, 1990; Peletier & Balcells, 1996; Hudson et al., 2010; Head et al., 2014), which suggests that disc galaxies have more recent star formation activity at larger radii (de Jong, 1996) or higher metallicities in their nuclear regions (Beckman et al., 1996; Pompei & Natali, 1997). Colour gradients have also been detected within bulges and discs by this method – negative colour gradients have been found within the bulges of S0s (Terndrup et al., 1994; Peletier & Balcells, 1996; Head et al., 2014) and spirals (Möllenhoff, 2004), while discs in these galaxies have been shown to contain both positive (Head et al., 2014) and negative (Michard & Poulain, 2000; Kannappan, Guie & Baker, 2009) gradients. Since negative colour gradients imply that redder light is more centrally concentrated within these components than bluer light, such trends imply the presence of increasingly older or more metal-rich stellar populations at smaller radii within these galaxies.

However, estimates of the stellar populations derived from colours alone are highly degenerate, such that using only the photometric colour, an unresolved stellar population cannot be distinguished from another that is three times older with half the metallicity (Worthey, 1994). Additionally, galaxies can also be affected by dust reddening, in which the dust present in the plane of an inclined disc can block the blue light from the galaxy, and give it a redder colour at optical wavelengths (Disney, Davies & Phillipps, 1989). To resolve these issues, and hence better understand the star-formation histories across galaxies, spectroscopic studies are vital.

1.5   Spatial Studies of the Stellar Populations

Spectroscopic studies of stellar populations over galaxies have long been used to determine their spatial star-formation histories more accurately. In most cases, the studies have focussed on long-slit spectra aligned along the major and minor axes of the galaxy to obtain estimates of the spatial distribution of the stellar ages and metallicities, although the past decade has welcomed integral field unit (IFU) spectroscopy over wider fields of view, providing more complete spatially-resolved spectroscopic information for galaxies.

Studies by Fisher, Franx & Illingworth (1996), Bell & de Jong (2000), Bedregal et al. (2011) and Prochaska Chamberlain et al. (2011) have found evidence for negative metallicity and positive age gradients across S0s, which indicate that the central regions of S0s contain younger and more metal rich stars. Further signs of recent star formation in bulge regions of S0s has been detected by Poggianti et al. (2001), Ferrarese et al. (2006), Sil'Chenko (2006) and Kuntschner et al. (2006), and a study by Pracy et al. (2013) found evidence of strong positive age gradients within the central ~ 1 kpc of the bulges of k+a galaxies. Another recent study of k+a galaxies by Rodríguez Del Pino et al. (2014) also found evidence that the most recent star formation activity in these galaxies was centrally concentrated within the disc.

Further studies of the luminosity-weighted ages of the bulges of S0s have shown an apparent relationship with luminosity. Kuntschner (2000), Smail et al. (2001), Poggianti et al. (2001) and Barway et al. (2013) all found evidence that while the bulges of S0s tended to contain younger stars than the discs, this trend was stronger in lower-luminosity S0s which appeared to contain younger stellar populations on average than the brighter S0s, even if they were in the same cluster. These results provide even more evidence that S0s can evolve from spirals through different quenching mechanisms and over different timescales. Brighter S0s are more similar to ellipticals, and therefore likely to have formed through more turbulent processes than fainter S0s, which were most likely stripped of gas through gentler mechanisms, and then built up their young bulge population through secular processes that created a pseudo-bulge (Barway et al., 2013).

Such studies of the star formation histories of S0 bulges and discs have revealed colour gradients across the galaxies, which are likely indicators of age and metallicity gradients, and have suggested that the quenching process responsible for the formation of each galaxy is dependent on environment and luminosity. However, such colour gradients fail to provide clear information on whether they represent a gradient within the individual components, or whether they arise simply from the superposition of varying amounts of bulge and disc light, where each component contains stellar populations of distinct different ages and metallicities. It also leaves open the possibility that the colour gradients could result from differing amounts of dust extinction at different radii, rather than telling us about spatial variations in the stellar population. Similarly, spectroscopic studies across S0 galaxies have attempted to resolve the age-metallicity degeneracy that often affects studies of galaxy colours, but still provide no information on the proportion of the light from the bulge and disc at any given location within the galaxy. Therefore, to resolve this ambiguity, we have developed two novel techniques to spectroscopically separate the light from bulges and discs in order to produce two one-dimensional spectra representing purely the light from each component.

These "clean" spectra can then be analysed for their ages and metallicities, as well as any gradients in these quantities, to determine the sequence of events that led to the quenching of star formation and the formation of S0 galaxies.

1.6   Outline of This Thesis

In this thesis, we set out to analyse the spectroscopic star formation histories within bulges and discs for a sample of S0s from the Virgo and Fornax Clusters, in order to determine the process that triggered their transformation from spirals. These clusters were selected as the closest single systems with sufficient members to undertake a systematic study of this transformation process. Chapter 2 introduces the sample in detail and outlines the data reduction. Chapter 3 describes a new technique to spectroscopically decompose long-slit spectra of S0 galaxies into bulge and disc components, and Chapter 4 covers the subsequent analysis of the separate components' stellar populations and star formation histories. Chapter 5 then looks at an unusual galaxy in the sample, NGC 4550 which has two counter-rotating stellar discs, and outlines a different technique to separate the star formation histories of the two discs using their different kinematics. The implications of these results for the likely evolutionary tracks followed by S0s are discussed in Chapter 6, followed by ideas to further develop the work presented in this thesis.

Chapter 2

Sample and Data Reduction

The various scenarios for S0 formation discussed in Chapter 1 make different predictions about the current properties of their bulges and discs. We might also expect different S0s to form via different mechanisms. Clues to their formation histories lie within the 'archaeological record' that can be extracted from spectral observations. Therefore, to understand this transformation, we need to accurately study the stellar populations within each component independently. Such a study requires high-quality long-slit spectra along the major axis of a sample of nearby galaxies with a high signal-to-noise ratio (S/N) out into the very outskirts of each galaxy.

2.1   Sample Selection

Since S0s appear to favour denser environments at low redshift, this study was carried out with a sample of 30 S0 galaxies from the Virgo and Fornax clusters, which are two of the largest and closest galaxy clusters to the Milky Way at distances of ~ 16.5 Mpc and ~ 19.3 Mpc respectively (Mei et al., 2007; Tonry et al., 2001). These two clusters were selected as they allow for a comparison of the different formation mechanisms between clusters, while their richness is a useful test for the differences within clusters. Additionally, their proximity allows us to obtain high-quality, spatially-resolved spectra with sufficiently high

S/N to reach right out into the outskirts of each galaxy, thus providing us with a clear picture of how the stellar populations have been affected over the full structure of the galaxy.

A total of 30 galaxies were selected from these two clusters- 21 from the Virgo Cluster and 9 from the Fornax Cluster. To obtain a representative view of how the S0s in these clusters were created, the sample was selected to include all those galaxies classified as S0 by Kuntschner (2000) in the Fornax Cluster, and by the ACS Virgo Cluster Survey (Côté et al., 2004) for those in the Virgo Cluster. As a secondary selection criterion, all galaxies with inclinations of ≤ 40 degrees (where 90 degrees is edge-on) were eliminated in order to reduce contamination in the sample from misclassified ellipticals. The inclination of each S0 in the Virgo Cluster was calculated by using their ellipticity measurements from Ferrarese et al. (2006), which were determined by fitting elliptical isotopes to g- and z-band images of each galaxy. The axis ratio, q, was derived from these ellipticities using

$$\epsilon = 1 - \frac{b}{a} = 1 - q, \tag{2.1}$$

where a and b are the lengths of the semi-major and semi-minor axes respectively. The inclination, i, could then be calculated using

$$cos^2 i = \frac{q - q_0^2}{1 - q_0^2}, \tag{2.2}$$

where q_0 is the minimum axes ratio for a galaxy considered to be edge on (Hubble, 1926b). Since galaxies are not infinitely thin, q_0^2 is generally taken to have a value of 0.2 (Holmberg, 1958).

As a result of this selection process, a sample of galaxies was obtained spanning a factor of 100 in luminosity and two orders of magnitude in dynamical mass, covering a wide range of B/T light ratios and local environments within the cluster, which is truly representative of all the S0 systems within these two clusters. The diversity in the final sample of galaxies can be seen in the SDSS images of the Virgo Cluster galaxies in Fig. 2.1, and the 2MASS JHK$_s$ images of
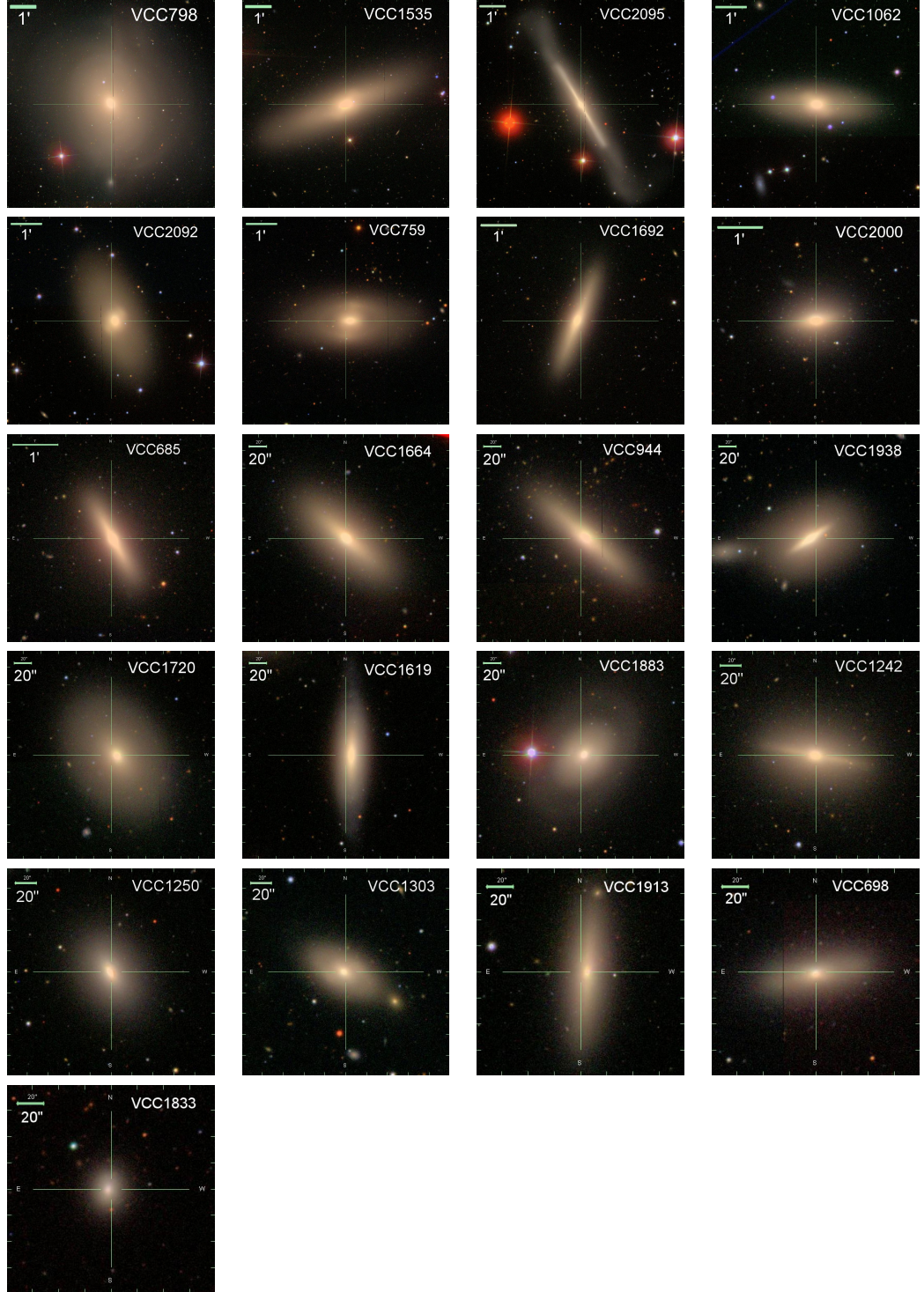
Figure 2.1: SDSS (DR7) images of each galaxy in the Virgo Cluster Sample, with the scale of each image shown in the top left corner. In all cases, the images are orientated with north towards the top and east to the left (Abazajian et al., 2009).
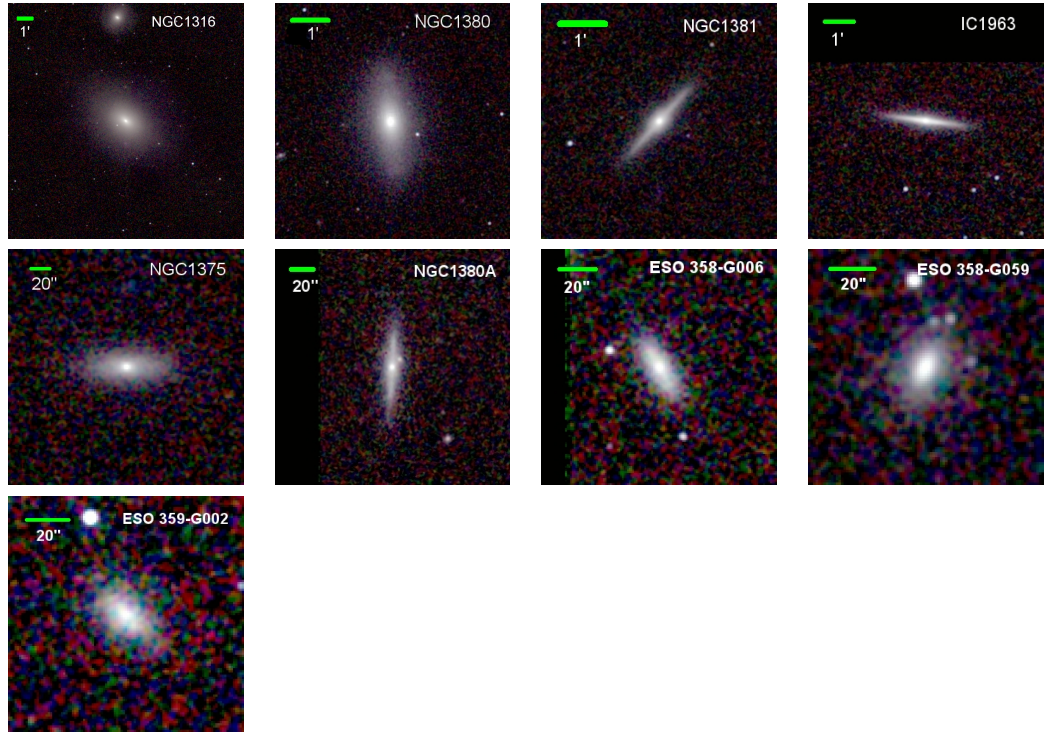
Figure 2.2: 2MASS images of each galaxy in the Fornax Cluster Sample, with the scale of each image shown in the top left corner. In all cases, the images are orientated with north towards the top and east to the left (Skrutskie et al., 2006).

the Fornax Cluster galaxies in Fig. 2.2. The SDSS images clearly show the red colours and featureless discs of the S0s, while the infra-red 2MASS images of the Fornax galaxies, selected for this figure because this cluster is not within the SDSS field of view, can see through any dust in the plane of the discs to highlight absence of regions of recent star formation.

2.1.1 Fornax Cluster

The Fornax Cluster sample were observed using the 8.2 m Antu/VLT between 2002 October 2 and 2003 February 24 with the FORS2 instrument in long-slit spectroscopy mode. Details of the sample and the observations are given in Table 2.1. For each galaxy, the slit was aligned with the photometric major axis, and was set to 0.5 arcsec wide and 6.8 arcmin in length. For all galaxies except NGC 1316, the centre of the galaxy was placed halfway along the slit in order to obtain information along the entire length of the major axis; NGC 1316

Table 2.1: Sample of S0s from the Fornax Cluster.

Name	RA	dec	B_T	Exp. Time	Date	Tel.
	$(^{h\ m\ s})$	$(°\ ´\ ″)$		(s)	(dd-mm-yyyy)	
(1)	(2)	(3)	(4)	(5)	(6)	(7)
NGC 1316*	03 22 41	−37 12 30	9.4	3×1200	13-10-2002	VLT
NGC 1380	03 36 27	−34 58 34	10.9	2×1200	24-02-2003	VLT
NGC 1381	03 36 31	−35 17 43	12.4	2×1600	24-02-2003	VLT
IC 1963	03 35 30	−34 26 51	12.9	2×1600	31-01-2003	VLT
NGC 1375	03 35 16	−35 15 56	13.2	2×1800	28-12-2002	VLT
NGC 1380A	03 36 47	−34 44 23	13.3	2×1700	28-12-2002	VLT
ESO 358-G006	03 27 18	−34 31 35	13.9	2×2400	14-10-2002	VLT
ESO 358-G059	03 45 03	−35 58 22	14.0	1×2550	08-02-2003	VLT
ESO 359-G002	03 50 36	−35 54 34	14.2	1×2250	26-11-2002	VLT

Note. Column (1): Galaxy name; Column (2): RA; Column (3): Declination; Column (4): Total apparent blue-band magnitude from de Vaucouleurs (1991); Column (5): Exposure time in seconds; Column (6): Date of observations; Column (7): Telescope. An asterisk beside the galaxy name indicates that the galaxy was significantly offset from the centre of the CCD.

is the largest galaxy in the sample, and it was necessary to offset it along the slit in order to cover sufficient sky for background subtraction. The standard resolution collimator was used in the unbinned readout mode, giving a spatial scale of 0.125 arcsec pixel^{-1}, and the GRIS1400V+18 grism gave a dispersion of 0.318 Å pixel^{-1} over a wavelength range of $4560 \leq \lambda \leq 5860$ Å. By analysing arc lines, the spectral resolution was found to be ~ 4 pixels FWHM, which corresponds to a velocity resolution of $\sim 73\,\mathrm{km\,s^{-1}}$ FWHM or a velocity dispersion of $\sim 31\,\mathrm{km\,s^{-1}}$. This data set was reduced and analysed in Bedregal et al. (2006), Bedregal et al. (2008) and Bedregal et al. (2011); the initial analysis of those papers provided a useful cross-check on the more powerful technique in the current analysis.

2.1.2 Virgo Cluster

The Virgo Cluster sample was observed using the GMOS instruments (Hook et al., 2004) in long-slit mode on Gemini-North and Gemini-South between 2008 April 24 and 2011 June 20, details of which are given in Table 2.2. As with

Table 2.2: Sample of S0s from the Virgo Cluster.

Name	RA ($^{h\ m\ s}$)	dec ($^{\circ\ \prime\ \prime\prime}$)	B_T	Exp. Time (s)	Date (dd-mm-yyyy)	Tel.	Seeing (arcsec)	Classification
(1)	(2)	(3)	(4)	(5)	(6)	(7)	(8)	(9)
VCC 798*	12 25 24	+18 11 26	10.09	4 × 900	26-02-2009	GN	1.4	S0
VCC 1535*	12 34 03	+07 41 59	10.61	4 × 900	26-02-2009	GN	1.2	S0
VCC 2095*	12 52 56	+11 13 53	11.18	4 × 900	01-06-2010	GN	1.4	S0
VCC 1062*	12 28 04	+09 48 14	11.40	4 × 900	18-01-2010	GS	0.7	SB0
VCC 2092*	12 52 18	+11 18 50	11.51	1 × 900	21-02-2009	GN	1.4	SB0
				3 × 900	26-02-2009	GN	1.3	
VCC 759*	12 24 56	+11 42 15	11.80	5 × 900	02-06-2010	GN	1.0	SB0
				1 × 900	08-07-2010	GN	0.6	
VCC 1692*	12 36 53	+07 14 47	11.82	4 × 1000	13-02-2010	GN	1.8	S0
VCC 2000	12 44 32	+11 11 25	11.94	4 × 900	11-02-2010	GS	0.6	E3/S0
VCC 685*	12 23 58	+16 41 37	11.99	4 × 900	11-03-2010	GN	1.8	S0
VCC 1664*	12 36 27	+11 26 21	12.02	2 × 900	27-04-2009	GN	1.5	E6
				2 × 900	28-04-2009	GN	1.0	
VCC 944	12 26 51	+09 35 02	12.08	4 × 900	23-04-2009	GN	1.3	S0
VCC 1938	12 42 47	+11 26 33	12.11	1 × 900	29-04-2009	GN	1.3	S0
				3 × 900	20-06-2009	GN	1.0	
VCC 1720*	12 37 31	+09 33 19	12.29	3 × 1500	30-05-2011	GN	0.7	S0
				2 × 1500	04-06-2011	GN	0.9	
				1 × 1500	20-06-2011	GN	0.8	

Table 2.2 – continued from previous page

Name	RA	dec	B_T	Exp. Time	Date	Tel.	Seeing	Classification
	(^{h} ^{m} ^{s})	($°$ $´$ $″$)		(s)	(dd-mm-yyyy)		(arcsec)	
(1)	(2)	(3)	(4)	(5)	(6)	(7)	(8)	(9)
VCC 1619	12 35 31	+12 13 15	12.50	2 × 900	20-06-2009	GN	1.5	E7/S0
				2 × 900	13-02-2010	GS	1.8	
VCC 1883*	12 41 33	+07 18 53	12.57	2 × 1500	25-05-2011	GN	0.9	RSB0
				1 × 1500	27-05-2011	GN	1.0	
				3 × 1500	28-05-2011	GN	0.9	
VCC 1242	12 29 53	+14 04 07	12.60	6 × 900	23-02-2010	GS	1.1	S0
VCC 1250	12 29 59	+12 20 55	12.91	1 × 900	19-04-2009	GN	1.4	S0
				3 × 900	20-06-2009	GN	1.4	
VCC 1303*	12 30 41	+09 00 56	13.10	3 × 1500	13-07-2010	GN	0.7	SB0
				1 × 1500	15-07-2010	GN	0.6	
VCC 1913	12 42 11	+07 40 37	13.22	4 × 900	22-02-2010	GS	0.6	E7
VCC 698	12 24 05	+11 13 06	13.60	4 × 1800	28-02-2009	GN	1.5	S0
				1 × 1800	23-04-2009	GN	1.5	
				5 × 1800	28-04-2009	GN	1.6	
VCC 1833	12 40 20	+15 56 07	14.54	2 × 900	13-02-2010	GS	1.4	S0

Note. Column (1): Galaxy name from Binggeli, Sandage & Tammann (1985); Column (2): RA; Column (3): Declination; Column (4):Total apparent blue-band magnitude from Binggeli, Sandage & Tammann (1985); Column (5): Exposure time in seconds; Column (6): Date of observations; Column (7): Telescope (GN- Gemini North, GS- Gemini South); Column (8): Seeing measurement at time of observations (FWHM); Column (9): Morphological classification from Côté et al. (2004). An asterisk beside the galaxy name indicates that the galaxy was significantly offset from the centre of the CCD, such that the sky subtraction outlined in Section 2.2.6 was carried out using background values from only one side of the galaxy.

NGC 1316 in the Fornax Cluster sample, it was necessary to offset the centres of the larger galaxies from the middle of the slit in order to maximize the spatial coverage and ensure sufficient background measurements for accurate sky sub-traction. The B1200 grating was used in combination with a 0.5 arcsec wide and 5.5 arcmin long slit, giving a wavelength range of $4300 \leq \lambda \leq 5450$ Å with a dispersion of 0.235 Å pixel^{-1}. The spectral resolution was measured from the FWHM of the arc lines to be ~ 1.13 Å, which corresponds to a velocity resolu-tion of $72\,\mathrm{km\,s}^{-1}$ FWHM, well matched to the Fornax data. Spatially, the CCDs were binned by 4 to give a final scale of 0.29 arcseconds pixel^{-1}. Details of the data reduction for this data set are given in Section 2.2.

Together, these two data sets provide a representative sample of cluster S0s in the local Universe, spanning a luminosity range of over five magnitudes and the full range of local environments within their host clusters. The reduced two-dimensional spectrum for each galaxy represents typically 1–3 hours of integra-tion on an 8-metre class telescope, providing very high signal-to-noise ratio data right out into the outer regions of the discs, which will allow us to decompose the light profile of each galaxy reliably at each finely-separated wavelength.

2.2   Data Reduction

The spectra for the Virgo Cluster galaxies were reduced using the GMOS spectral reduction packages in IRAF.[1] The process was carried out manually to allow the data to be checked after each step and ensure an accurate reduction. The Virgo Cluster galaxies were observed using GMOS on both Gemini-North and Gemini-South, with calibration flat fields, bias frames and CuAr arc spectra also taken for each set of observations with the same instrumental set-up. The observations

---

[1]IRAF is distributed by the National Optical Astronomy Observatories, which are operated by the Association of Universities for Research in Astronomy, Inc., under cooperative agreement with the National Science Foundation

were made in service mode, which ensured near optimal weather conditions for each observation. An example of the typical sequence of observations is listed below for a galaxy observed with four exposures:

- On the night

  - Target selected and acquisition images obtained to centre the target galaxy on the detector and to align the slit.

  - Calibraton flat field observed with a central wavelength of 4710 Å.

  - Two science exposures observed with a central wavelength of 4710 Å.

  - Two science exposures observed with a central wavelength of 4760 Å.

  - Calibraton flat field observed with a central wavelength of 4760 Å.

- Following day

  - Two CuAr arc images observed with central wavelengths of 4710 Å and 4760 Å.

- Each semester

  - A series of bias images are observed with the same instrumental set up as the science exposures, and median stacked to produce a master bias frame for all exposures observed that semester.

The GMOS detector contains three CCDs over which the spectrum is distributed, with gaps between each CCD of around 39 unbinned pixels (~ 9.2 Å). Therefore, each galaxy and calibration frame was observed over an even number of exposures with central wavelengths split equally between 4710 Å and 4760 Å in order to ensure full wavelength coverage. The CCD images also show four unexposed regions parallel to the wavelength direction. Two of these regions are at the edges of the CCD, and two lie 1/3 and 2/3 of the distance along the spatial direction where bridges lie across the slit to maintain a constant width over its full length. These bridges cover ~ 40 unbinned rows of pixels, which corresponds to

$\sim$ 2.9 arcsec in the radial direction in this data set, and the affected pixels were masked out in the analyses presented in Chapters 3, 4 and 5. Since the GMOS instruments have identical designs and are mounted on identical telescopes, the data reduction process outlined in below could be applied equally well to data from both instruments.

2.2.1 Bias Correction

The first step to reducing any astronomical data detected on a CCD is to correct for the bias level, which is an arbitrary value added to each pixel. Since the individual pixels on a CCD do not measure the incoming photons with uniform efficiency, an image taken of a uniform light source would result in a Gaussian distribution in the level of detections of all the pixels across the CCD. When the CCD is read-out, the charge amplifier converts the detections from charges to voltages for each pixel, which may result in a null detection for those pixels with measurements in the low end of the Gaussian tail. Therefore, to prevent such issues, especially when observing low-luminosity targets, a bias value is added to each pixel, which is sufficiently high to minimise the number of pixels with too-low values for the charge amplifier to detect, while simultaneously low enough to prevent too many pixels saturating if a bright star is contained within the field of view. For the three GMOS-North detectors the bias levels were measured to be $\sim$748, 610 and 373 counts from red to blue, and for GMOS-South the bias measurements were $\sim$717, 670 and 655 counts. In all cases, the typical variation was found to be around ±2 counts.

To correct for the bias level, a master bias image was provided by the Gemini Observatory for each run of observations, having been created by median stacking a series of zero second exposures to produce an image of the pixel-to-pixel variations across the CCD, such as the one shown in Fig. 2.3. By median stacking the individual images, the influence of any one-off features, such as cosmic rays, could be eliminated, thus producing a clean master bias frame that was then
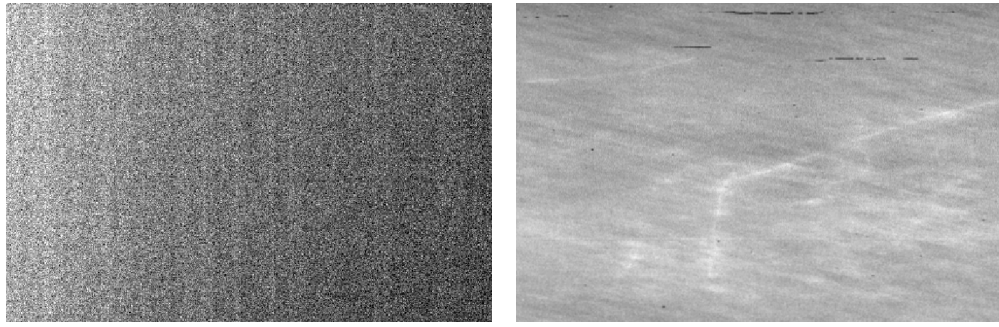
Figure 2.3: Examples of bias (left) and flat field (right) calibration frames. The pixel-to-pixel variations in the bias frame are typically of the order of 0.3%.

subtracted from the science and calibration frames.

2.2.2   Flat Field Correction

Although the bias level minimizes the number of null detections due to less efficient pixels, the variations in the quantum efficiency of each pixel still remain, and can result in artefacts in the image that may be invisible to the naked eye, but would significantly affect any measurements made from that image, particularly of low surface brightness targets. The causes of these variations in the pixel-to-pixel responses could be small differences in their sizes (and thus detection areas), variations in the gain of each pixel, bad pixels, obscuration from dust on the surface of the detector, and vignetting. Since few of these factors can be fixed prior to observations, we must apply the necessary corrections during the post-processing of the images.

The corrections are applied by a process of flat-fielding. Flat field images were observed throughout the night before each set of science exposures and for each wavelength set-up using the quartz halogen continuum lamp to simulate a uniform light source. These images were prepared by trimming the overscan regions, multiplying the pixel values by the CCD gain, mosaicking the three CCDs to produce a single image covering the full spectral range, and finally normalized by dividing through by a polynomial function in the wavelength direction, which was calculated from the response over the full spectral range. An example of part of a flat field image can be seen in Fig. 2.3, which clearly shows the effects

of dirt on the surface of the detector and large scale variations in the pixel responses. In all cases, to obtain the best flat field image representing as many of these defects as possible, the exposure times are selected to produce sufficiently high flux measurements while at the same time avoiding saturation.

Having created the master flat field for each set of science exposures, the bias-subtracted science frames were reduced by trimming the overscan regions, multiplying the pixel values by the CCD gain, mosaicking the the images to cover the full spectral range, and finally flat-field correcting by dividing by the master flat field image for that instrumental set-up. As part of this reduction process, an approximate wavelength solution was also applied to each frame using the central wavelength and pixel scale listed in the headers. This solution will act as a starting point for refining the wavelength calibration over the CCD after masking out cosmic rays and bad pixel columns, which will become distorted and harder to detect after correcting for the distortion in the spectrum due to the optics.

2.2.3 Cosmic Ray Removal

With the long exposure times necessary to observe faint, extended sources such as galaxies, the number of cosmic rays hitting the detector increases significantly, and they must therefore be removed. An IRAF task was used to initially identify possible cosmic ray detections in all the science and flat field frames by looking for pixels with values unusually higher than their neighbours. Having identified these targets, the mean value of all the pixels in a box with sides of typically 11 pixels centred on each target was calculated, after excluding the second highest pixel value within that box in case it is another cosmic ray detection, and the target labelled as a cosmic ray if its value was found to exceed a certain threshold above the mean value. Since many cosmic rays hit the detector at an angle, they can span many pixels and artificially enhance the mean pixel value of that part of the CCD, and so this procedure was run multiple times to ensure all the affected

pixels were identified and accounted for in the final mask. After the cosmic rays were removed using the mask, the image was inspected visually to ensure that no artefacts remained, and if this was found to be the case, the procedure was repeated with more iterations until no evidence of the cosmic ray detections were visible in the masked image.

2.2.4 Bad Pixel Masking

Another issue that some pixels on the CCD may have is that they do not measure the incoming flux linearly, and thus would give erroneous values compared to their neighbours in a manner that is not fully corrected by the flat-fielding process. Therefore, to remove the effects of such pixels, a bad pixel mask was created and applied to the science frames to replace the values of affected pixels by interpolation.

Normally, where flat field images have been taken on sky during twilight, exposures of different integration times are divided to identify pixels that do not show a linear increase between the two flux levels. However, this technique was not possible for the GMOS data as all the flat fields were observed with the same continuum lamp and with the same exposure time, and so a different technique was required. It was decided to use a modified version of the cosmic ray detection method outlined in Section 2.2.3. A reduced flat field frame was used, and the probability of each pixel being 'bad' was assessed by taking the median value of all the pixels in a box centred on that pixel, and adding the pixel to the mask if its value fell either above or below a given threshold away from the median. Repeating this analysis for each pixel produced a bad pixel mask for that image, and, by repeating this technique for similar images observed over the full semester, a reliable master bad pixel mask was constructed that could be applied to all the science images observed during that semester. This master bad pixel mask was then applied to the reduced science images by interpolating over the pixels marked as bad.

2.2.5   Wavelength Calibration

Having reduced and corrected all the science frames for defects on the CCD and incident events from cosmic rays, the next step was to calculate a reliable wavelength solution for each frame to allow accurate measurements of the kinematics and line indices. The wavelength solution was calculated using arc images that had been observed using Cu-Ar lamps as part of the daytime calibrations. The arc spectra were reduced in the same way as the science frames, but without bad pixel masking and the flat field correction steps, and were binned into sections of ten pixels in the spatial direction. A number of prominent arc lines, typically ~ 50, were identified over the full spectral range, and the mean offset between their measured and true wavelengths was calculated by fitting a polynomial of order 4. The residuals of the resulting wavelength fits were generally $\sim 0.2 - 0.3$ Å.

By repeating this process for each spatially binned spectrum, the offset between the initial and true wavelength solutions could be calculated over the full CCD, thus producing an accurate map for the wavelength solution which could be applied to the CCD to both refine the wavelength calibration of the data, and also correct for the geometric distortions caused by the instrument optics. An example of the effect of these distortions on a sky line can be seen in Fig. 2.4, along with the correction after applying the accurate wavelength solution to the science spectra.

2.2.6   Sky Subtraction

In order to measure the flux of the galaxy in the outskirts of the disc, and thus reliably measure the kinematics and line strengths, accurate sky subtraction is needed to remove the light from the background sky. The sky background was measured for each image over sections of the spectrum far from the centre of the galaxy to reduce contamination from the outer disc. In cases where the galaxies were located close to the centre of the CCD, the level of the sky background in
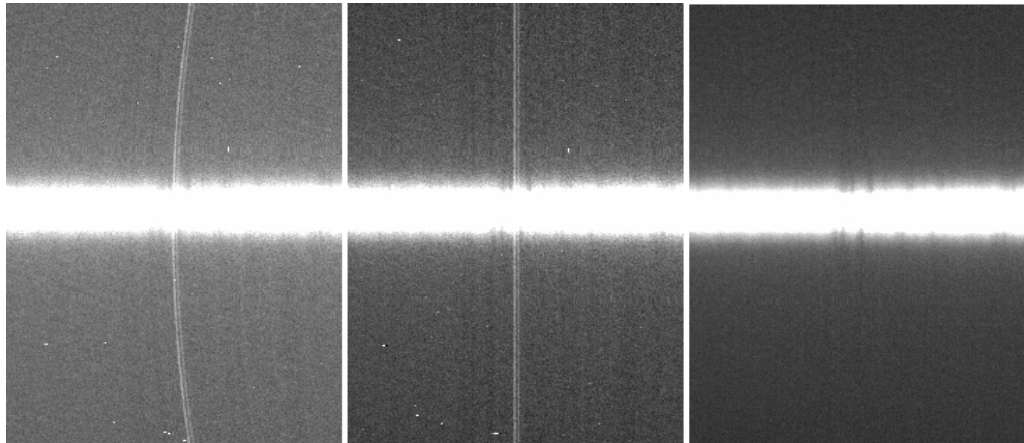
Figure 2.4: An example of the distortion imposed by the spectrograph on a prominent sky line centred on the Mg triplet in the spectrum of VCC 1938 (left), the correction after applying the accurate wavelength solution to the spectrum (centre), and the final flux-calibrated spectrum after sky subtraction and combining multiple exposures, which has also removed the remaining bright pixels that were not masked out in an earlier step (right).

each science image was measured over regions typically 100–200 pixels wide located close to both edges of the CCD, whereas for galaxies that were significantly offset from the centre of the CCD (as marked by asterisks in Table 2.2), the sky background was measured on only one side. Using these measurements, a first order function was calculated for each column of pixels, and the wavelength-calibrated spectra were then sky subtracted using these measurements.

It was important to carry this step out carefully as it was found that the GMOS spectra contained noticeable amounts of contamination from scattered light within the instrument, the physical distribution of which was independent of the position of the galaxy on the CCD and varied with the pointing of the telescope. This low-level scattered light prevented the light profile of the spectrum from levelling off at larger radii from the centre of the galaxy, making it difficult to identify where the background sky level should be measured for an accurate subtraction. It was noted by Norris, Sharples & Kuntschner (2006) that the scattered light in GMOS data appears to contribute a reasonably constant offset to the two-dimensional spectrum, significantly affecting measurements in the low-luminosity outer regions of galaxies but becoming more insignificant towards the inner regions. They suggested using the flux measurements in the four unex-

posed regions on each CCD (two at the top and bottom edges, and two at around 1/3 and 2/3 of the distance along the spatial direction where the bridges lie) to map out the magnitude of the scattered light over the CCD, and then to subtract that off the spectra. However, when applied to this data set, the results proved disappointing, with no clear improvement in the flux levels in the outer parts of the CCD, and in some cases even leading to the flux level increasing towards the edges of the CCD. From these results, demonstrated in Fig. 2.5, it could be seen that if the peak of the galaxy lay close to one of the bridges, the flux level under that bridge was higher than in any other unexposed region, suggesting that these unexposed regions are not truly unexposed and detect a low level of scattered light from the galaxy in addition to the approximately flat offset described by Norris, Sharples & Kuntschner (2006). Therefore, the sky background level was measured carefully in each reduced science image by using the light profiles at different wavelengths to identify the best region over which to take the background level. It was found that the bluest parts of the spectra were worst affected by the scattered light, resulting in several cases where the background level of counts increased towards the edge of the CCD. In such cases it was impossible to identify the true background level under the contaminating light. This phenomenon was most likely caused by the flat-field calibration lamps being very red-luminous, and thus better modelling the contaminating effect of the scattered light in this part of the spectrum. In order to apply a reliable background subtraction to the spectra, the regions selected for measuring the sky background were chosen by studying the one-dimensional light profiles of each spectrum over the full wavelength range. The radii over which the spectrum appears to level off over the longest wavelength range were then used to measure the background level as these regions were considered to be least affected by scattered light. Comparisons of the two-dimensional spectra of each galaxy showed that generally the worst affected regions, i.e. where the background light increased at larger radii, were blueward of 4300 Å. Since the bluest spectral feature used in this study was the Hβ feature at 4861 Å, the excess contamination at shorter
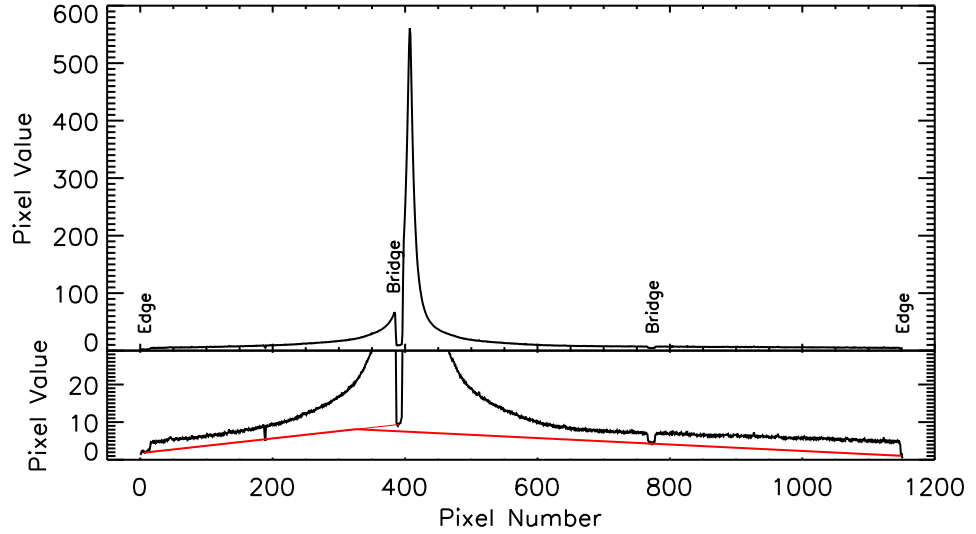
Figure 2.5: *Top*: An example of the mean light profile of a galaxy centred close to one of the bridges, with the unexposed regions under the bridges and at the edges of the CCD marked. *Bottom*: A close up view of the low-level flux, with the level of the scattered light marked in red using the technique of Norris, Sharples & Kuntschner (2006). It can be seen that the level of the scattered light is higher under the bridge closest to the centre of the galaxy, suggesting that additional scattered light from the galaxy is also present, and that if the scattered light was subtracted off, the flux level on the far side of the CCD would increase towards the edge.

wavelengths did not appear to significantly affect the spectral range used for the science analysis. However, as a precaution, the bluest parts of the spectra of all the galaxies in the sample were cut, shifting the starting wavelength of the spectral range from ~ 3980 Å to ~ 4300 Å, to remove those parts that could not be background subtracted reliably and maintain a constant wavelength range over the full sample. Inevitably, a low level of residual scattered light will remain in the data, requiring us to be careful in subsequent analysis.

2.2.7 Flux Calibration

The penultimate step in reducing the science spectra is to flux calibrate the spectra, where the measurements in counts are converted into an absolute flux value with units of erg s^{-1}cm^{-1}Å^{-1}. To carry out this correction, a spectrophotometric standard star was observed for each programme of observations with the same

Table 2.3: Spectrophotometric (S) and template (T) stars observed with the Virgo Cluster data.

Name	T/S	Spectral Class
Feige66	S	-
Hiltner600	S	-
LTT1788	S	-
HD054719	T	K2 III
HD070272	T	K5 III
HD072324	T	G9 III
HD073593	T	G8 IV
HD120136	T	F6 IV
HD144872	T	K3 V
HD145148	T	K0 IV
HD161817	T	A2 VI

instrumental set up, of which the details are given in Table 2.3. These stars were reduced in the same way as the science spectra, and then used to produce a sensitivity function with which to correct the science spectra. The sensitivity function lists the conversion from counts to flux at each wavelength in the spectrum. It is created by comparing the measured counts at each wavelength in a one-dimensional spectrum of a spectrophotoemtric flux standard star with the flux measurements expected at those wavelengths for that star. The necessary conversion of counts to flux can then be calculated as a function of wavelength, producing the sensitivity function which can be applied to the science spectra for flux calibration. The sensitivity functions assume that slit losses, transparency and seeing conditions were similar for observations of both the standard star and the galaxies.

Before applying the flux calibration to the science spectra, they were first corrected for the effects of atmospheric extinction, using the airmass at the midpoint of the integration for each exposure to apply an appropriate correction as derived from the KPNO extinction table of Stone & Baldwin (1983). Finally, each science frame was divided by the exposure time, and the absolute flux calibration applied using the sensitivity function derived from the relevant standard star.

2.2.8 Template stars

In order to match the composite spectral type of the galaxy during the kinematic analysis outlined in Sections 3.1 and 5.2, we need observations of template stars with a range of spectral properties. Therefore, observations of eight template stars were also requested, as listed in Table 2.3, which were reduced in the same way as the science images, as described above. Finally, a one-dimensional spectrum with a high S/N was extracted for each star.

2.2.9 Combining Multiple Exposures

As can be seen in Table 2.2, each galaxy was observed multiple times with different wavelength set ups in order to build up the S/N of the final image while ensuring a full spectral coverage over the gaps between the CCDs. Therefore, the final step in the data reduction was to combine these individual science exposures to produce the final spectrum for each galaxy, an example of which is given in Fig. 2.4.

Before combining the images, the alignment on the CCD of each galaxy was checked by comparing the measured positions of the peak of the spectrum over the full wavelength range to align the data spatially, and measuring the centres of prominent sky lines to ensure the best possible registration of absolute wavelength calibration. In all cases, the maximum offset between different exposures was found to be of the order of 0.5 pixels, and so no further corrections were necessary. The individual images were then combined, rejecting the highest value measured by each pixel in order to remove any residual cosmic rays in the images.

After reducing all the science spectra in this way, a high-quality two-dimensional spectrum was obtained for each galaxy, each one representing typically 1–3 hours of integration on an 8-metre telescope. The quality, resolution and data reduction steps presented here closely match those of the Fornax Cluster sample, and, to-

gether, these two data sets constitute a sample of long-slit spectra of 30 S0 galaxies extending right out into the outskirts of the discs. The resulting high quality of the data, generally with a signal-to-noise ratio in excess of 100 over the central 2 arcseconds of each galaxy, allows us to carry out the novel analysis described in the next chapter, whereby we decompose the light profile of each galaxy at each finely-separated wavelength, and thus obtain independent one-dimensional bulge and disc spectra for these S0s, from which their star-formation histories can be studied with minimal contamination.

Chapter 3

Spectroscopic Bulge–Disc Decomposition

Bulge–disc decomposition has long been applied to images of galaxies in order to understand how the luminosity and size of each component vary across galaxies of different morphologies and in different environments, which can provide information on how the star formation was induced or quenched throughout the galaxy, and thus how the galaxy formed (Kormendy, 1977; Burstein, 1979; Kent, 1985). With multi-waveband photometry, such as Bothun & Gregg (1990) and Peletier & Balcells (1996), colour information can be added to the analysis, where colour gradients between the bulges and discs act as indicators of the presence of age and metallicity gradients across the galaxy, thus providing more detailed information on the star formation history. The next logical step for bulge–disc decomposition analysis is to apply the technique to spectra in order to reduce the age-metallicity degeneracy in the study of the stellar populations within each component, and obtain more detailed information about the bulge and disc stellar populations and the processes that quenched their star formation.

Conventional photometric bulge–disc decomposition of galaxies in one dimension involves measuring the luminosity of the galaxy against radius along the major axis, and then fitting this light profile with a combination of bulge and
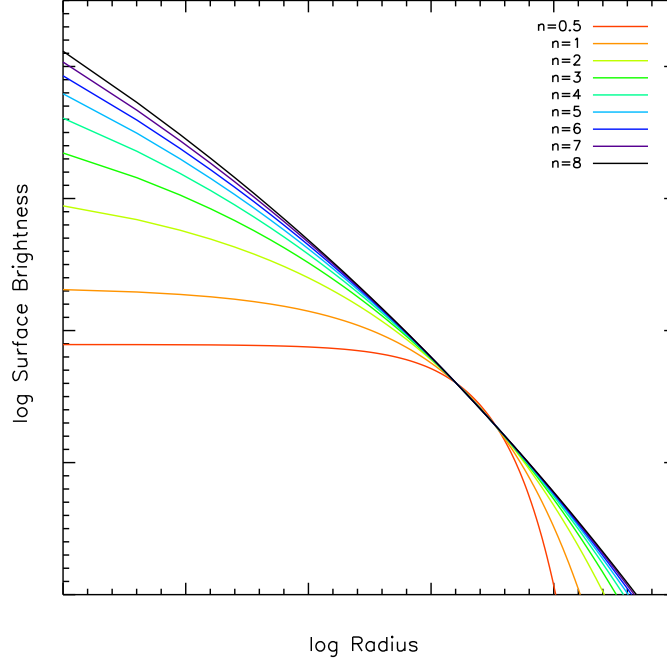
Figure 3.1: A demonstration of how the Sérsic profile varies with n.

disc profiles to find the best fit. Bulges are generally modelled as a Sérsic profile,

$$I_{\mathrm{B}}(R) = I_{\mathrm{Be}} \exp \left\{ -b_n \left[(R/R_{\mathrm{e}})^{1/n} - 1 \right] \right\}, \tag{3.1}$$

where R_{e} is the bulge effective radius, I_{Be} is the bulge effective surface brightness, n is the Sérsic index and b_n is a variable related to n in the form

$$b_n = 1.9992n - 0.3271 \tag{3.2}$$

(Sérsic, 1968). Examples of how the Sérsic profile varies with n are given in Fig. 3.1, where the shape changes from being Gaussian at $n = 0.5$ to becoming centrally concentrated with very extended wings as n increases. Classically, bulges were found to have a Sérsic index of 4, which is also known as the de Vaucouleurs profile (de Vaucouleurs, 1953), and so those bulges with $n \sim 4$ are known as classical bulges. Their similarity with elliptical galaxies, such as their old stellar populations and Sérsic indices around 4, have led to many theories that these bulges formed through similar mechanisms to ellipticals, i.e. through hierarchical clustering and mergers (Toomre, 1977b; White, 1997). However, bulges

have now been shown to have a range of Sérsic indices, where those with $n \sim 1$ are known as pseudobulges. Since bulges with smaller values of n have been shown to contain younger stellar populations and to be more rotationally supported than classical bulges, pseudobulges are thought to have formed through secular evolutionary processes, such as the inward movement of gas through the disc that slowly builds up a bulge, (Kormendy & Illingworth, 1982; Kormendy, 1982; Carollo et al., 1997; Gadotti & dos Anjos, 2001). When viewed edge on, many pseudobulges have been found to display a boxy or peanut shape, which is distinctive evidence of a bar that has formed through similar secular processes, and thus adds weight to these formation theories (Athanassoula, 2005).

Discs are also generally modelled with $n = 1$, but rearranged to form the exponential profile,

$$I_{\mathrm{D}}(R) = I_{\mathrm{D0}} \exp(-R/R_0), \tag{3.3}$$

where I_{D0} is the central surface brightness of the disc and R_0 is the disc scale length (Freeman, 1970).

Using these models to represent the bulge and disc, the light profile of any disc galaxy can be decomposed into these two components, although in many cases features such as bars, rings, thin and thick discs etc. provide additional complications to the galaxy and need to be modelled as well to achieve a reliable decomposition.

This technique can similarly be applied to a high-quality two-dimensional spectrum of a galaxy, aligned with the major axis, to decompose the light profile at each finely-separated wavelength into bulge and disc components. The decomposition will provide information on the size and luminosity of each component at each wavelength, which can be used to build up two one-dimensional spectra representing purely the bulge and disc light. From these spectra, independent analysis of the bulge and disc stellar populations can be determined with minimal contamination, leading to a better understanding of how the star formation in spirals was quenched to produce the S0s we see today. In this chapter, the

decomposition technique will be described in detail, using VCC 698 from the Virgo Cluster sample throughout as an example for each step, and identifying those issues unique to the decomposition of spectra.

3.1   Kinematics Corrections

The main complication when decomposing spectra in this way is accounting for the velocity dispersion and radial velocity over the galaxy, where the velocity dispersion decreases at larger radii, while the rotational velocity red- or blue-shifts the spectra at larger radii relative to that from the centre of the galaxy. Therefore, before fitting the light profile at each wavelength, the two-dimensional spectrum must be corrected such that each spectral feature has the same velocity dispersion and radial velocity, thus ensuring that the light profiles for each wavelength bin measures the light from the same point on the rest-frame spectrum at all radii and preventing any artificial distortions arising in the final bulge and disc spectra. Extra care must be taken with this correction when a bar is present within the galaxy to account for its kinematics.

The first step necessary for these corrections was to radially bin the two-dimensional galaxy spectrum into one-dimensional spectral bins at different radii with sufficient signal-to-noise (S/N) to allow their kinematics to be measured accurately. The binning was applied to the galaxy spectra prior to the flux calibration step, while the spectra are in units of electrons, and the S/N for each spectrum at each radius was calculated using the CCD equation,

$$\frac{S}{N} = \frac{N_*}{\sqrt{N_* + n_{\mathrm{pix}}(N_{\mathrm{S}} + N_{\mathrm{R}}^2)}}, \tag{3.4}$$

where N_* is the total number of photons collected from the spectrum, n_{pix} is the number of pixels over which the photons were collected, and N_{S} and N_{R} are the total number of photons per pixel from the sky background and the readout noise respectively. Working from the centre of the galaxy spectrum, spectra in adjacent rows were summed together until the total S/N for the binned spectrum
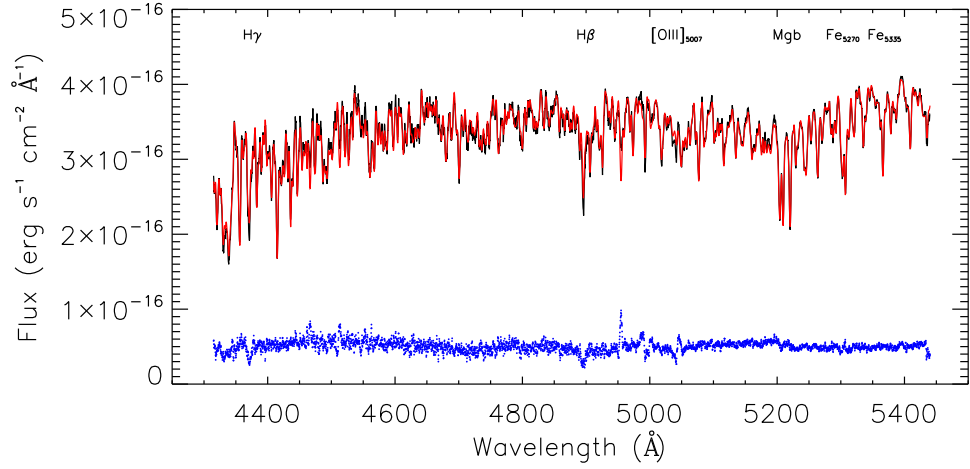
Figure 3.2: An example of how PPXF fits stellar templates to the centrally-binned spectrum of VCC 698, showing the original spectrum in black, the best fit model overplotted in red, and the residuals from subtracting the model from the original spectrum below in blue, offset from zero by an arbitrary amount.

reached a minimum value of 70 per Å. This step was repeated radially outwards from the centre of the galaxy until no more bins with this S/N could be created, at which point the minimum value for the S/N was dropped to 50, and then to 30, and finally to 20 as the binned spectra moved deeper into the outskirts of the galaxy. The binned spectra were then assigned a radius, which was taken to be the radius at which the total number of counts within that binned spectrum is split in half, and the kinematics measured using the Penalized Pixel Fitting method (PPXF) of Cappellari & Emsellem (2004). Figure 3.2 demonstrates how PPXF uses the template stellar spectra from Table 2.3 to produce best-fit models to the centrally-binned spectrum of VCC 698 by modelling the line-of-sight velocity distribution as a Gaussian with a series of Gauss-Hermite polynomials, from which the line-of-sight velocity distribution can be obtained. By repeating this analysis for all the binned spectra for a galaxy, the radial velocity and velocity dispersion profiles can be obtained, examples of which are given in Fig. 3.3 for VCC 698 and in Appendix A for all the Virgo Cluster galaxies. The errors in the measurements were calculated by running a series of Monte Carlo simulations – in each simulation, a model was created for the binned galaxy spectrum by
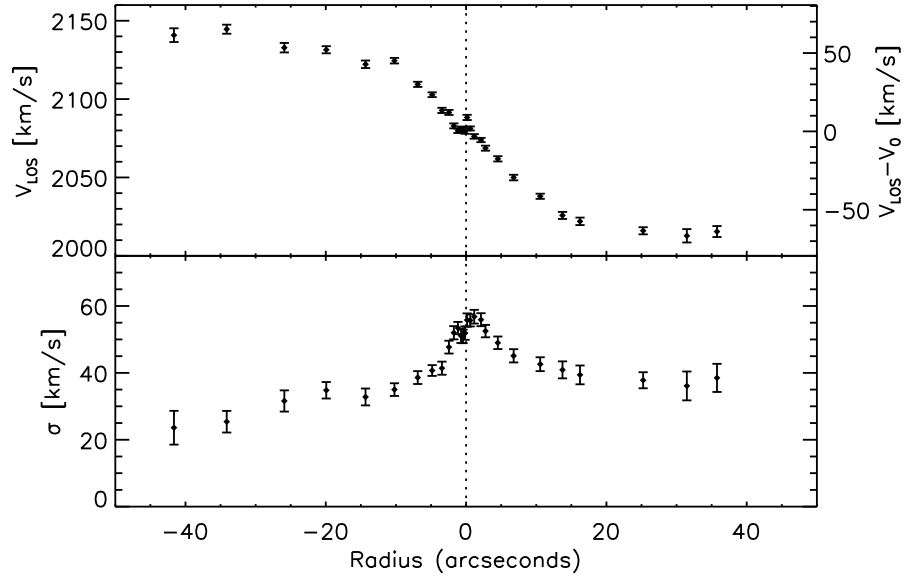
Figure 3.3: Kinematics plots for VCC 698, showing the line-of-sight velocity against radius in the top plot, with the offset from the velocity of the centre of the galaxy on the right axis, and the velocity dispersion on the bottom.

convolving the best combination of template spectra with the appropriate line-of-sight velocity distribution, and then degrading them to the S/N of the original spectrum. The model was then passed through PPXF to measure the uncertainty in the measurements of the kinematics for that spectrum. This step was repeated 1000 times for each binned spectrum to build up a true representation of the uncertainty in the measurements for that spectrum, and the standard deviation in the difference between the input and output measurements used as the error on the results in Fig. 3.3 and in Appendix A.

Having created the kinematics plots for the galaxy, the radial velocity of the centrally binned spectrum within that galaxy and the maximum velocity dispersion of the galaxy were identified. The velocity dispersion correction was applied by convolving the spectrum from each spatial location with the appropriate Gaussian to bring it up to the maximum value measured within that galaxy. The rotational velocity was then calculated by cross-correlation, where the shift in the wavelength of the spectral features at each location was measured relative to

those in the peak spectrum. Plotting the velocity dispersion corrected kinematics in this way acted as a good check for the initial velocity curves, such as in Fig. 3.3, to ensure that no kinematic features such as bars had been lost through using too large bin sizes. A rolling average was then applied to the velocity dispersion corrected kinematics curve by replacing the value of each spectrum with the mean value of that spectrum and the 5 spectra either side (i.e. ± 1.45 arcsec). Finally, the results were further smoothed by converting the velocity shifts into pixel shifts, and taking the integer values for the shifts. This technique worked well for regions of the two-dimensional spectrum with high signal-to-noise, and so in the outer regions, where the noise dominated the results, the final reliable shift was applied to the remaining rows. Since many of the galaxies in the sample were only offset slightly from the centre of the CCD, enough coverage of both semi-major axes of each galaxy was obtained, thus allowing their kinematics to be analysed separately. This duplication was useful to ensure the results were reproducible for each galaxy, and can also provide information on spatial asymmetries within the galaxies.

3.2 Decomposition of the Light Profiles

Once this velocity alignment has been carried out, the bulge–disc decomposition can be performed at all wavelengths. As a first approach, the galaxies were modelled using a de Vaucouleurs profile for the bulge and an exponential profile for the disc. However, this combination of fits was found to limit the ability to fit galaxies if their light profiles were not well described by this model, and so, to increase the flexibility of the fitting process, the full sample was decomposed using a Sérsic bulge profile and an exponential disc profile. By way of demonstration, examples of such fits to light profiles at individual wavelengths in the long-slit spectrum of VCC 698 are given in Fig. 3.4, showing the galaxy light profile along the major axis, the individual fits using Sérsic bulge and exponential disc profiles, and the best fit achieved by combining these fits to produce
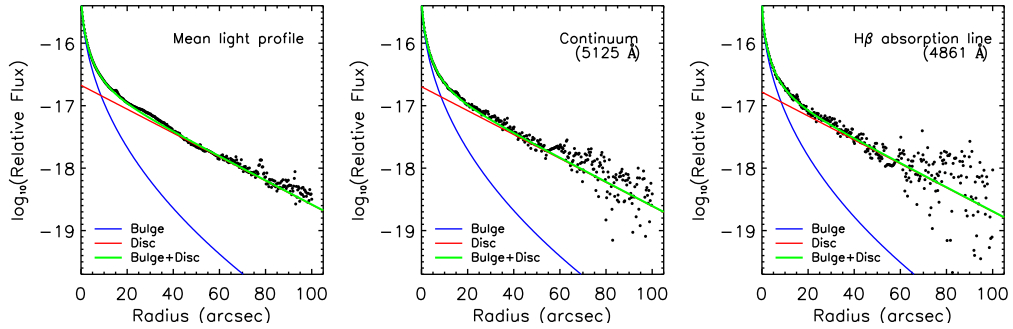
Figure 3.4: The best fits to the mean light profile for VCC 698 (left), and example light profiles taken from one column of pixels within the continuum (middle) and within the Hβ absorption feature (right). The bulge, disc and bulge + disc profiles are represented by the blue, red and green lines respectively.

the final model. The best fits to the mean profile of the rest of the galaxies in the sample are given in Appendix B. An alternative visualization is given in Fig. 3.5, showing a small section of the two-dimensional models produced for VCC 698 for the bulge, disc and composite galaxy centred on the Mg triplet feature, as derived by fitting the spatial profile of the two-dimensional spectrum (also shown) wavelength by wavelength. In each profile, the central few arcseconds were masked out prior to fitting in order to eliminate the effects of seeing, so the peaks of the bulge and disc spectra at very small radii in Fig. 3.5 were not used in the fit.

Prior to running the decomposition on the light profile at each individual wavelength, reasonable initial estimates for each parameter were needed. To obtain such values, the two-dimensional spectrum was compressed into one single, mean light profile for that galaxy, which could then be decomposed in the same way to find the best fit, as shown in Fig. 3.4. At this stage, the fits were checked by eye to ensure a good fit, in which case the best fit parameters were taken as initial estimates for the decomposition at each wavelength. In each case, the light profile was fitted from an inner distance of 2" out towards the edge of the CCD where the light profile levelled off. The inner distance of 2" was selected to eliminate the effects of seeing – as can be seen in Table 2.2, the maximum value recorded for the seeing FWHM during any of the observations was 1.8".
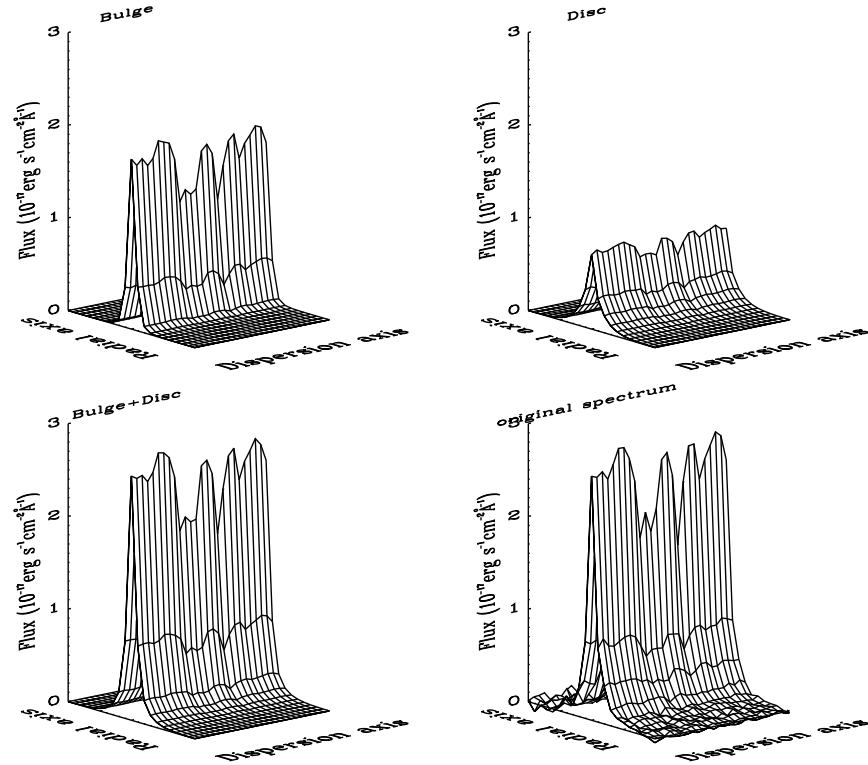
Figure 3.5: A section of the two-dimensional spectra for the bulge, disc and composite models, and the original spectrum of VCC 698, showing how the light profile varies with wavelength. The data have been binned such that each step in the radial direction is 14.5", and in the dispersion direction is 2.4Å. The models are centred on the Mg triplet, with wavelength increasing towards the right of the diagrams.

Additionally, any other features that appeared in the slit, such as foreground stars or background galaxies, were masked out in the light profiles to reduce contamination from those sources. In such cases, the seeing measurements were used as a guide to the size of such features, and the mask was centred at the peak of the contaminating light. The masks were then checked by eye ensure they covered the full size of the affected area, and broadened as necessary to cover the full size of the contamination, particularly in cases with a background galaxy. Having fitted the light profile for each galaxy, the fit was considered to be good if, for example, the Sérsic and exponential profiles represented the inner and outer parts of the light profile respectively, and the residuals plotted against radius were minimized. In general, the residuals between the mean light profiles and their best fits were of the order of $\sim 1 - 2\%$ for the Virgo Cluster sample for the

regions over which they were fitted. Additionally, since many of the galaxies in the sample were offset only slightly from the centre of the slit, it was possible to further test the reliability of the initial parameters by carrying out an independent decomposition of both semi-major axes to ensure that they were consistent with each other. In all but one galaxy in which both semi-major axes could be decomposed, the decomposition parameters were found to be consistent with each other. This consistency can be seen in the small errors listed in Table 3.1 for such galaxies, marked with a [†], where these errors include both the uncertainties in the individual fits for both sides of the galaxy and the difference between both sets of measurements. For those galaxies in which only one semi-major axis could be decomposed, the errors listed simply describe the uncertainty from the best fit.

Having identified the best fit parameters for the mean light profile for each galaxy, the individual light profiles at each wavelength could then be decomposed using these results as initial paramters for the wavelength-dependent fits. However, it was found that if all the Sérsic bulge and exponential disc parameters were left free for the full spectral fit, the results over the entire wavelength range became very unstable. This instability was most likely due to a combination of degeneracy issues from having too many free parameters for each one-dimensional fit. Therefore, to reduce this degeneracy, the light profiles were fitted with fixed values for R_e, R_0 and n, where these values were taken from the fits to the mean light profile for that galaxy. As a result of these limitations, only the bulge effective surface brightness and the disc central surface brightness were allowed to vary as a function of wavelength. Figure 3.6 presents examples of the offsets in the de Vaucouleurs and exponential profiles that can be achieved with a fixed effective radius and scale length, and only allowing the surface brightness to vary. However, before applying these limits to the fits over the full spectrum, random light profiles at different wavelengths, both within the continuum regions and spectral features, were checked by eye to ensure that no significant bias was inflicted on the results by holding these parameters fixed. Examples

Table 3.1: Results for the decomposition parameters and kinematics measurements for the decomposed bulge and disc spectra.

Name	Cluster	R_{e} [arcsec]	R_0 [arcsec]	n	V_{LOS} [km s^{-1}]	σ_0 [km s^{-1}]
(1)	(2)	(3)	(4)	(5)	(6)	(7)
VCC 798	Virgo	8.9 ± 0.3	61.5 ± 0.6	1.87 ± 0.14	741 ± 5	181 ± 7
VCC 1062	Virgo	8.7 ± 0.2	36.5 ± 0.6	1.30 ± 0.09	547 ± 4	199 ± 7
VCC 2092	Virgo	8.74 ± 0.15	67 ± 2	1.41 ± 0.07	1316 ± 4	194 ± 8
VCC 1692†	Virgo	4.5 ± 0.4	22.4 ± 0.3	1.6 ± 0.4	1727 ± 3	217 ± 6
VCC 2000†	Virgo	2.43 ± 0.05	9.7 ± 0.7	0.91 ± 0.08	1110 ± 5	267 ± 8
VCC 685	Virgo	2.87 ± 0.16	16.39 ± 0.14	0.8 ± 0.2	1209 ± 5	200 ± 8
VCC 1664†	Virgo	9 ± 3	19.9 ± 0.3	3.5 ± 1.4	1148 ± 10	207 ± 17
VCC 944†	Virgo	14 ± 5	31.4 ± 0.5	3.9 ± 1.1	834 ± 4	146 ± 5
VCC 1720†	Virgo	7.4 ± 0.5	38.0 ± 1.7	1.9 ± 0.4	2316 ± 2	119 ± 3
VCC 1883†	Virgo	2.9 ± 0.4	14.8 ± 1.9	2.3 ± 0.4	1767 ± 1.3	77 ± 2
VCC 1242†	Virgo	3.2 ± 0.2	15.7 ± 0.2	0.6 ± 0.2	1586 ± 2	80 ± 3
VCC 1303	Virgo	7 ± 2	27 ± 3	3.1 ± 0.6	897 ± 4	91 ± 6
VCC 698	Virgo	8 ± 4	22.4 ± 1.4	2.4 ± 1.4	2079 ± 2	52 ± 2
NGC1316	Fornax	16.7 ± 0.9	43.5 ± 3.6	0.62 ± 0.03	1716 ± 10	304 ± 19
NGC1380†	Fornax	15.7 ± 1.3	35.1 ± 2.4	1.85 ± 0.10	1790 ± 13	266 ± 22
NGC1381†	Fornax	3.2 ± 0.11	18.5 ± 0.7	0.94 ± 0.11	1717 ± 13	154 ± 19
NGC1375†	Fornax	4.2 ± 0.7	15.9 ± 0.9	1.9 ± 0.3	782 ± 9	116 ± 14
IC1963†	Fornax	–	15.3 ± 0.4	–	1634 ± 2	60 ± 3
ESO 358-G006†	Fornax	–	10.5 ± 0.3	–	1261 ± 6	99 ± 9
ESO 359-G002†	Fornax	–	7.4 ± 0.7	–	1449 ± 4	61 ± 5

Note. Column (1): Galaxy name; Column (2): Cluster; Column (3): Bulge effective radius; Column (4): Disc scale length; (5): Bulge Sérsic index; Column (6): Central line-of-sight velocity; Column (7): Central velocity dispersion. The errors represent one sigma uncertainties in the measurements, and the † symbol indicates those galaxies for which both semi-major axes could be analysed independently.
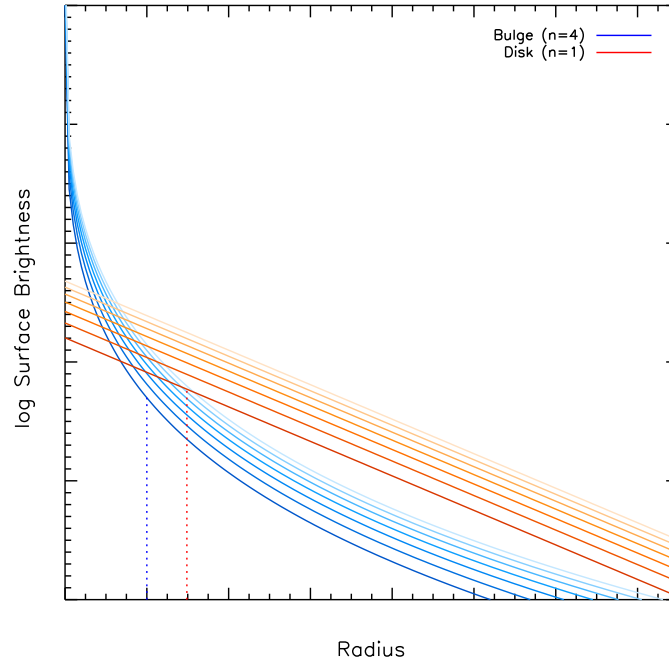
Figure 3.6: The effect of varying the surface brightness of de Vaucouleurs (blue) and exponential (red) profiles while holding their effective radii and scale lengths constant (vertical dotted lines). Lighter colours indicate increasing values for the bulge effective surface brightness and central surface brightness of the disc.

of these fits are given in Fig. 3.4, which presents examples of the best fit to the mean light profile for VCC 698, and the fits achieved for individual light profiles from the continuum and within the Hβ absorption feature. With this added constraint, the results from the decomposition over the full spectral range, and from both semi-major axes where applicable, became consistent with each other, and the co-added bulge and disc spectra bore a close resemblance to the original spectrum.

It was also hoped that by holding these parameters fixed in the fits, the effects of any residual scattered light (see Section 2.2.6) could be mitigated. Since the distribution of the scattered light on the CCD is different on the two sides of the galaxy, it was expected that contrasting results would be obtained from the decomposition of both semi-major axes if scattered light was compromising the results. However, the results for the decomposition parameters listed in Table 3.1 and the stellar populations analysis presented in Chapter 4 were found to be

consistent over both sides of each galaxy. Therefore, this consistency suggests that the results presented here are not affected significantly by contamination from scattered light.

Of the 30 galaxies in this data set, seventeen could be decomposed reliably using this method. Of the remaining thirteen, six (NGC 1380A, ESO 358-G059, VCC 2095, VCC 759, VCC 1913 and VCC 1938) showed more complicated light profiles due to the presence of dust lanes, secondary discs, rings etc. that could not be fitted by the simple bulge + disc model used here. Three more galaxies (IC 1963, ESO 358-G006 and ESO 359-G002) were found by Bedregal et al. (2006) to have very compact bulges and therefore to be disc dominated from very small radii, making it impossible to determine a reliable bulge model. For these systems a disc spectrum was extracted by assuming that the bulge light was negligible outside of the central masked region, and just fitting a disc component. A further two galaxies, VCC 1535 and VCC 1250 also show significant Hβ, [OIII]$_{\lambda 4959}$ and [OIII]$_{\lambda 5007}$ emission originating from nuclear discs in their central regions, which could not be accounted for in the light profiles with the simple model used in this study, and the faintest galaxy in the Virgo sample, VCC 1833, had too low a signal-to-noise ratio to fit both components reliably. The final recalcitrant galaxy was VCC 1619, which contains two counter-rotating stellar discs of similar mass and size, making it unsuitable for this type of decomposition. However, the opposing kinematics of the two discs in this galaxy produce distinctive cross-shaped absorption features, which can be used to disentangle their individual stellar populations. A description of this kinematic decomposition is outlined in Chapter 5.

Having obtained measurements for the effective surface brightness of the bulge and the central surface brightness of the disc of each galaxy as a function of wavelength, the total light from the bulge and disc at each wavelength can be obtained by integration. This integration was carried out using the trapezium rule between a distance of 2" from the centre, the inner limit used in the light profile decomposition for all galaxies, and the outer limits used in the in-

dividual fits, which depended on how far the galaxy was positioned from the edge of the CCD. By plotting these integrated luminosities against wavelength, one-dimensional spectra can be produced representing purely the integrated light from the bulge and disc. Examples of the integrated, decomposed bulge and disc spectra for each galaxy in the sample are plotted in Figures 3.7–3.10. If the kinematics corrections carried out on the binned spectra prior to decomposition were applied correctly, then these bulge and disc spectra would be expected to have matched line-of-sight velocities and velocity dispersions, which would correspond to the line-of-sight velocity at the centre of the galaxy and the maximum velocity dispersion measured within the galaxy. Therefore, the kinematics of these spectra were measured using PPXF again, and were found to be consistent. The values determined in this way are also given in Table 3.1. It is interesting to note that if the decomposition paramaters are reliable, the majority of galaxies in this sample appear to contain pseudobulges, with only three galaxies showing Sérsic indices of ≥ 2.5. This trend will be discussed in Section 3.3 with a comparison to literature results.

The high signal-to-noise ratio of the decomposed spectra obtained using this integrated light approach is immediately apparent. For example, it can be seen that in many of the galaxies, both the Hβ line and the magnesium triplet appear stronger in the bulge than in the disc. Since these features are used as age and metallicity indicators respectively, this difference already hints that the bulge contains younger stars with a higher metallicity than the disc in this galaxy. A more quantitative assessment of this impression will be made in Chapter 4.

3.3   Comparison with Decomposition of Images

The method outlined above is restricted by the use of long-slit spectra of the major axis only, which may introduce contamination in the stellar populations analysis due to the presence of structures such as dust lanes, bars, rings etc. that lie in the plane of the disc. More sophisticated methods of two-dimensional bulge–disc
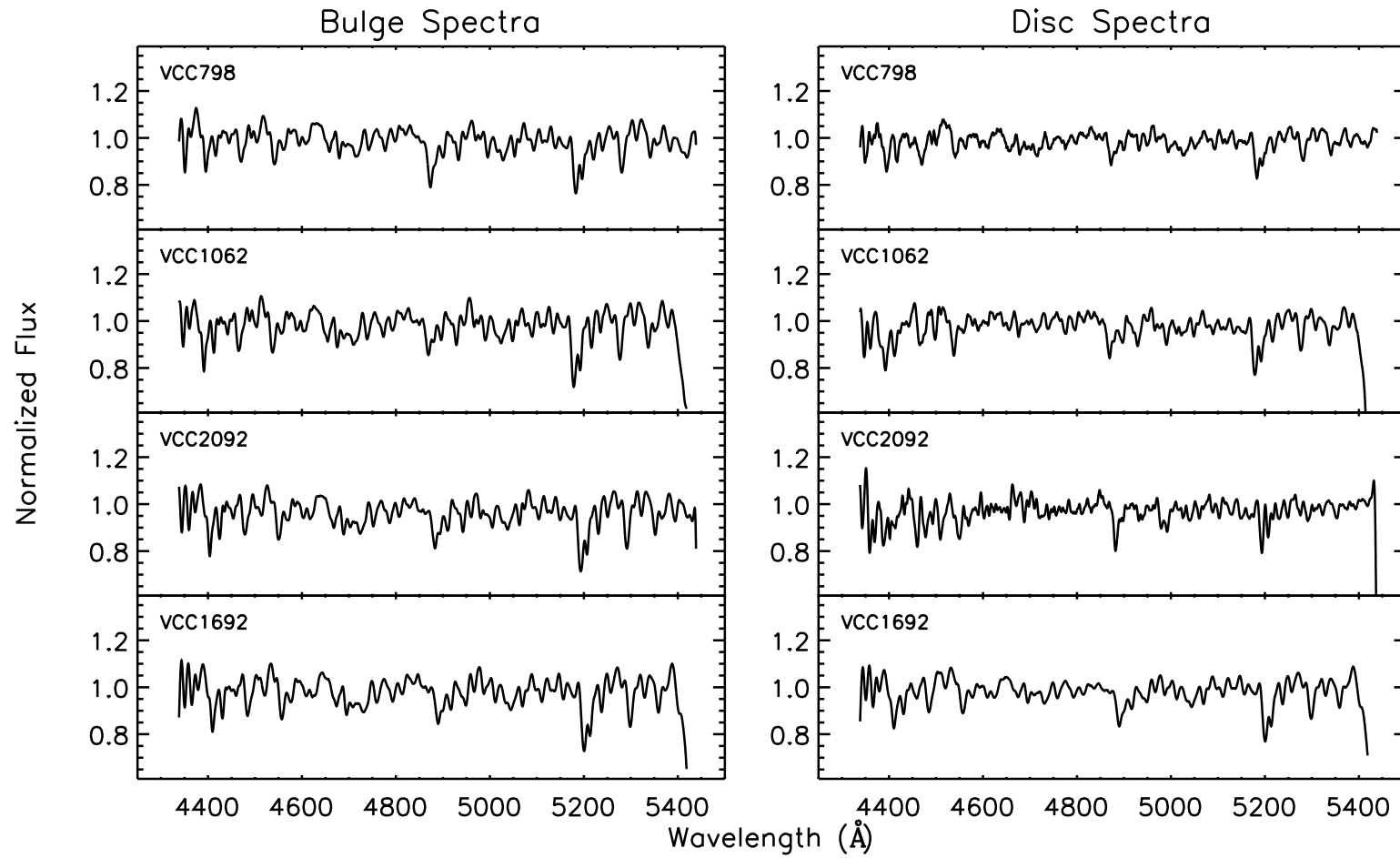
Figure 3.7: The decomposed bulge and disc spectra for the Virgo Cluster galaxies that could be decomposed with the Sérsic bulge + exponential disc model. Each spectrum represents the total integrated light from the bulge (left) or disc (right) of the galaxy listed in the top left corner of the spectrum.
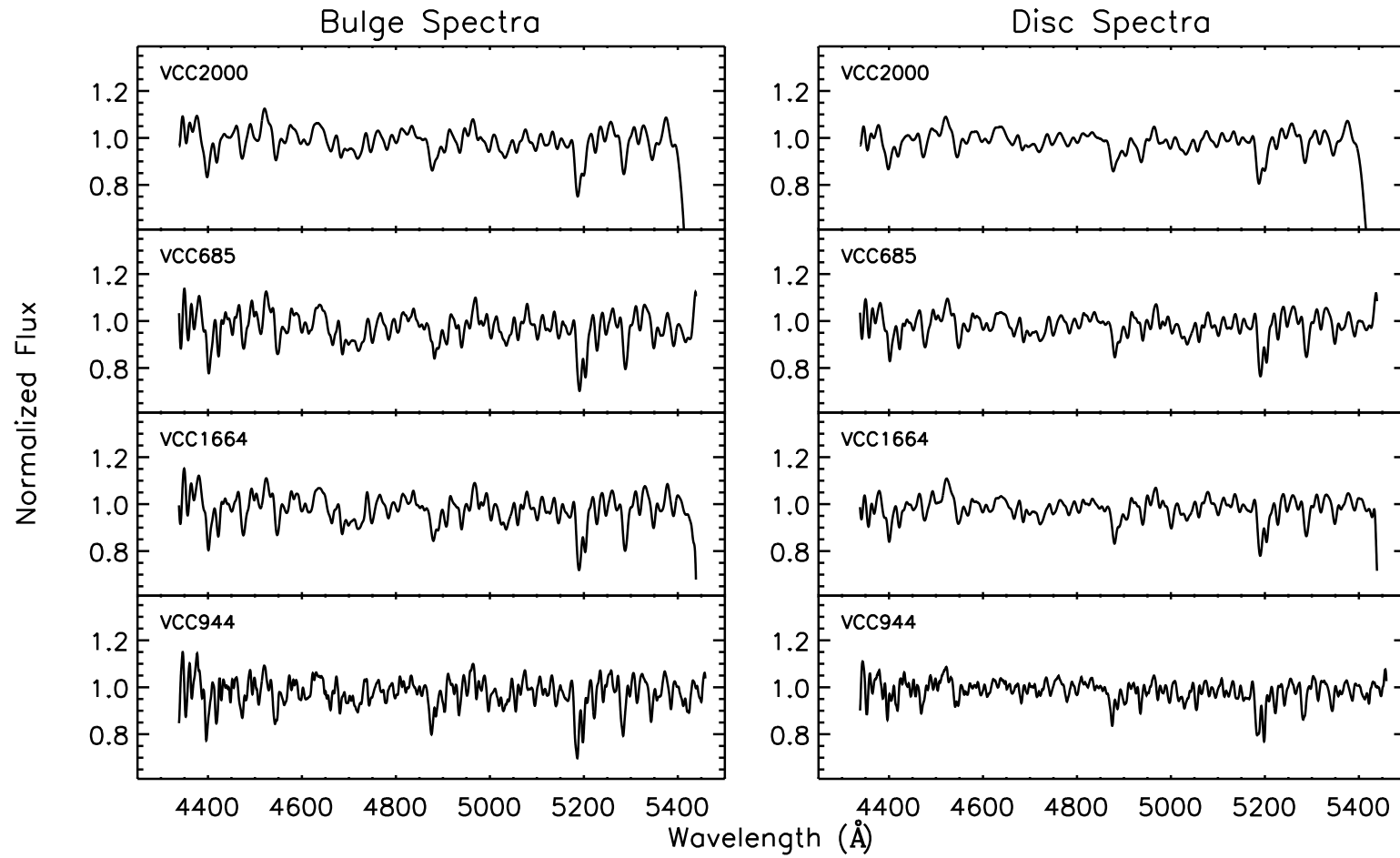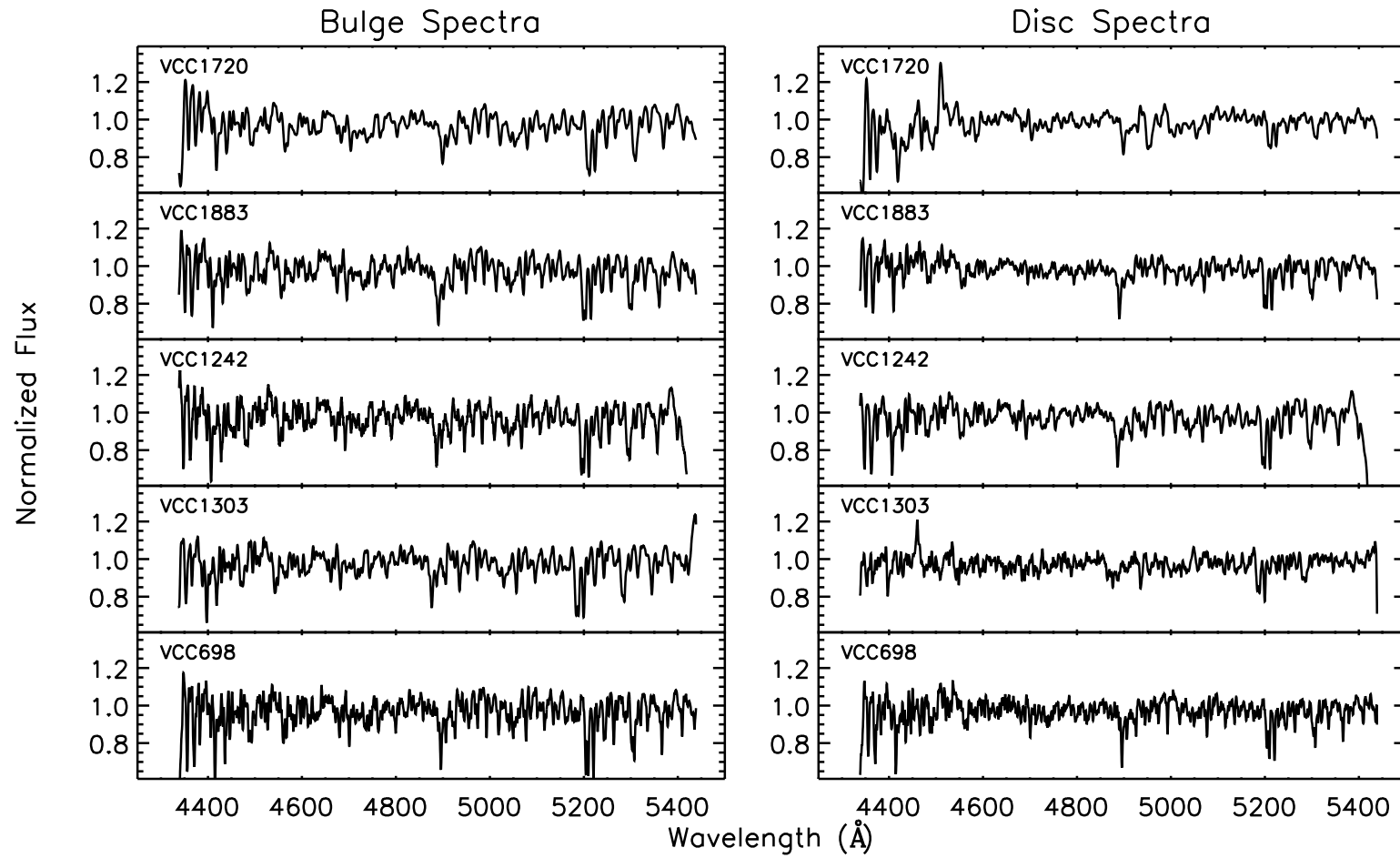
Figure 3.8: The decomposed bulge and disc spectra for the Virgo Cluster galaxies that could be decomposed with the Sérsic bulge + exponential disc model. Each spectrum represents the total integrated light from the bulge (left) or disc (right) of the galaxy listed in the top left corner of the spectrum.

Figure 3.9: The decomposed bulge and disc spectra for the Virgo Cluster galaxies that could be decomposed with the Sérsic bulge + exponential disc model. Each spectrum represents the total integrated light from the bulge (left) or disc (right) of the galaxy listed in the top left corner of the spectrum.
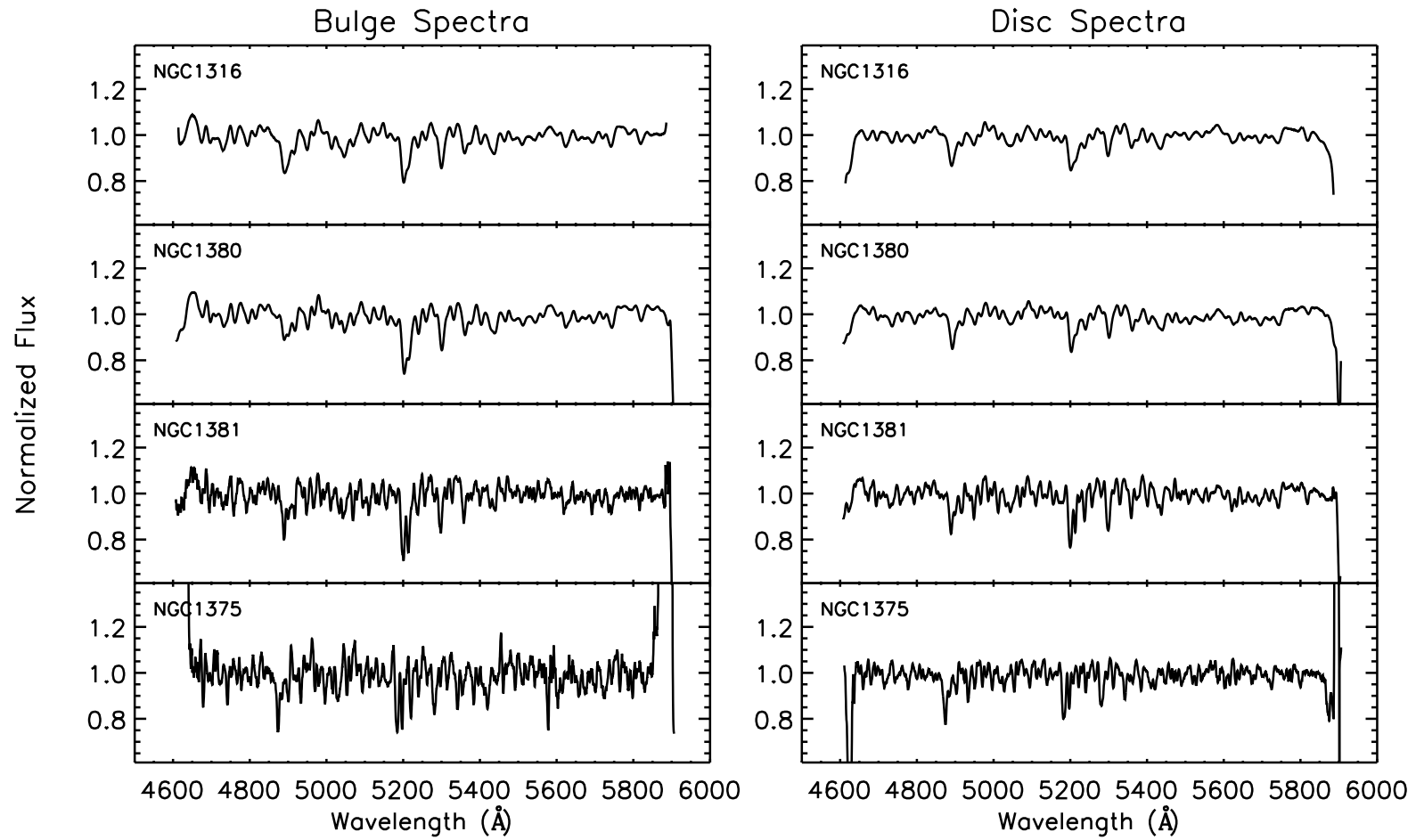
Figure 3.10: The decomposed bulge and disc spectra for the Fornax Cluster galaxies that could be decomposed with the Sérsic bulge + exponential disc model. Each spectrum represents the total integrated light from the bulge (left) or disc (right) of the galaxy listed in the top left corner of the spectrum.

decomposition applied to images of galaxies have the advantage that they can work around such features and thus obtain better measurements of the bulge and disc parameters using the full structural information available. It would therefore be interesting to see whether our simpler one-dimensional decomposition could be compromising the extracted spectra.

To this end, images of each Virgo Cluster galaxy were obtained from the SDSS DR7 (Abazajian et al., 2009), and mosaicked together with the MONTAGE software[1] to produce a large field of view for a two-dimensional photometric decomposition. The SDSS g-band images were selected because the central wavelength of this band, 4770 Å, lies closest to the central wavelength of the spectra, and the corrected (fpC) frames were used as they had already undergone bias subtraction and flat fielding as part of the *frames* pipeline (Stoughton et al., 2002).

The decomposition was carried out using the GALFIT image analysis software (Peng et al., 2010, v3.0.4), which is a two-dimensional parametric galaxy fitting algorithm. In order to compare directly to the spectral decompositions, the SDSS images were fitted with a Sérsic bulge and exponential disc profile. Each fit was also convolved with a PSF created for each galaxy by median stacking images of stars within the mosaicked image. The best fit model of each image and the residuals produced by GALFIT were checked by eye, and the software re-run with new initial parameters if the provisional fit was found to be poor. An example of the decomposition of VCC 698 with GALFIT can be seen in Fig. 3.11. Figure 3.12 presents the results for the bulge and disc sizes and bulge Sérsic index as measured from the SDSS images compared with those from the spectral decomposition, and show a good correlation between the two methods with some scatter which could be attributable to features within the plane of the disc as outlined above.

As a further test of the decomposition parameters, the results obtained from the long-slit spectra were compared with those from the literature. These results
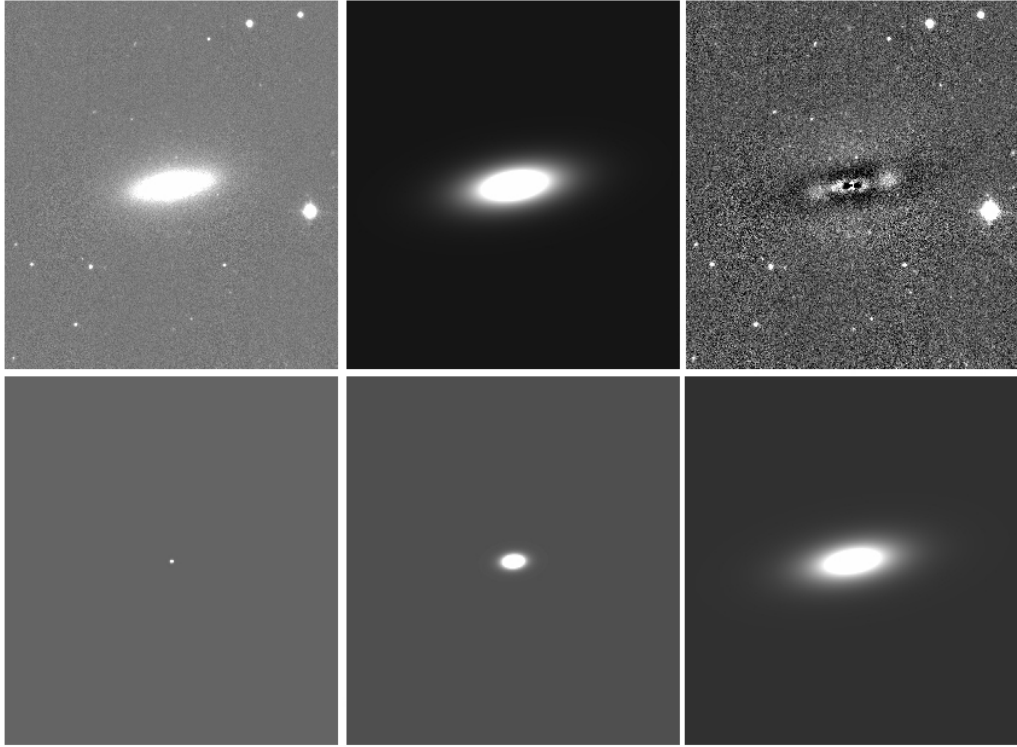
---

[1]http://montage.ipac.caltech.edu/

Figure 3.11: Example of the decomposition of VCC 698 with GALFIT. Along the top, from left to right are the original g-band SDSS image of the galaxy, the best-fit model from GALFIT, and the residuals after subtracting the best fit from the original image. In the residual image, a small dust disc can be seen in the bulge region. The bottom images represent the individual components that build up the best fit – the PSF (left), Sérsic bulge (middle) and exponential disc (right).

are plotted in Figure 3.13. To ensure full coverage of the sample of galaxies, bulge and disc paramteres for the Virgo Cluster galaxies were taken from Kormendy & Bender (2012) and McDonald et al. (2011), both of which used SDSS g-band images of the galaxies. A comparison was also carried out with Bedregal et al. (2011) for the Fornax Cluster galaxies, in which the decomposition was carried out using 2MASS K_S-band images of the galaxies. It is important to note that the results from Kormendy & Bender (2012) and McDonald et al. (2011) give the disc sizes as the disc effective radii, and so the disc scale lengths obtained from the long-slit spectra used here were converted into effective radii using $R_e = 1.678R_0$.

Comparison of Figs. 3.12 and 3.13 show similar levels of scatter. This scatter is partly due to the differences in the decomposition techniques used in each

study. For example, Bedregal et al. (2011) used K_s band images from the 2MASS survey which would be less affected by dust in the plane of the disc than the spectroscopic data, but would also be less sensitive to bluer light than the g-band images. Additionally, Kormendy & Bender (2012) applied their decomposition using double Sérsic profiles which, in four of the five overlapping galaxies (VCC 698, VCC 944, VCC 1062 and VCC 1720), resulted in very non-exponential profiles for the disc which might have affected the fit to the bulge as well.

Another likely contribution to the scatter would be dust in the plane of the discs, which may affect the decomposition of the spectroscopic light profiles more than the photometric data. There have been many studies looking at the effects of dust on the decomposition parameters of bulges and discs. For example, Gadotti, Baes & Falony (2010) found that the presence of dust can lead to over-estimations of the disc scale length and underestimations of the bulge effective radius and Sérsic index. Möllenhoff, Popescu & Tuffs (2006) proposed that the disc scale length measurements can be off by as much as 50% due to dust. A more recent study by Pastrav et al. (2013) agreed with Gadotti, Baes & Falony (2010) that dust causes overestimations in the disc scale length, and identified that while the effect is strongest in young stellar discs, old stellar discs are still affected, especially when fitted with exponential profiles. Similarly, they found that the bulge Sérsic index is also generally underestimated, especially at higher inclinations. However, Pastrav et al. (2013) also identified that the bulge effective radii tend to be slightly overestimated in the presence of dust, contradicting Gadotti, Baes & Falony (2010), and that this effect is stronger for de Vaucouleurs (classical) bulges than for exponential (pseudo-) bulges. Consequently, since the spectroscopic data consists of observations along the major axes of galaxies with inclinations of greater than 40°, it is likely that the parameters obtained from this data set are more affected by dust than the photometric data from the literature. Indeed, it can be seen in Figs. 3.12 and 3.13 that the bulge Sérsic indices and scale lengths do appear to be underestimated in general in the spectroscopic
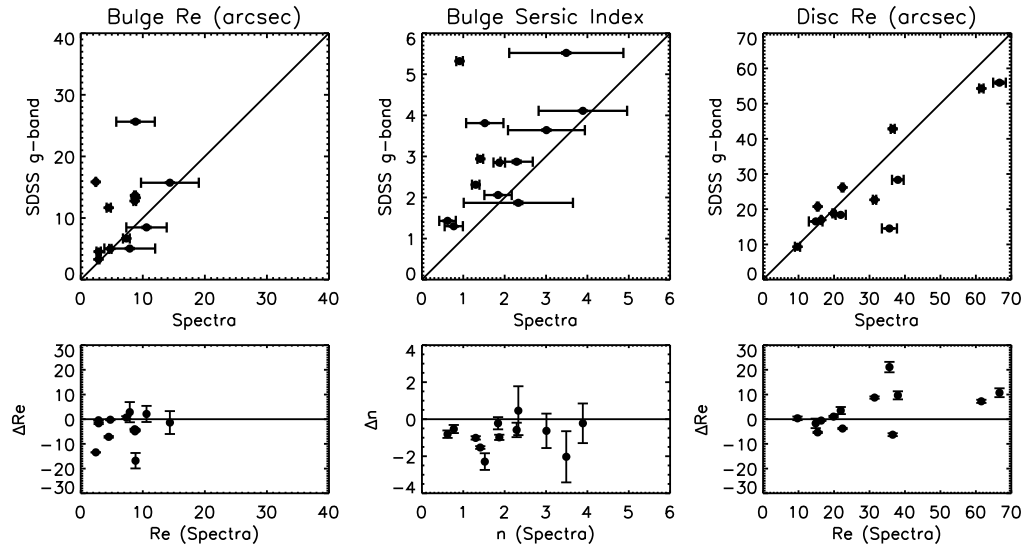
Figure 3.12: Comparison of the decomposition parameters as measured from the spectral decomposition method outlined above (x-axis) with those obtained from decomposing SDSS images of the same galaxies with GALFIT (y-axis). The top row of plots give the direct comparisons between the spectroscopic and photometric results, and the diagonal represents the one-to-one correlation. The bottom row plots the difference between the spectroscopic and photometric results against the spectroscopic results.
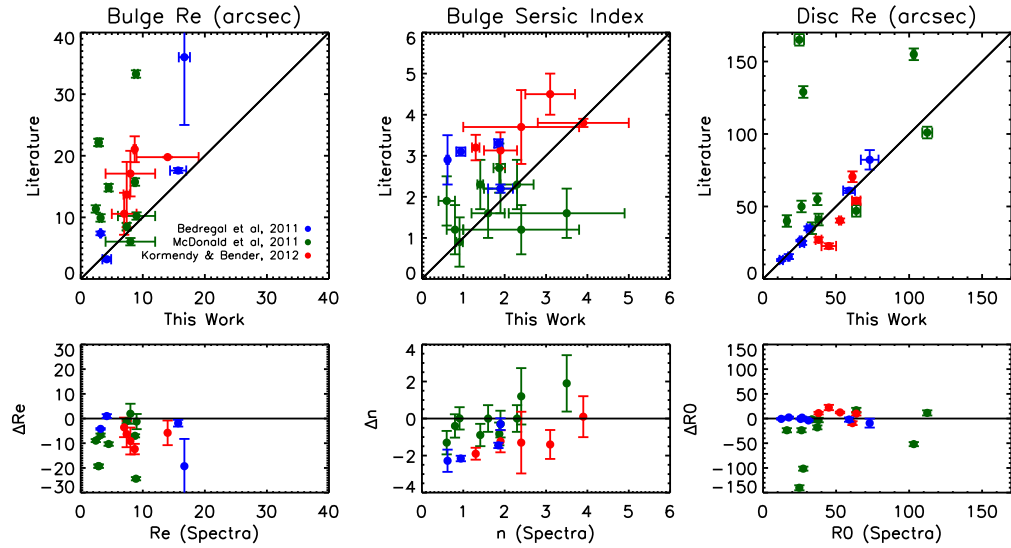

Figure 3.13: As for Fig. 3.12, but comparing the spectroscopic results with those from the literature. Blue points represent comparison of the Fornax Cluster galaxies with the results of Bedregal et al. (2011), while green and red points reflect the work of McDonald et al. (2011) and Kormendy & Bender (2012) respectively for the Virgo Cluster galaxies. Note that the right hand plots are for the disc effective radius, where the conversion $R_e = 1.678 R_0$ was used for the spectral results.

results, as predicted by Gadotti, Baes & Falony (2010).

It is interesting to note at this point that Table 3.1 showed only three galaxies that would be considered to have classical bulges, i.e. with Sérsic indices of greater than 2.5. The middle plots of Fig. 3.12 however suggest that the Sérsic indices derived through spectral decomposition is underestimated compared to those obtained through photometric decompositions at similar wavelengths. Figure 3.13 also shows a similar scatter among results from the literature – according to Bedregal et al. (2011), McDonald et al. (2011) and Kormendy & Bender (2012), only 56% (9 out of 16 overlapping measurements) of the total sample of galaxies used in this study are considered to be pseudobulges. Interestingly, two of the Virgo cluster galaxies, VCC 698 and VCC 1720, overlapped with both the McDonald et al. (2011) and the Kormendy & Bender (2012) studies, and in both cases were classified differently by each. Kormendy & Bender (2012) classed both galaxies as having classical bulges, with Sérsic indices of 3.7 and 3.13 for VCC 698 and VCC 1720 respectively, while McDonald et al. (2011) derived Sérsic indices of 1.2 and 2.2 respectively, suggesting that they both contain pseudobulges. As a result, it is unlikely that spectroscopic decomposition can distinguish between classical and pseudobulges with better accuracy than the more traditional photometric decomposition using purely long-slit spectra from the major axis of a galaxy. Consequently, this phenomenon may simply be the result of dust attenuation leading to underestimated Sérsic indices in these galaxies.

As a test of the impact of such systematic distortions, the spectra were decomposed again using fixed values for R_e, R_0 and n from the decomposition of the SDSS images and allowing only the amplitudes of the components to vary. As Fig. 3.14 shows, this test revealed little difference between the bulge and disc ages and metallicities from the original spectroscopic decomposition results (see Chapter 4) and those decomposed using the SDSS values, thus confirming that the spectral decomposition is fairly robust against such potential systematic errors in the bulge and disc parameters.
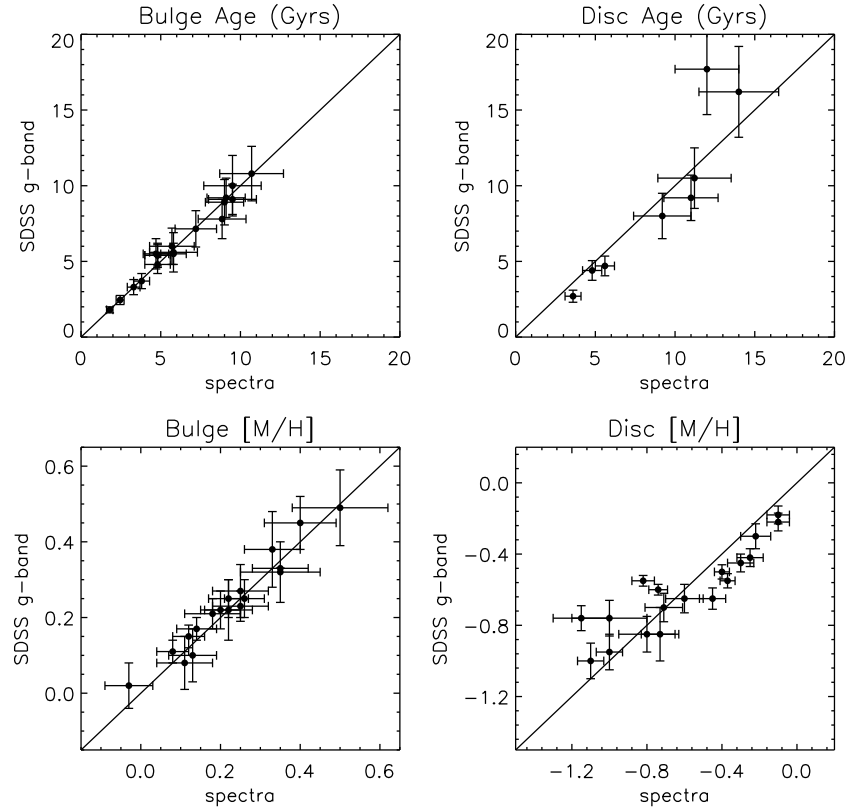
Figure 3.14: Comparison of the calculated ages and metallicities for the bulges and discs after decomposition using the spectral parameters (x-axis) and those measured from the SDSS image decompositions (y-axis). Note that the disc age plot does not include those galaxies where the Hβ line strengths lay below the SSP models in both analyses, and that both semi-major axes of the spectra were decomposed separately with the spectral and SDSS parameters.

3.4 Analysis of the Systematic Errors due to Kinematics

Another potential issue with the decomposition method is that the kinematic corrections applied before the decomposition could result in losing information on the bulge and disc star formation histories. For example, by broadening the spectrum to match the maximum velocity dispersion, information on the line strengths in the outer regions may be lost, resulting in less reliable measurements of the line indices, and thus compromising the stellar populations analysis. Similarly, the radial velocity corrections were carried out by measuring the overall offset in the spectrum from the centre of the galaxy, which does not take into

account the different rotational velocities that the bulge and disc will have.

In order to test the significance of these effects when decomposing the corrected two-dimensional spectrum, a series of simulated two-dimensional spectra were created and decomposed in the same way as the galaxy spectra. The model spectra were formed by co-adding spectra of known different stellar populations and velocity dispersions to represent the bulge and disc, where these co-added spectra were composite spectra obtained from the Vazdekis et al. (2010) single stellar population (SSP) models using the MILES stellar library (Sánchez-Blázquez et al., 2006). The proportion of bulge and disc light to add at each radius was determined by creating a model light profile based on typical measurements from the decomposition of the Virgo Cluster S0s, and the disc spectrum offset in the wavelength direction in order to simulate the rotational velocity of that component relative to a non-rotating model. As a final step, noise was added to the model spectra to simulate the uncertainties in the real measurements.

The simulated spectra were then decomposed in the same way as the galaxy spectra, and the stellar populations of the bulges and discs compared to the input values. As can be seen in Fig. 3.15 for one such test, the results were found to be consistent with the original stellar populations that went into the spectrum, thus indicating that the kinematic corrections described in Section 3.1 are sufficient to blur the individual kinematics of the bulge and disc to allow successful decomposition, while minimizing the information lost about the strengths of any features in the data.

3.5   Summary

A new method is presented for analysing S0 galaxy spectra by decomposing their major-axis light into bulge and disc components on a wavelength-by-wavelength basis, in order to construct clean, high-quality spectra for each individual component. Application of this technique to the full sample of galaxies described in Tables 2.1 and 2.2 has resulted in the successful decomposition of more than half
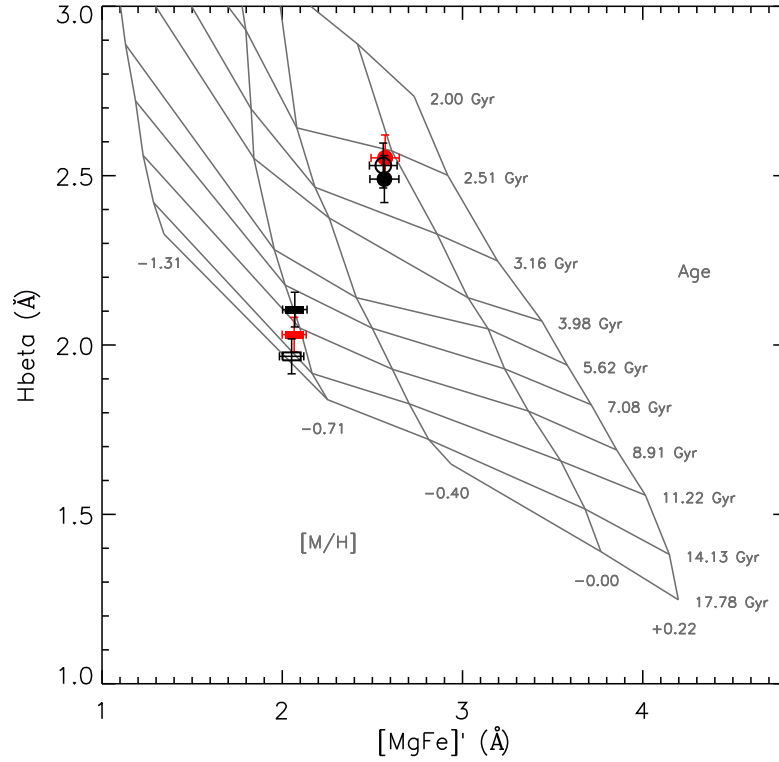
Figure 3.15: A comparison of the stellar populations of the template spectra used to create a simulated two-dimensional spectrum (red symbols) with the results obtained from decomposing this spectrum into bulge and disc components (black symbols, filled and open symbols represent measurements from both semi-major axes). The consistency in the input and output results indicate that the kinematics corrections applied before the decomposition is carried out does not significantly affect the line indices of the decomposed spectra.

of the total sample, producing high-quality spectra representing purely the bulge and disc light from each galaxy and revealing the kind of data required to implement this analysis successfully. It has been ascertained that in systems where the galaxies are well-described by this two component model, where both components are sufficiently resolved to allow a reliable structural fit, and where there is little indication of complicating issues like strong dust lanes or extra components such as bars, it is quite possible to spectroscopically decompose galaxies in this way. Fortunately, comparison between the original two-dimensional spectrum and the model offers a useful *a posteriori* check on the impact of such additional factors.

In addition to this technique, a separate decomposition was also developed

and successfully applied to VCC 1619, the Virgo Cluster galaxy with two counter-rotating stellar discs, in which the different kinematics of the two discs were used to separate their stellar populations, as described in Chapter 5.

With such unprecedented high-quality uncontaminated spectra of individual bulge and disc components of S0s, we are now in a position to use their individual star-formation histories to determine how the star formation in the progenitor spirals was quenched, and thus how S0s in nearby clusters formed.

Chapter 4

The Star Formation Histories of Bulges and Discs

Having established how to decompose a long-slit spectrum of a galaxy into clean bulge and disc spectra, we can now move onto analysing these spectra to learn about their individual star-formation histories. The analysis presented in this chapter uses the Lick/IDS indices measured from the decomposed spectra to study the stellar populations, both globally over the bulge and disc and any gradients within these structures. The resulting ages and metallicities will address the questions we have about S0 formation.

4.1 Ages and Metallicities

In the integrated light spectrum of a galaxy, the strength of the various absorption lines provides information on the underlying stellar population, with hydrogen lines primarily associated with its age, while magnesium and iron lines constrain its metallicity. The strengths of these absorption features were measured with the INDEXF software (Cardiel, 2010), which uses the Lick/IDS index definitions to calculate a pseudo-continuum over each absorption feature based on the level of the spectrum in bands on either side, and measures the strength of the feature
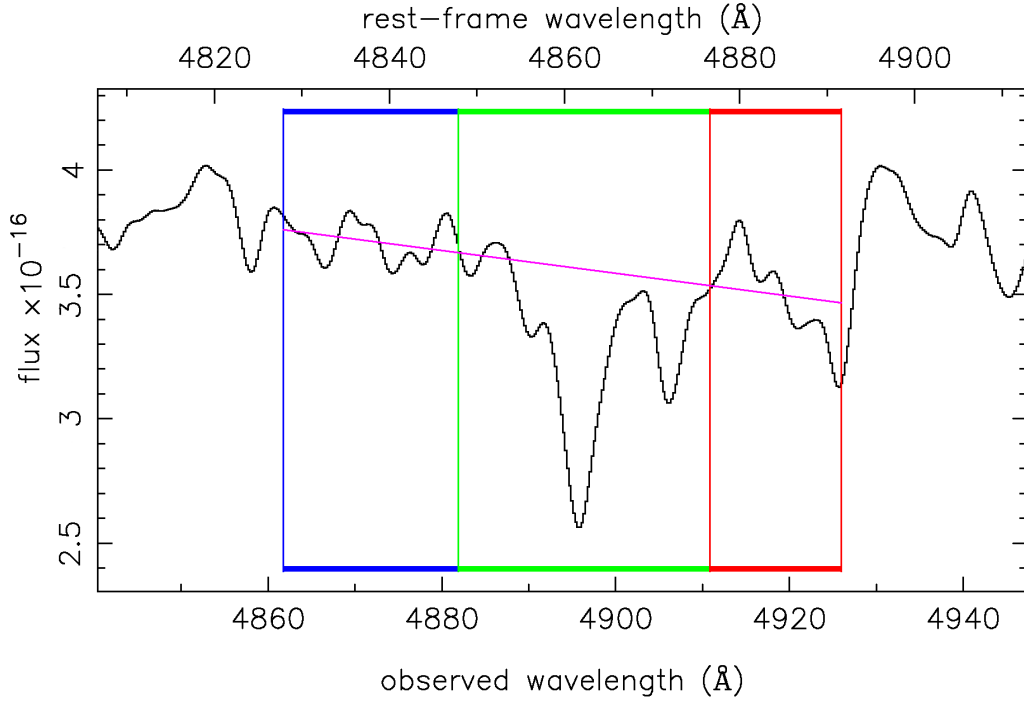
Figure 4.1: An example of the measurement of the Hβ line strength in the decomposed bulge spectrum of VCC 698. The blue and red boxes represent the two bands within which the pseudocontinuum is calculated, and the green band gives the wavelength region over which the strength of the feature is measured relative to the pseudocontinuum (magenta line)

relative to the pseudo-continuum (Worthey et al., 1994; Worthey & Ottaviani, 1997). By way of illustration, Fig. 4.1 demonstrates the measurement of the Hβ feature in the decomposed bulge spectrum of VCC 698, where the red and blue boxes mark the regions over which the pseudo-continuum (magenta line) is calculated, and the green box marks the area over which the line strength is calculated.

In order to obtain quantitative estimates of age and metallicity, these line indices are compared to those predicted by single stellar population (SSP) models that have been created using stellar libraries of the same spectral resolution as the data. The first step in creating an SSP model is to identify stars in the stellar library with similar ages and metallicities, and to obtain a mean estimate of their line indices. By repeating this process for stars of different ages and metallicities, pairs of derived line indices can be plotted to build up the SSP model. The model appears as a grid of age and metallicity estimates, with which the
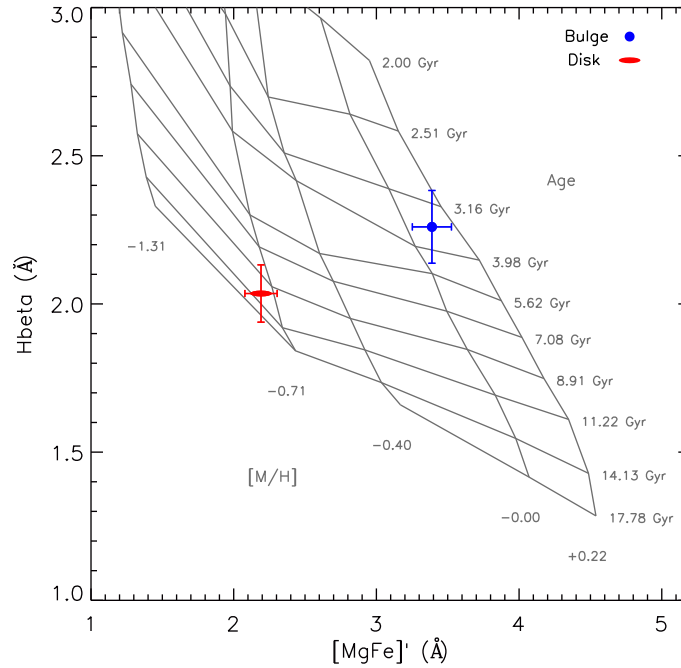
Figure 4.2: Example of the VCC 698 SSP model, with the line index measurements from the bulge and disc spectra over-plotted. The blue circle represents the bulge while the red ellipse corresponds to the disc value. The error bars represent the statistical uncertainties.

measured line indices from the decomposed bulge and disc spectra can be compared, as illustrated in Fig. 4.2. The light from galaxies however is not that of a single stellar population, instead consisting of multiple populations with different chemical compositions superimposed upon one another. If a recent star formation event has occurred within a galaxy, the light from the newly-created stars will temporarily outshine all other stars in that galaxy. As a result, they will dominate the light until the hottest, brightest stars die off, typically after a few billion years. Therefore, the age and metallicity of that galaxy as derived from an SSP model will be luminosity-weighted, and can provide information on how long ago the most recent star-formation event occurred, and the origin of the gas that fuelled it.

In this study, the Vazdekis et al. (2010) SSP models were chosen, which use the MILES stellar library (Sánchez-Blázquez et al., 2006). These models were preferred over more traditional models, such as Worthey & Ottaviani (1997) and

Bruzual & Charlot (2003), because the library spectra have a high resolution of $\sim 58.4\,\mathrm{km\,s^{-1}}$, meaning that the models can be matched to the spectral resolution of the data, as opposed to degrading the galaxy spectra to the lower resolution of the models. As a result, this process minimizes the loss of information that normally occurs when degrading the data to match lower-resolution models. To obtain the tuned SSP models for each decomposed spectrum, the stellar spectra were convolved with a Gaussian of the appropriate dispersion via a web-based tool[1] to match the resolution and redshift of the target. In the case of VCC 698, the velocity dispersion of the galaxy was lower than that of the library spectra, and so the decomposed spectra of this galaxy were instead broadened to 58.4 km s^{-1}.

To model the age and metallicity, the Hβ index and combined metallicity index,

$$[\mathrm{MgFe}]' = \sqrt{\mathrm{Mgb} \cdot (0.72 \times \mathrm{Fe}5270 + 0.28 \times \mathrm{Fe}5335)}, \qquad (4.1)$$

were selected, where the latter was chosen due to its negligible dependence on the α-element abundance (González, 1993; Thomas, Maraston & Bender, 2003). As a further slight complication, if any traces of emission are present in the Hβ feature, they would reduce the absorption-line strength of this feature and skew the results to older ages. González (1993) identified that the ratio between the equivalent widths of the [OIII]$_{\lambda 5007}$ and Hβ emission features is around 0.7 in the brightest ellipticals, while a later study by Trager et al. (2000) found the ratio to vary between 0.33 to 1.25 with a mean value of 0.6. Therefore, to correct for this contamination, the mean value from Trager et al. (2000) was used here to estimate the level of emission correction necessary for the Hβ index, using

$$\Delta(\mathrm{H}\beta) = 0.6 \times \mathrm{EW}[\mathrm{OIII}]_{\lambda 5007}, \qquad (4.2)$$

where the flux of the [OIII]$_{\lambda 5007}$ feature was measured from the residual spectrum obtained by subtracting the best combinations of stellar templates produced by PPXF from the original bulge and disc spectra (see for example Fig. 3.2), and

---

[1]http://miles.iac.es/

divided by the level of the continuum in the bulge or disc spectrum at that wavelength. For this sample, the majority of the corrections were only of the order of 5 per cent of the Hβ index, so any residuals from the approximate nature of this correction are unlikely to compromise the results significantly.

Having measured and corrected the line strengths, they could then be overplotted onto the tuned SSP models for each galaxy. The global, luminosity-weighted ages and metallicities of the bulge and disc were calculated by interpolating across the SSP model grid, and the errors shown reflect the statistical uncertainties in the line index measurements as estimated from the propagation of random errors and the effect of uncertainties in the line-of-sight velocities. Clearly in the example in Fig. 4.2, the bulge appears to contain a younger and more metal-rich stellar population than the disc.

This analysis was applied to all galaxies that were decomposed with the simple bulge-plus-disc model outlined in Chapter 3, with each semi-major axis compared independently where possible as a test of the reproducibility of the results. In general it was found that the line index measurements for the bulge and disc were consistent when compared for both halves of each galaxy. Hence, a single measurement for the properties of the bulge and disc stellar populations was derived for each such galaxy by taking the mean value of the line indices from each semi-major axis. The results for the ages and metallicities of the Fornax and Virgo galaxies are presented in Figs. 4.3 and 4.4, where the bulge results are represented by circles, the disc results by ellipses, and the lines link bulge and disc results from the same galaxy. The three isolated disc points in Fig. 4.3 are the three galaxies in the Fornax Cluster sample that contain very compact bulges and were thus fitted with an exponential disc model only, as described in Section 3.5. Where the line index measurements lay off the SSP grid, the corresponding stellar populations were estimated by extrapolation, except where the Hβ line index fell below the SSP model, in which case that component was assigned a nominal age of 18 billion years. It is important to note that currently different SSP models give different absolute results due to the remaining uncertainties in stellar astro-
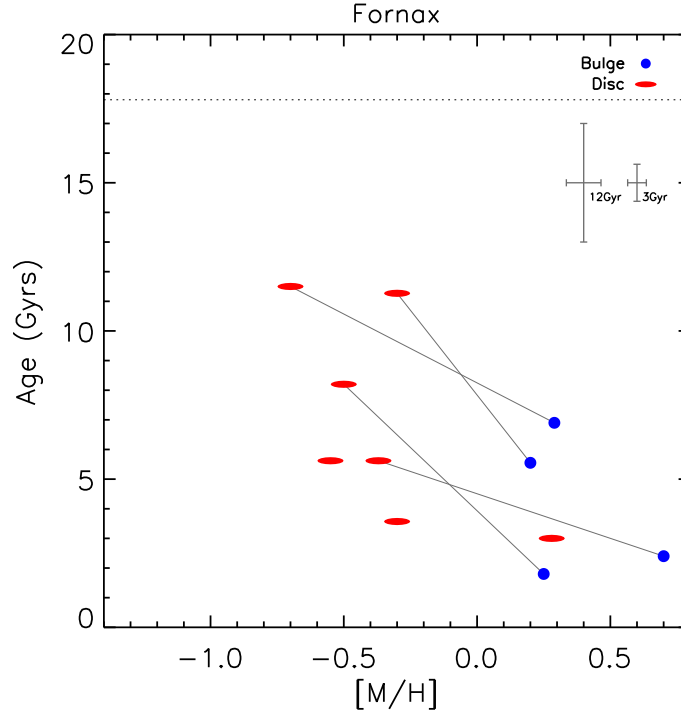
Figure 4.3: Estimates of the relative ages and metallicities of the bulges (circles) and discs (ellipses) of the Fornax Cluster S0s. The solid lines link bulge and disc stellar populations from the same galaxy, and the horizontal dotted line links the lower edge of the SSP models used. The stellar populations measured from the three galaxies modelled as pure discs are also shown. The typical errors for stellar populations of 3 Gyrs and 12 Gyrs are shown on the right of the plot. The larger uncertainy for the 12 Gyr stellar population reflects the increased difficulty of constraining the age of older stellar populations compared to younger ones using the Hβ index.

physics, and therefore the results shown in Figs. 4.3 and 4.4 should be considered as constraints on the relative, global, light-weighted ages and metallicities of the different stellar populations rather than their absolute values. The mean errors for stellar populations of 3 Gyrs and 12 Gyrs are also given, having been derived from a combination of the difference between the stellar populations from both semi-major axes, the statistical uncertainties seen in Fig. 4.2, and interpolation errors when interpreting the SSP models. These two ages were selected as the large differences in their age uncertainies clearly demonstrates the increased difficulty in constraining the age of older stellar populations.

Despite the limitations imposed due to the small number of Fornax Cluster galaxies that could be decomposed into individual bulge and disc components, Figs. 4.3 and 4.4 clearly show that the bulges contain systematically younger and
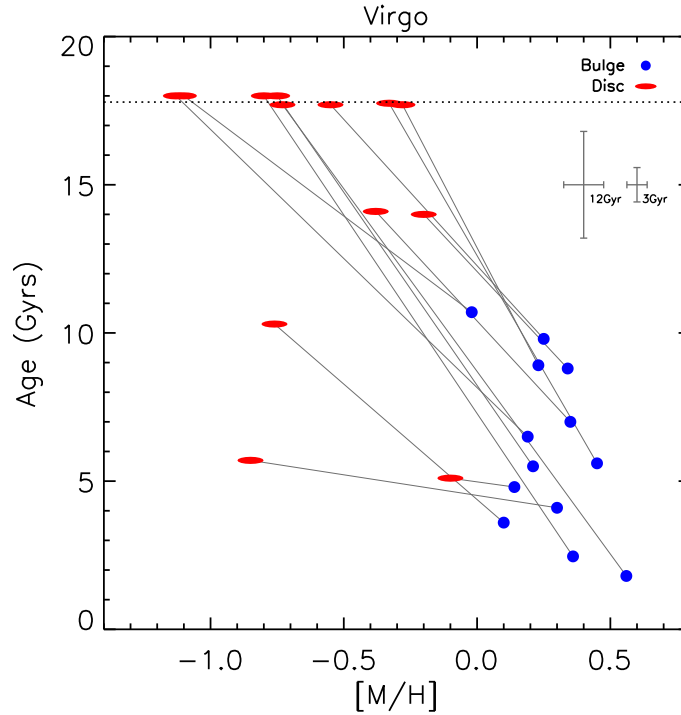
Figure 4.4: Estimates of the relative ages and metallicities of the bulges (circles) and discs (ellipses) of the Virgo Cluster S0s. The solid lines link bulge and disc stellar populations from the same galaxy, and the horizontal dotted line links the lower edge of the SSP models used. The typical errors for stellar populations of 3 Gyrs and 12 Gyrs are shown on the right of the plot. The larger uncertainty for the 12 Gyr stellar population reflects the increased difficulty of constraining the age of older stellar populations compared to younger ones using the Hβ index.

more metal rich stellar populations than their associated discs in both clusters, implying that they hosted more recent formationactivity than the discs. Such recent central star formationactivity after the disc was quenched would explain why S0s have been found to host positive age and negative metallicity gradients throughout their entire structure, while the precursor spirals show old bulges surrounded by a young, star-forming disc (Fisher, Franx & Illingworth, 1996; Bell & de Jong, 2000; Prochaska Chamberlain et al., 2011; Bedregal et al., 2011). It would similarly explain the enhanced luminosity of the bulges of S0s after their transformation from spirals (Christlein & Zabludoff, 2004).

It is interesting to note that the ages of the discs in the Fornax Cluster appear to be younger than those in the Virgo Cluster. This trend may simply be an effect due the smaller sample of galaxies from the Fornax Cluster, but could

also reflect the different evolutionary histories of these two clusters. Virgo is a larger and richer cluster while Fornax is more compact and denser (Abell, Corwin & Olowin, 1989; Girardi et al., 1995; Ferguson, 1989; Jerjen, 2003). Similarly, Virgo clearly shows two substructures within the cluster and displays non-virialized motions (Huchra, 1985; Binggeli, Tammann & Sandage, 1987; Binggeli, Popescu & Tammann, 1993), while Fornax is virialized (Blakeslee et al., 2009). Clearly these two clusters have undergone different evolutionary processes, and so it is unsurprising that this is reflected in the star-formation histories of their galaxies. The differences in ages of the discs could simply represent different gas stripping timescales within the two clusters. Since Virgo is less dense, it is possible that the gas in the spiral discs in this cluster was stripped out over a longer timescale than in the Fornax Cluster. As a result, the disc stellar popualtions in the Virgo galaxies would consist of a composite of stars over a larger age range than Fornax, skewing the global age to older values. Similarly, in the denser environment of the Fornax Cluster, it is possible that the gas stripping mechanism wasn't so gentle, and triggered a small amount of star formation within the disc. The addition of a small amount of younger stars, or 'frosting', to an underlying old stellar population would contribute to a younger overall age (Trager et al., 2000).

4.2 Colour Gradients

As well as estimating the global ages and metallicities of the bulges and discs, this spectral decomposition method also provides an approximate measure of any gradients in these properties within the bulges and discs. Specifically, if there were a colour gradient in a component, such that, say, red light was more centrally concentrated than blue light, then the characteristic size-scale of the component would be smaller in red light than in blue light.

Due to the combination of the residual scattered light retained in the Virgo Cluster data (see Section 2.2.6) and the degeneracy experienced when the fits
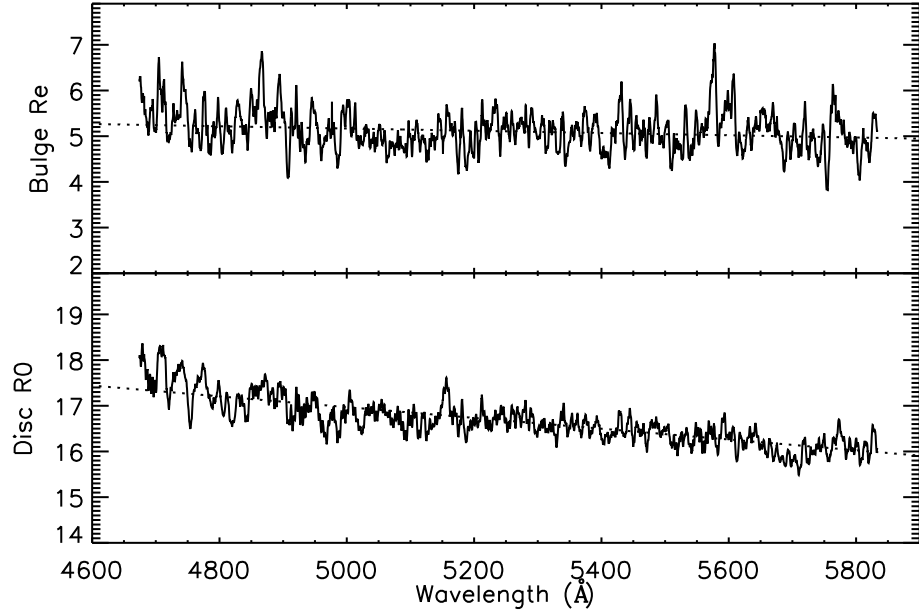
Figure 4.5: Model bulge effective radius and disc scale length plotted against wavelength for NGC1375. A strong negative gradient can be seen in the disc scale-length, corresponding to a negative colour gradient across the disc, while the gradient in the bulge is much weaker.

contained too many free parameters, the decomposition using the Sérsic bulge and exponential disc model was carried out with fixed values for R_e, R_0 and n. However, the pilot study for this technique fitted the Fornax Cluster galaxies with a de Vaucouleurs bulge and an exponential disc, with free parameters for R_e and R_0, thus making it possible to study colour gradients within the decomposed spectra of these galaxies. Two galaxies, NGC 1381 and NGC 1375, were successfully decomposed into bulge and disc components with this model, while a further three galaxies with compact bulges were fitted with exponential profiles to extract their disc spectra. An example of how the scale-lengths of each component vary as a function of wavelength in NGC 1375 are given in Fig. 4.5. Both cases show a clear negative gradient, indicating that the centre of each component is redder than its outer parts, although the effect is clearly stronger in the disc than the bulge.

In order to quantify this effect in terms of more conventional colour gradients, the bulge effective radius and the disc scale length can be calculated at the

the central wavelengths of the B and V band filters from the Johnson-Cousins system [4450 Å and 5510 Å respectively (Bessell, 1990)]. For the bulge, the ratio of light in the B-band to that in the V-band is given by

$$\frac{I_{\mathrm{B}}}{I_{\mathrm{V}}} = \left(\frac{I_{\mathrm{eB}}}{I_{\mathrm{eV}}}\right) \exp\left\{-7.67\left[\left(\frac{1}{R_{\mathrm{eB}}}\right)^{1/4} - \left(\frac{1}{R_{\mathrm{eV}}}\right)^{1/4}\right]R^{1/4}\right\}, \qquad (4.3)$$

or, in magnitudes,

$$B - V = \mathrm{const} - 2.5\log_{10}\left(\frac{I_{\mathrm{eB}}}{I_{\mathrm{eV}}}\right)$$

$$+ 19.18\left(\frac{1}{R_{\mathrm{eB}}^{1/4}} - \frac{1}{R_{\mathrm{eV}}^{1/4}}\right)R^{1/4}\log_{10} e. \qquad (4.4)$$

Differentiating with respect to $R^{1/4}$, we find

$$\frac{d(B-V)}{d(R^{1/4})} = 8.3\left(\frac{1}{R_{\mathrm{eB}}^{1/4}} - \frac{1}{R_{\mathrm{eV}}^{1/4}}\right). \qquad (4.5)$$

This equation can then be integrated out from the centre to any radius, to obtain a change in colour,

$$(B-V)_{\mathrm{R}} - (B-V)_0 = 8.3\left(\frac{1}{R_{\mathrm{eB}}^{1/4}} - \frac{1}{R_{\mathrm{eV}}^{1/4}}\right)R^{1/4}. \qquad (4.6)$$

As a characteristic radius, we set $R = R_{\mathrm{eV}}$ in Equation (4.6), and then divide by $\log R_{\mathrm{eV}}$ to create an appropriate gradient quantity.

A set of analogous equations can be used in order to define a gradient in the disc:

$$\frac{I_{\mathrm{B}}}{I_{\mathrm{V}}} = \left(\frac{I_{0\mathrm{B}}}{I_{0\mathrm{V}}}\right)\exp\left[-\left(\frac{1}{R_{0\mathrm{B}}} - \frac{1}{R_{0\mathrm{V}}}\right)R\right]; \qquad (4.7)$$

$$B - V = \mathrm{const} - 2.5\log_{10}\left(\frac{I_{0\mathrm{B}}}{I_{0\mathrm{V}}}\right)$$

$$+ 2.5\left(\frac{1}{R_{0\mathrm{B}}} - \frac{1}{R_{0\mathrm{V}}}\right)R\log_{10} e; \qquad (4.8)$$

$$\frac{d(B-V)}{d(R)} = 1.09\left(\frac{1}{R_{0\mathrm{B}}} - \frac{1}{R_{0\mathrm{V}}}\right); \qquad (4.9)$$
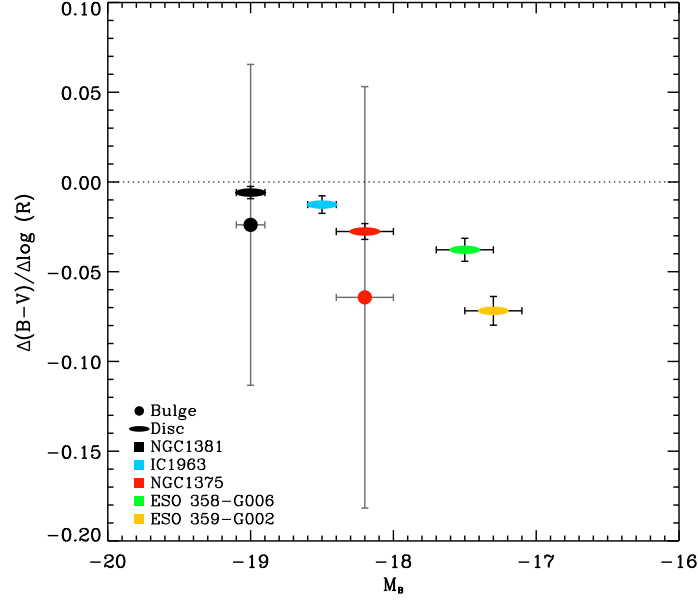
Figure 4.6: The colour gradients in the bulges (circles) and discs (rectangles) of each galaxy against the galaxy's absolute B-band magnitude.

$$(B - V)_{\mathrm{R}} - (B - V)_0 = 1.09 \left(\frac{1}{R_{0\mathrm{B}}} - \frac{1}{R_{0\mathrm{V}}} \right) R. \qquad (4.10)$$

The colour gradients obtained from these formulae using the observed variation in scale-length with wavelength for each component of each galaxy are shown in Fig. 4.6. The uncertainties in these measurements reflect the full range of gradients that could be measured from the scale length plots, such as in Fig. 4.5. The gradients were measured again twice, the first time taking the B-band value as the value from the best fit line plus the 1σ uncertainty due to the scatter, and the V-band value as the value from the best fit line minus the same uncertainty. The second measurement simply reversed where the uncertainties were added and subtracted. The final uncertainties for the gradients plotted in Fig. 4.6 consequenctly reflect the range of gradients obtained through this method.

In all cases, the colour gradients for the discs are negative, indicating that the centres are redder than the outskirts. The multiplication factor of 8.3 for the bulges in Equation 4.6 compared to 1.09 for the discs in Equation 4.10 appears at first to give the bulges steeper gradients. However, the large scatter in the bulge

plots relative to their slope loses all information on whether the bulges contain positive or negative gradients, which is reflected in in the large errors on the bulge points in Fig. 4.6. There also appears to be a trend that the gradients are stronger in fainter galaxies. The range of values obtained are directly comparable to those found in previous studies of early-type galaxies, with La Barbera & de Carvalho (2009) reporting a typical gradient of $\frac{\Delta g - r}{\Delta \log R} \sim -0.071 \pm 0.003$, Roche, Bernardi & Hyde (2010) finding a range of $-0.8 < \frac{\Delta g - r}{\Delta \log R} < 0.0$, and Suh et al. (2010) reporting values of $-0.4 < \frac{\Delta g - r}{\Delta \log R} < 0.0$. den Brok et al. (2011) similarly detected gradients within the range $-0.2 < \frac{\Delta g - i}{\Delta \log R} < 0.0$ for a sample of early-type galaxies, but found that S0s show weaker gradients than ellipticals, suggesting that the underlying mechanisms may differ.

Attempts have also been made to ascertain the causes of such gradients. For example, La Barbera & de Carvalho (2009) concluded that the main contributors to the colour gradients were the radial variations in metallicity over the galaxies, and that, while a small positive age gradient was also present, its contribution to the colour gradient was negligible in comparison. The spectral decomposition method presented here provides us with a new mechanism for seeing directly in the individual components whether these gradients are associated with changes in age or metallicity, and the next section will describe how this information can be exploited.

4.3   Line Index Gradients

If there were a gradient in the strength of a particular absorption line within a single component, the luminosity of the galaxy at that wavelength would drop with radius at a faster or slower rate than the light from other parts of the spectrum. As a result, one would expect that the scale-length as determined within the absorption feature would differ from that of the surrounding continuum, which, in turn, would show up in the two-dimensional spectrum of that component generated from the best-fit model, like those shown in Fig. 3.5. Therefore, these model
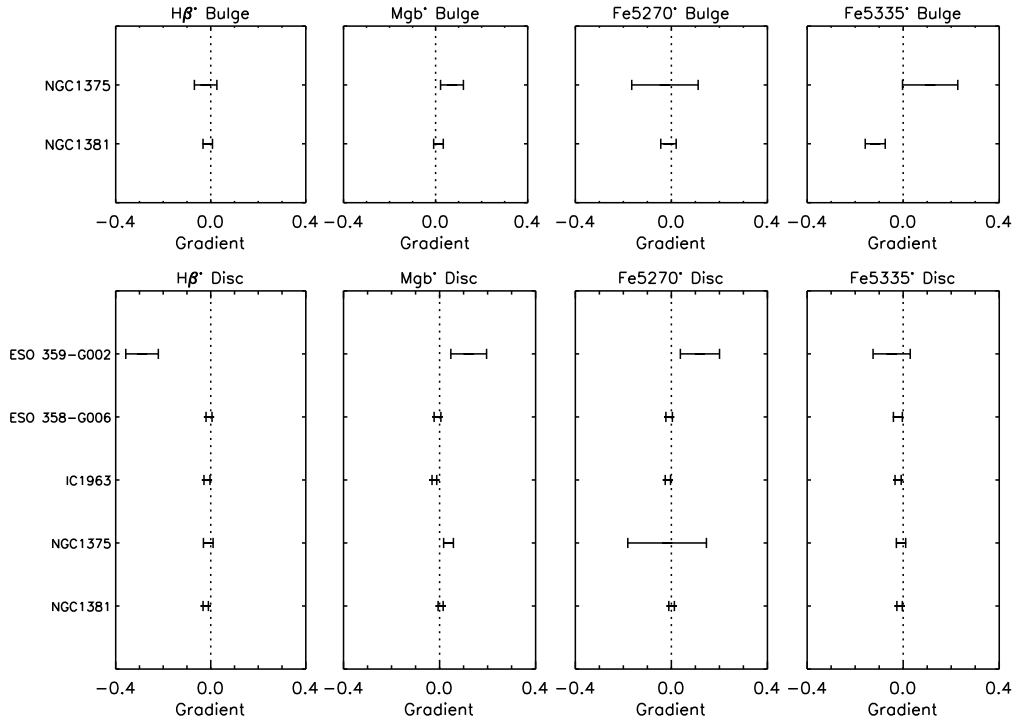
Figure 4.7: The line gradients for the bulge and disc in each galaxy, calculated using $\Delta \text{Index}^*/\Delta \log_{10}(R)$.

spectra were analysed by calculating the Lick indices from them as a function of radius. It is important to note at this point that normally when comparing direct measurements of line indices measured at different radii within a galaxy, the spectra must be broadened to the same resolution. However, since the velocity dispersion was equalised throughout the galaxy before the decomposition process, the decomposed spectra for each galaxy used here should all have the same spectral resolution already, and so no correction is necessary.

Having measured the Lick indices throughout each galaxy, a logarithmic gradient was then generated for each index by calculating the magnitude version of the indices,

$$\text{Index}^* = -2.5 \log_{10} \left(1 - \frac{\text{Index}}{\Delta \lambda} \right), \tag{4.11}$$

and measuring its variation with $\Delta \log_{10}(R)$. The resulting gradients for the bulge and disc of each galaxy are presented in Fig. 4.7.

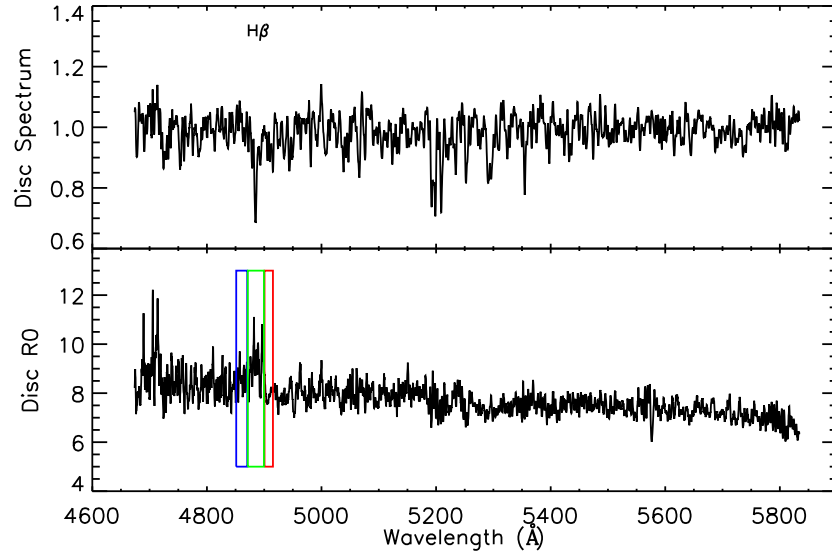Any signal in this plot would arise from a variation in the component's scale-

Figure 4.8: The decomposed disc spectrum for ESO 359-G002 (top) and a plot of its disc scale length against wavelength (bottom). A feature is present at the wavelength of the Hβ line on the scale-length plot, implying that there is a negative gradient in its line strength with radius from the centre of the galaxy. The three bands used for measuring the Lick index strength over this feature have also been plotted, where the colours correspond to those in Fig. 4.1.

length at the wavelength of the index. For example, if a positive absorption line index gradient was present over the disc of a galaxy, the strength of that feature would increase with radius and the light profile would appear steeper at the centre of that feature than in the continuum. As a result, the scale length of the disc at that wavelength would be shorter than in other parts of the spectrum, and so a dip would appear in the scale length plots, such as those in Fig. 4.5. Conversely, a negative gradient in an absorption feature would result in a peak at that wavelength in the scale-length plot. Therefore, the strength of any such features can be used to test the significance of any line index gradients measured over the bulge and disc.

To calculate the errors on the line index gradients shown in Fig. 4.7, the strength of the features present at that wavelength on the corresponding scale length plots were measured by treating those plots as spectra and extracting the Lick indices, as shown in Fig. 4.8 for the Hβ feature: if there were a signal, then the value of scale-length in the central band should differ significantly from
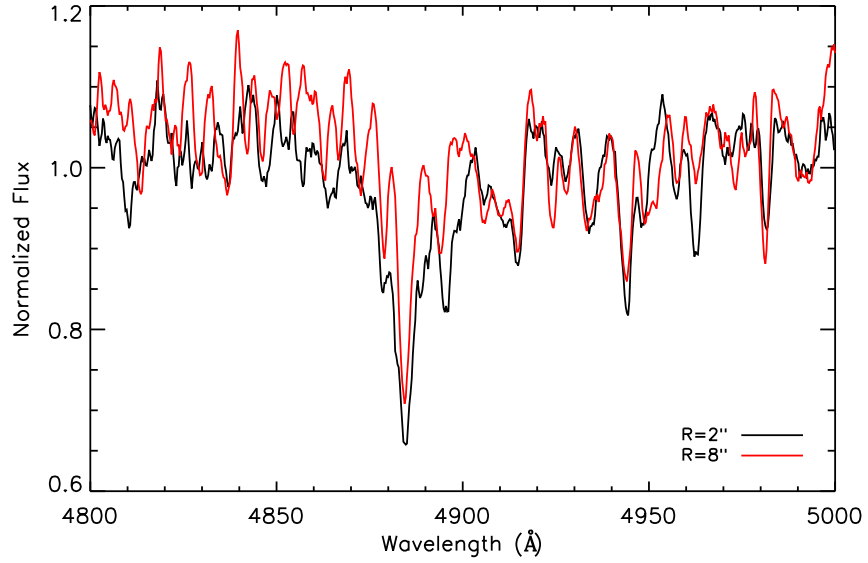
Figure 4.9: The Hβ feature in the reconstructed spectra of the disc of ESO 359-G002 at the radii of the inner seeing limit (black), and the disc scale length (red).

the value in the pseudo-continuum, leading to a non-zero index. To calculate the significance of any such measurement, and hence the appropriate size of the error bars in Fig. 4.7, this procedure was repeated at random wavelengths over the same scale length plot to obtain a measure of the noise over the continuum regions, and the strength of the feature at the true wavelength was divided by this noise. These results were found to be consistent with those of Bedregal et al. (2011), in which the line strength gradients were measured over the whole galaxy.

As can be seen from Fig. 4.7, the Hβ index of ESO 359-G002 shows a negative gradient detected with a $> 4\sigma$ significance, which would suggest the presence of an age variation across its disc. The origins of this detection can be seen in Fig. 4.8, where the scale length measured at the wavelength of Hβ differs from that in the surrounding continuum, just as described above. The effect of this variation on the reconstructed spectra is illustrated in Fig. 4.9, which shows that the derived Hβ feature at a radius of 2 arcsec (the inner seeing limit of the galaxy) is deeper than at 8 arcsec (the disc scale length). The SSP model for this galaxy was used to translate the Hβ line index gradient into an approximate age

gradient of $\Delta \log_{10}(\mathrm{age})/\Delta \log_{10}(R) \sim 1.1 \pm 0.2$. This corresponds to ages of 1.86 ± 0.14 Gyrs and 8.77 ± 0.16 Gyrs at the respective inner and outer radii shown in Fig. 4.9. Note, however, that such an age gradient is in the wrong sense to explain the negative colour gradient seen in this system.

In trying to explain the observed colour gradients, the situation is no more helpful in all the other galaxies. As is evident from Fig. 4.7, none of the other components in any of these systems display significant gradients in any of their indices. These limits can be translated into limits on the variation in the properties of the stellar population between the centre and each component's characteristic radius (R_e for bulges and R_0 for discs) as above. Typically, this analysis yields an upper limit of a $\sim 30\%$ change in age and metallicity between these locations. This corresponds to a colour gradient of $\left| \frac{\Delta(B-V)}{\Delta \log R} \right| \approx 0.02$ using the models of Bruzual & Charlot (2003), which cannot explain the sizeable colour gradients found in Section 4.2. It would therefore appear that some other factor, most likely dust reddening that varies with radius, must be the underlying cause of the colour gradients in these galaxies.

4.4 α-enhancement

A further constraint on the stellar populations of the bulges and discs is provided by the measurement of any enhancement in their α-element abundances relative to iron, as this quantity provides information about the timescales for star formation in the separate components. Nucleosynthesis models predict that a significant proportion of α-elements, such as oxygen and magnesium, present in the ISM are ejected from Type II supernovae (SNe), whereas Type Ia SNe tend to enrich the ISM with Fe (Thomas, Maraston & Bender, 2003). Since Type II SNe start to occur shortly after star formation has begun while Type Ia SNe need longer for their progenitor stars to evolve, the α-element abundance tells us about the timescale over which star formation occurred in a stellar population.

The ratio of the Lick Mgb index to the mean of the Lick Fe5270 and Fe5335

indices, Mgb/$\langle\text{Fe}\rangle$, was selected as a robust proxy of the α-element abundance (Bedregal et al., 2008). Short star-formation events are characterized by larger-values of Mgb/$\langle\text{Fe}\rangle$, with the ratio decreasing for star formation timescales of longer than ~ 1 Gyr due to the increasing Fe enrichment on such timescales.

Due to the small number of Fornax Cluster galaxies that could be successfully decomposed into bulge and disc components, it was decided to analyse the α-enhancement of the Virgo Cluster galaxies only in order to build up statistically representative results for one cluster without the added confusion of results from a second cluster with a potentially different evolutionary history and data systematics.

Since this analysis directly compares measurements of the line indices for all galaxies, the first step was to broaden all the decomposed bulge and disc spectra to match the resolution of VCC 2000, the galaxy with the highest velocity dispersion in this sample. Note that this step is not necessary when studying the stellar populations of each galaxy independently, as in Section 4.1, as the ages and metallicities for each galaxy were obtained directly from SSP models tuned to the resolution of the data. Figure 4.10 presents the Mgb/$\langle\text{Fe}\rangle$ ratio for each decomposed spectrum plotted against the age of the component. It can be seen that the bulge spectra show increasing Mgb/$\langle\text{Fe}\rangle$ ratios with increasing ages; a Spearman rank test on these data shows a correlation coefficient of 0.64, with a less than 2% chance that this correlation could happen by chance. This enhanced Fe enrichment in the younger bulges suggests that the enriched gas that fed the most recent star-formation events in these bulges had been contaminated by exposure to a longer period of star formation than in the older bulges. The disc spectra, on the other hand, show no obvious correlations between their Mgb/$\langle\text{Fe}\rangle$ ratios and their ages. A Spearman rank test carried out on this data resulted in a correlation coefficient of 0.25 and a probability of 50% that such a correlation could be produced randomly. Since many of the discs were found to be old (see Fig. 4.4), their light is not dominated by the latest star-formation event, but instead represents the sum of all the stellar populations within the entire disc, so
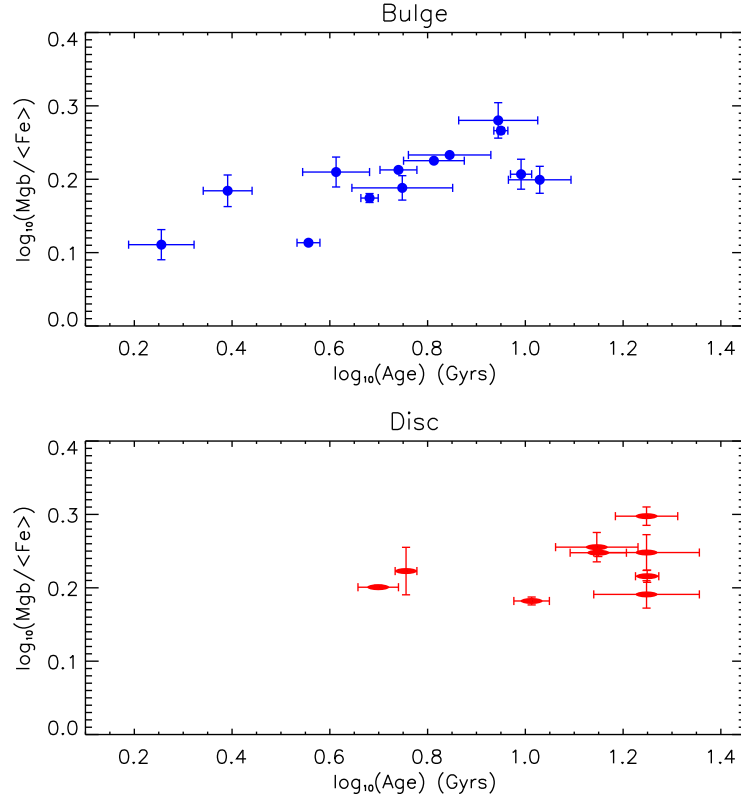
Figure 4.10: The bulge (top) and disc (bottom) Mgb/⟨Fe⟩ ratios plotted against their ages. Note that in the bottom plot, galaxies with disc ages greater than the upper limit of the SSP models have been omitted.

any similar correlation might be expected to be completely washed out.

Interestingly, a comparison of the bulge and disc Mgb/⟨Fe⟩ ratios, shown in Fig. 4.11, does reveal a correlation, with a correlation coefficient of 0.69 and a greater than 99 percent significance. This correlation suggests that the bulge and disc star formation histories are connected, but the offset from the line of equality shows that bulges are in general more Fe enriched than the discs of the same galaxy. This result is consistent with a scenario where the gas that produced the final star-formation event in the bulge was pre-enriched by earlier star formation within the disc. Further evidence for this scenario appears in Fig. 4.12, which clearly links the age of the bulges, and thus the time since the final star formation event there, to the Mgb/⟨Fe⟩ ratios of their surrounding discs, such that galaxies with older bulges had the star formation in their discs truncated longer ago and after a shorter timescale.
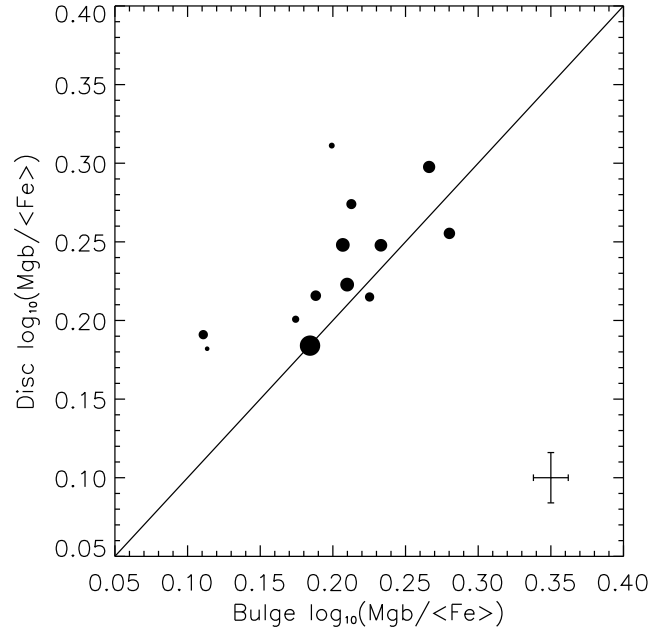
Figure 4.11: The Mgb/$\langle$Fe$\rangle$ ratios for the bulge and disc of each galaxy. The size of the symbol represents the luminosity of the galaxy in the K-band, where larger symbols indicate brighter galaxies. The mean error for the data points is given in the bottom right. The diagonal line represents the line of equality for the bulge and disc measurements for comparison.
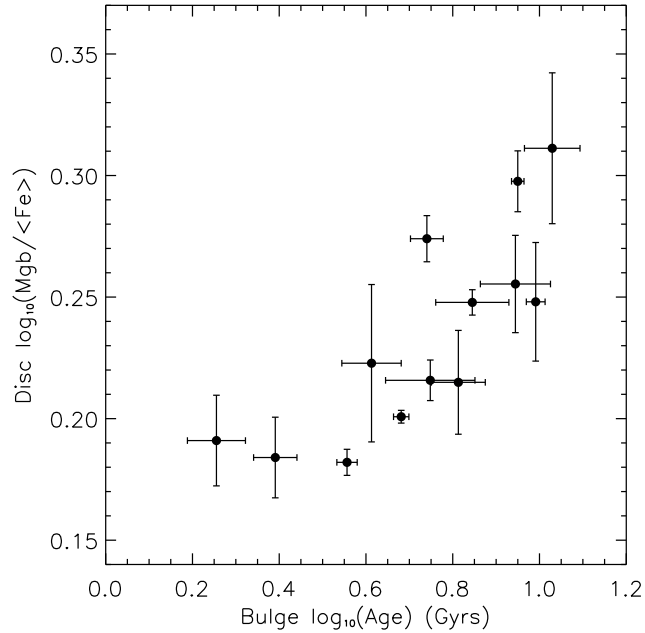

Figure 4.12: The relationship between the disc Mgb/$\langle$Fe$\rangle$ relative abundances and the age of the corresponding bulges, which acts as an indicator of when the final episode of star formation occurred in that galaxy.

4.5   Conclusion

By decomposing Virgo and Fornax Cluster S0 galaxies into clean disc and bulge spectra, we have been able to uncover a number of new facts about these individual components as well as the connections between them. From these data, a coherent quantitative picture of each S0's star-formation history is beginning to emerge, which is summarized in cartoon form in Fig. 4.13. The galaxy starts out as a normal spiral, with an old bulge surrounded by young, star-forming disc. As the spiral galaxy evolves, the star formation rate of the disc typically decreases slowly over time (Hopkins, 2004, 2007; Thomas et al., 2005; Lee et al., 2007), leading to an accumulation of multiple stellar populations within this structure. At some traumatic point in the galaxy's life, the gas in the disc is stripped, thus quenching the star formation there, and in the process some of the gas gets dumped in the centre of the galaxy leading to a final burst of star formation in the bulge. This central star-formation activity after significant quenching of the disc would increase the bulge-to-total light ratio of the galaxy, and hence explain the enhancement of the bulge luminosity during the transformation from spirals to S0s described in Christlein & Zabludoff (2004). The galaxy then fades to the S0 that we see today with a predominantly younger and more metal-rich bulge surrounded by an older and more metal poor disc, as so clearly found in Figs. 4.3 and 4.4. Although strong indications of this phenomenon have been found previously through radial variations in age and metallicity in S0 galaxies by studies such as Bedregal et al. (2011), Fisher, Franx & Illingworth (1996), Bell & de Jong (2000), Kuntschner (2000), MacArthur et al. (2004) and Prochaska Chamberlain et al. (2011), this study confirms that the phenomenon can be traced to the superposition of distinct bulge and disc components rather than more general gradients within those components. Furthermore, the analysis of the Fornax Cluster galaxies found that while negative colour gradients existed within each component, no significant line index gradients were found that could explain the colour gradient in terms of radial variations in the age or metallicity.
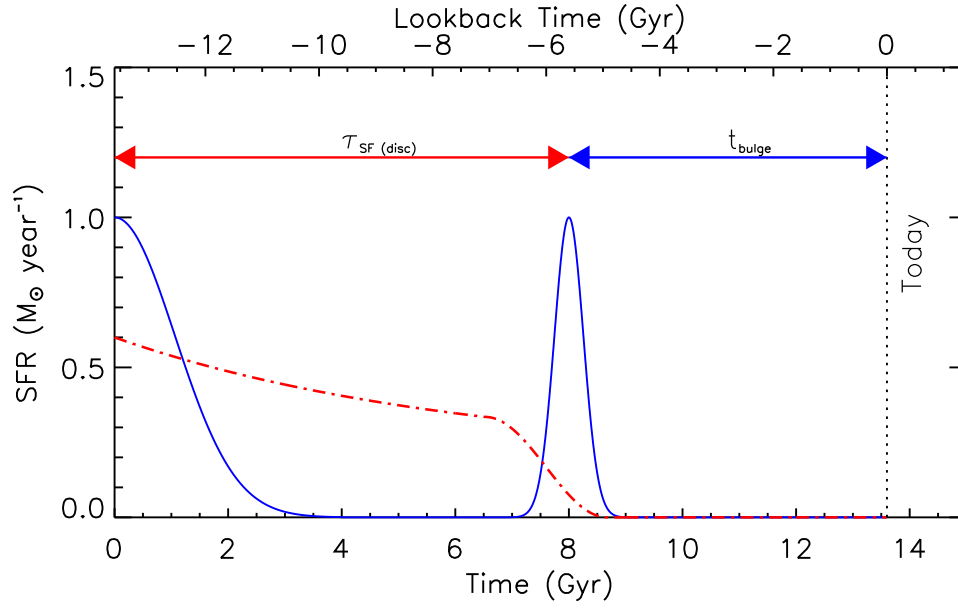
Figure 4.13: A simplified star formation history for the bulge and disc of an S0 galaxy, showing the relationship between the age of the bulge stellar populations, t_{bulge}, and the star formation timescale of the disc, $\tau_{\text{SF(disc)}}$. The disc (dot-dash line) experiences continuous star formation, the rate of which declines gradually with time, until the quenching process begins, which finishes soon after when a central star-formation event uses up the remaining disc gas to produce the predominantly-young bulge of the final S0 (solid line).

It therefore seems likely that the red centres of all components must be attributed to centrally-concentrated dust in these systems.

A subtler probe of the star formation histories of bulges and discs is provided by their α-element abundances. As we saw in Fig. 4.10, there is a significant correlation between Mgb/$\langle$Fe$\rangle$ and age in the bulges of these galaxies, but not in their discs, which can both be understood in the context of Fig. 4.13. The emission from the bulge is dominated by the younger stars from the final burst of star formation, so the value of Mgb/$\langle$Fe$\rangle$ here is largely dictated by the gas from which this burst formed, which in this picture originated in the disc and was dumped into the bulge when the galaxy transformed. Thus, it reflects the properties of the gas in the disc at the end of its star-forming life. In general, the longer ago this transformation occurred (and hence the older the age inferred for the bulge), the shorter the star-forming lifetime of the disc because $\tau_{\text{SF(disc)}} + t_{\text{bulge}}$ in Fig. 4.13 reflect the total age of the galaxy. If $\tau_{\text{SF(disc)}}$ is relatively short (so

t_{bulge} is relatively long), the gas left at the end of the disc's star-forming lifetime will not be so polluted by Fe from type Ia SNe, so Mgb/$\langle$Fe$\rangle$ will be relatively large, explaining the correlation seen. In the disc, on the other hand, the observed value of Mgb/$\langle$Fe$\rangle$ reflects the more extended and potentially complicated complete star-formation history of this component, as its light will not be dominated by a single star-formation event, and the derived luminosity-weighted age will be similarly complex, so the absence of any correlation in this component is not a surprise.

This connection between the polluted gas from the disc and the visible last burst of star formation in the bulge is underlined by Fig, 4.11, which shows the general trend that the Mgb/$\langle$Fe$\rangle$ in the two components are correlated, but that the disc is less Fe-enriched than the bulge. This difference arises because the disc's value for Mgb/$\langle$Fe$\rangle$ reflects its entire star-formation history, some of which will have occurred at early times before the Type Ia SNe started producing large quantities of Fe, whereas the bulge luminosity is dominated by stars produced from the most polluted disc gas, which will be significantly more Fe enriched. There is also an interesting hint in this figure that the most massive galaxies seem to show the least difference between Mgb/$\langle$Fe$\rangle$ for discs and bulges, which would suggest an earlier transformation leading to less difference in the degree of Fe enrichment, as perhaps a new example of the "downsizing" phenomenon.

As a final illustration of the physics that underlies Fig. 4.13, Fig. 4.12 shows the clear correlation between Mgb/$\langle$Fe$\rangle$ for the disc component and the age of the bulge. Again, this fits with the finite time available for galaxy evolution, such that if the transformation occurs later then the disc will have had time to become strongly polluted by Fe, reducing Mgb/$\langle$Fe$\rangle$, and the bulge will have undergone its final burst of star formation relatively recently, decreasing its luminosity-weighted measured age.

The scenario presented in Fig. 4.13 suggests that the age differences between the bulges and discs should only be around a few billion years. While this difference can be seen in the Fornax Cluster S0s in Fig. 4.3, the Virgo Cluster shows

larger age differences for many of the galaxies. Since the age of the disc is related to the time since the galaxy was accreted into the cluster, the older discs in the Virgo Cluster compared to the Fornax Cluster could simply reflect the different evolutionary histories of the two clusters. As discussed in Section 4.1, Fornax is a dense, compact and virialized cluster while Virgo is larger and looser and displays two substructures. As a result, it is likely that galaxies falling into these two clusters would have experienced slightly different gas stripping scenarios. Additionally, the number of galaxies in the sample from each cluster is very different. It can be seen in Figs. 4.3 and 4.4 that some of the Virgo galaxies do show similar age differences between their bulges and discs as those seen in the Fornax Cluster. Consequently, it is possible that there are galaxies in the Fornax Cluster that show similar trends to those in the Virgo Cluster that have simply not been included in this study. However, it is important to remember that the results presented here have been derived from only two galaxy clusters. Therefore, to better understand the transformation scenario between spirals and S0s, we need to study a larger sample of galaxies from a wider range of clusters.

As this discussion indicates, there is now a wealth of information that can be gleaned by decomposing spectra of S0 galaxies into their bulge and disc contributions, and studying the detailed stellar population properties of these individual components. We are at the point of being able not only to put together the general picture of the quenching of disc star formation accompanied by a final episode of bulge star formation shown in Fig. 4.13, but also looking at the variations from galaxy to galaxy to tie down the different histories that different galaxies have witnessed.

Chapter 5

Disentangling the Stellar Populations of NGC 4550

5.1 Introduction

The presence of counter-rotating populations of stars in S0 galaxies is a well-known phenomenon, although reasonably uncommon: while almost a quarter of S0 galaxies contain gaseous components that counter-rotate relative to their stars, less than 10% were found to contain distinct counter-rotating stellar disc components (Bertola, Buson & Zeilinger, 1992; Kuijken, Fisher & Merrifield, 1996; Emsellem et al., 2011). However, such systems do exist, and so any theory of S0 formation must provide a channel for their creation.

Of these counter-rotating systems, the one that presents the greatest challenge to models of galaxy formation is VCC 1619, or NGC 4550 as it is better known. Rubin, Graham & Kenney (1992) obtained long-slit spectra along the major axis of this normal-looking S0 galaxy (see Fig. 2.1), and found that the absorption-lines split neatly into two, indicating two extended counter-rotating discs. Subsequent analysis has confirmed that these discs are very similar, with comparable sizes, masses, kinematics and line strengths (Rix et al., 1992). Integral-field observations, in combination with dynamical models, confirmed the picture, but

revealed some breaking of the symmetry, with one disc being thicker than the other (Cappellari et al., 2007) and also containing an emission-line component (Sarzi et al., 2006).

The reason that it is difficult to come up with a scenario for constructing such a system is that the obvious solution of merging two normal discs with opposite angular momenta does not generally work. In particular, it has long been known that most mergers between two roughly equally-massive discs are likely to be very destructive, heating the system enormously and not resulting in the required disc-like final morphology (Toomre, 1977a). However, this problem may not be insurmountable: Puerari & Pfenniger (2001) show that a major merger between disc galaxies of comparable mass could produce the kinematics seen in NGC 4550, as long as the initial conditions are just right, with the precursor systems co-planar on a carefully-chosen parabolic orbit. A similar result was found by Crocker et al. (2009), who also tried to reproduce the gas kinematics of the galaxy. Clearly, such an arrangement is rather contrived, but not impossible if systems like NGC 4550 are truly rare. The ATLAS^{3D} survey (Cappellari et al., 2011) obtained integral field stellar kinematics for a volume-limited sample of 260 early-type galaxies. Out of these they found 11 cases (see fig. C5 of Krajnović et al. 2011) showing evidence for major counter-rotating stellar discs. However in only about half of these (about 2% of the sample) do the two counter-rotating discs seem to have comparable mass, as in NGC 4550.

An alternative scenario that avoids the destructive force of a major merger is the possibility that counter-rotating gas could be accreted rather slowly by a normal disc galaxy, and subsequently form stars in a new counter-rotating disc. This possibility was explored through simulations by Thakar & Ryden (1996, 1998), who found that the counter-rotating stellar disc formed in this way tended to be rather small. They did find that a series of mergers with gas-rich dwarf galaxies could produce a counter-rotating disc of comparable mass and size to the original, but once again the initial conditions needed to be very carefully tuned to produce such matched discs.

The similarity of the two discs in NGC 4550 led Evans & Collett (1994) to suggest a third possibility that could much more naturally produce identical counter-rotating discs. In this "separatrix-crossing" scenario, a single initially-triaxial elliptical galaxy evolves slowly with time into an axisymmetric morphology. At that point, the family of box orbits that existed in the triaxial system would disappear, and stars would switch onto tube orbits instead. Since the initial box orbit had no preferred sense of rotation, stars would end up randomly on tube orbits rotating in either sense around the centre of the now-axisymmetric system, thus automatically generating a pair of identical counter-rotating stellar populations.

To date, it has not been clear which, if any, of these scenarios might be responsible for the formation of NGC 4550. However, they do predict some distinct differences in the resulting counter-rotating discs, particularly in the properties of their stellar populations, which we might be able to use to distinguish between them. While the separatrix-crossing scenario will produce truly identical discs, a counter-rotating stellar disc formed by gas accretion must have a younger population than the pre-existing disc, while the counter-rotating discs in a system formed by a merger will reflect the stellar populations of the progenitor galaxies. In this chapter, I will present a novel technique using the different kinematics of the two discs to separate their stellar populations, and thus determine whether this bizarre galaxy formed through internal processes or through interactions with another galaxy.

5.2   Kinematic Decomposition

In order to study the stellar populations of the two component counter-rotating discs, the first step is to separate their spectra. Fortunately, outside the central few arcseconds, the line-of-sight velocities of the two components are different enough to split the corresponding absorption lines quite cleanly (see Fig. 5.1 for an example of the characteristic cross-shaped profile for the absorption features)
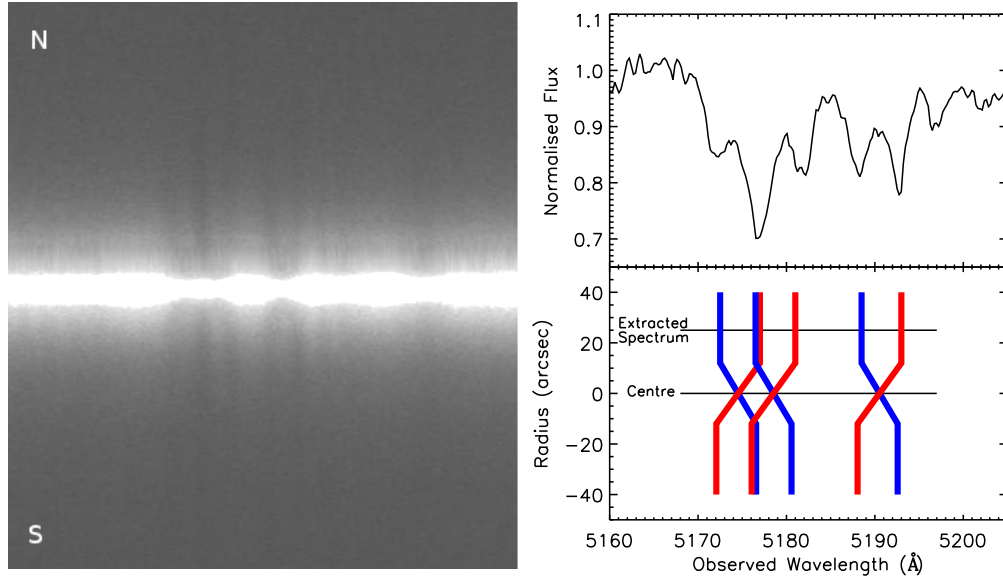
Figure 5.1: A section of the two-dimensional spectrum of NGC 4550, centred on the Mg triplet (left), and a closer look at the effect on the shape of the spectral features due to the counter-rotating discs, taken from the outer parts of the disc where the kinematics are well separated (right).

– indeed, it was this splitting that enabled Rubin, Graham & Kenney (1992) to identify the counter-rotating discs in the first place. Therefore, we can fit a two-component spectral model to the spectra in this region, where each component has a different mean velocity and velocity dispersion, reasonably unambiguously. At the same time, we also have to allow for the unknown stellar population properties of the two components. In order to fit all these factors simultaneously, the PPXF code was modified in a similar way to Coccato et al. (2011), such that instead of combining a series of template stars to produce a single model spectrum to fit the galaxy, it derives two model spectra representing the two stellar population components, which, when added together, would best fit the galaxy spectrum. To achieve the best fit, the component spectra were multiplied by low-order Legendre polynomials to model out any mismatch in the flux calibration of the continuum, and convolved with line-of-sight velocity distributions of different shapes, mean velocities and dispersions, to best represent the kinematics of each component.

One further complication that is clear from the raw spectra is that there is a

third, gaseous, component rotating in one direction, as is evident from the strong [OIII]$_{\lambda 5007}$ emission line. We can deal with this contaminant by simply masking it from the spectral range used in the fitting. However, there is presumably also emission from hydrogen gas, which usually accompanies the [OIII]$_{\lambda 5007}$ line in galaxies. Such emission could prove disastrous for the analysis of this galaxy as it would partially fill in the hydrogen absorption lines of one of the stellar components, completely altering the derived line strengths of these important lines, and thus the inferred properties of the stellar population. The idea of kinematic decomposition of the stellar populations is not yet lost completely, as it was also found that the observations for this galaxy, unlike some others in the sample (see Section 2.2), were minimally affected by contamination from scattered light. As a result, a wider spectral range of $4250 < \lambda < 5400$ Å could be used for the spectral fitting, which encompasses the wavelength of the Hγ absorption feature. Therefore, a third component was fitted, consisting simply of two Gaussians representing emission lines at the wavelengths of the Hβ and Hγ features, with a FWHM equal to the spectral resolution of the galaxy spectrum and the ratio of their intensities given by the Balmer decrement from Reynolds et al. (1997). By convolving this component with its own velocity distribution in the fit process, one can also obtain the kinematics of the gas component. Fortunately, due to the long wavelength range over which the spectra are fit, and because the ratio of hydrogen emission line strengths in the gaseous component is different from the ratio of the corresponding absorption lines in the underlying stellar component, there is no degeneracy in the resulting fit, so both components can be independently extracted. In principle, differential reddening could introduce a degeneracy problem, but because this galaxy is an S0 with little evidence for large amounts of dust, the effect is not thought to be significant.

A typical result of this fitting process is illustrated in Figure 5.2. As well as confirming the generally very good job that this fitting process does in reproducing the full spectrum with the three components, this figure also underlines the importance of including the gas component: from the raw spectrum, one might
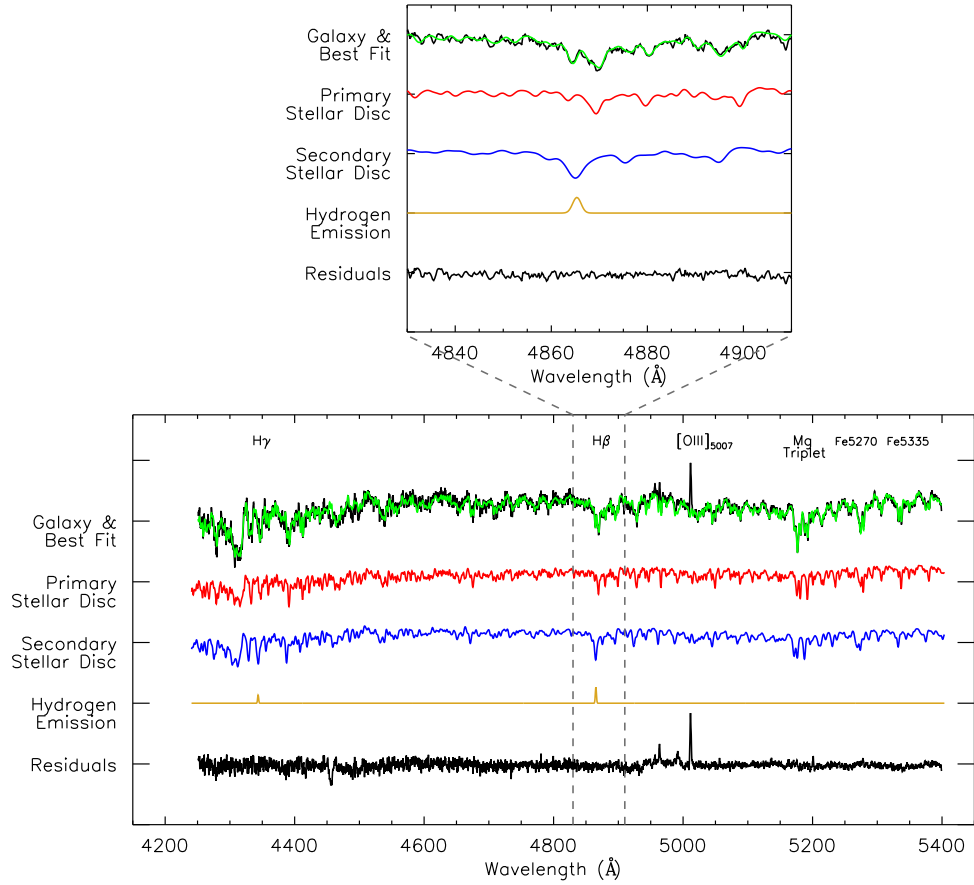
Figure 5.2: The spectrum of one side of the outer disc of NGC 4550, showing both the full spectral range and a zoom in on the Hβ line. The data are shown in black, and the green line shows the best-fit model. The individual components that comprise this model and the residuals of the fit are also shown.

conclude that the Hβ absorption line is somewhat stronger in the redshifted (primary disc) component, but the full fitting process reveals that this conclusion is driven by the filling in of the absorption feature in the blueshifted component by the emission line, and actually it is this secondary-disc component that has the stronger absorption line.

This fitting process was repeated using the spectral data from all along the major axis, co-added spatially to maintain a signal-to-noise ratio of at least 20 per pixel as described in Section 3.1. Only the central ~ 5 arcsec could not be decomposed in this way, due to a combination of the overlapping kinematics of the two discs and the increasing contribution to the light from the bulge. The mean velocities and velocity dispersions derived for the three components over
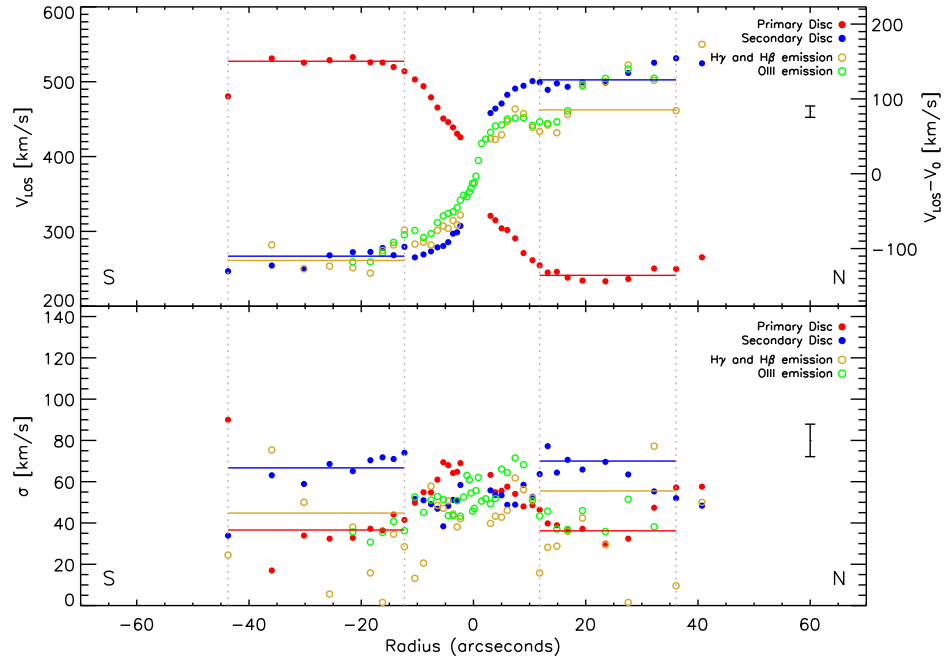
Figure 5.3: Measurements of the radial velocity and velocity dispersion for each kinematic component fitted to the spectra of NGC 4550 as a function of radial position along the major axis (with north and south directions annotated). Typical characteristic error bars are shown on the right of each plot. The horizontal lines show the results of fitting to spectra co-added over the entire flat part of the rotation curve (marked by vertical dotted lines). The kinematics of the $[OIII]_{\lambda 5007}$ line, derived by direct fitting to the spectral line, are also shown.

the galaxy are shown in Fig. 5.3. Errors on each point were estimated by Monte Carlo simulations of model galaxies constructed using the same components as in the fit; for clarity, we do not plot all points with error bars, but show the mean resulting error on the right of the plot. We also tested the sensitivity of the kinematic results to the spectral templates adopted by repeating the analysis using a sub-sample of the ELODIE spectral templates (Prugniel & Soubiran, 2001) that covered the full range of spectral classes with a spectral resolution of 0.5 Å (FWHM), but found no significant systematic differences.

By co-adding the data from the flat part of the rotation curve, as marked in Fig. 5.3, we found a primary disc with a rotation velocity of 143 ± 7 km s^{-1} and a velocity dispersion of 36 ± 7 km s^{-1}, and a secondary disc with a lower rotation velocity of -118 ± 8 km s^{-1} and a higher velocity dispersion of 68 ± 10 km s^{-1}. These results are consistent with the early findings of Rix et al.

(1992). Additionally, subsequent to this study, Coccato et al. (2013) decomposed the kinematics of NGC 4550 in a similar way using full two-dimensional IFU data. Their results show excellent agreement with those presented in Fig. 5.3. They found that the primary disc rotates with a velocity of $\sim 140 \, \mathrm{km \, s^{-1}}$ outside of 25" with a velocity dispersion of between $60 - 80 \, \mathrm{km \, s^{-1}}$ in the inner regions which drops to $\sim 30 \, \mathrm{km \, s^{-1}}$ at a radius of 14". Similarly, they measured the velocity of the secondary stellar disc to be slower than the primary disc, with a value of $\sim 110 \, \mathrm{km \, s^{-1}}$, and with a velocity dispersion of $40 - 80 \, \mathrm{km \, s^{-1}}$. The ionized gas was also found to corotate with the secondary disc with the same velocity, and with a velocity dispersion of $\sim 50 \, \mathrm{km \, s^{-1}}$.

There is clearly something a little strange about the kinematics derived for the emission-line gas disc. Because the gas shows a lower velocity dispersion than the secondary stellar disc that co-rotates with it, one would expect it to display a smaller amount of asymmetric drift, and hence rotate more quickly, whereas it actually rotates slower than the accompanying stars. This strange property does not seem to be the result of any failing in extracting the gas kinematics correctly: we can obtain some confidence that the fitting process is picking up the correct properties for the hydrogen emission lines by comparing the results obtained to those measured directly from the excluded [OIII]$_{\lambda 5007}$ line, also shown in Figure 5.3, which are clearly very similar. The most likely explanation is therefore that the gas does not form a simple equilibrium axisymmetric disc, and hence would not obey the usual asymmetric drift equation. Indeed, some indication of an asymmetry in the [OIII] gas velocity with respect to the projected major axis is visible in Sarzi et al. (2006).

Since the spectra of the two discs in this galaxy were disentangled by full spectral fitting over a wide wavelength range from galaxy spectra that had been spatially binned to build up the S/N to a minimum of 20, the resultant best fit for each disc should contain reliable representations of the star formation histories contained within that component. Therefore, a careful analysis of the stellar populations should determine how this galaxy, and thus others like it, formed.

5.3   Stellar Populations

Having kinematically decomposed the spectra into the two stellar disc components at each radius, we can now study the stellar populations of each individual component, as derived from the strengths of its absorption lines. In order to render the line strengths at different radii comparable, all component spectra were broadened with Gaussians to match their dispersions to the largest values found at the centre of the galaxy. Estimates for the ages and metallicities of each disc as a function of radius were then derived using the SSP models of Vazdekis et al. (2010), as described in Section 4.1.

Figure 5.4 shows the resulting values of the $H\beta$ index in the stellar discs, as an indicator of stellar population age, plotted against the combined metallicity index, $[MgFe]'$, as an indicator of metallicity, for each component as a function of radius. The average results obtained by combining all the outer disc data from the flat part of the rotation curve, as delineated in Figure 5.3, is also shown. Since this galaxy was centred on the CCD, we have observations covering the whole of both sides of the galaxy. As a result, the counter-rotating components will be Doppler shifted in opposite directions on opposite sides, which allows for two independent measurements of these quantities with potentially different systematic biases as different spectral features in the two components will end up superimposed in the composite spectra from each side. An illustration of this effect is the Mg-triplet presented in Fig. 5.1, in which the simplified diagram clearly shows the distortion in the spectral features due to the superposition of light from the two discs. Although not so clear in this diagram, the different line-of-sight velocities of the two discs would result in different distortions on both sides of the galaxy, even in the outer regions where the kinematics have flattened out. The good agreement between the two rows of plots shown in Fig. 5.4 again provides some confidence that the results are not significantly compromised by this effect.

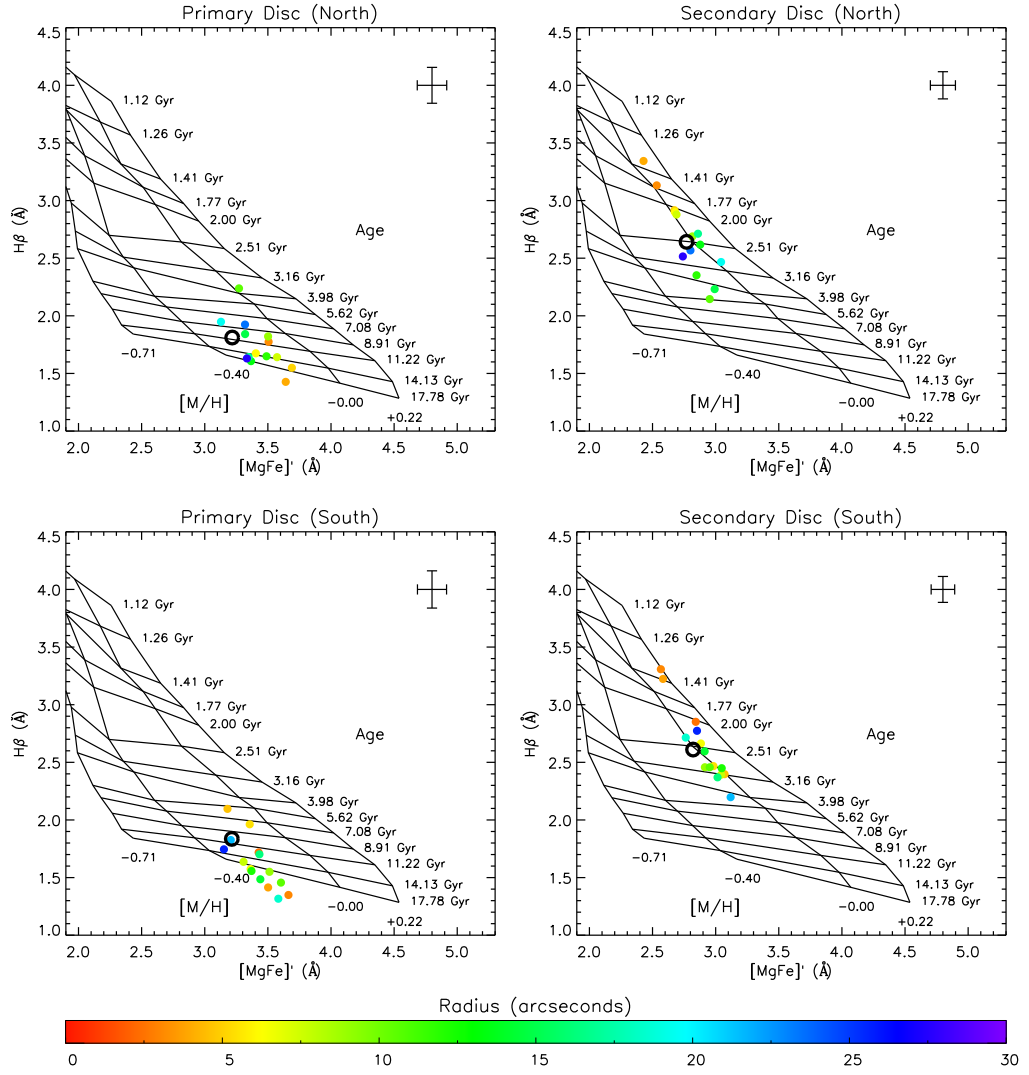What is most striking about these plots is the systematic difference between

Figure 5.4: The line indices derived from the model components compared to the predictions of SSP models, measured out to a radius of ~ 30 arcsec, or ~ 2.25 kpc, where the S/N drops below 30 per Angstrom. The primary and secondary discs are in the left and right columns, while the north and south side of the galaxy are in the upper and lower rows. The radius of each measurement is color-coded; the open black points show the average value for the outer part of each disc. For clarity, points are plotted without errors; a typical error bar is shown in the top right of each plot.

the Hβ indices between the two components: the primary disc is old, with an age inferred here of $\sim 11\,\mathrm{Gyr}$, while the secondary disc is much younger at $\sim 2.5\,\mathrm{Gyr}$, with its innermost parts even more youthful. Interestingly, the young component was also found to co-rotate with the molecular gas (Crocker et al., 2009) and the ionized gas, which are generally associated with recent star formation episodes. Similar trends were also found in the subsequent analysis of Coccato et al. (2013), such that the primary disc was found to be older than the secondary disc.

5.4 The Demise of the Separatrix-Crossing Model

By carefully disentangling the spectral components of NGC 4550, we have been able to learn a great deal about their individual properties, determining quantities that have significant implications for how this peculiar system might have formed. In particular, the strong differences in the stellar populations of the two discs seem to rule out the separatrix-crossing model in which they were formed from a single parent stellar population. It is interesting that one of the things that motivated Evans & Collett (1994) to consider this model in the first place was the apparent similarity of line strengths between components; as we have now seen, this similarity in apparent Hβ line strengths arises from an unfortunate cancellation between the stronger absorption lines of a younger population superimposed on the emission lines from the gas that rotates in the same direction.

However, the very presence of this gas suggests that all may not be lost for the separatrix-crossing model. Perhaps this scenario did indeed occur, creating two initially-identical stellar discs. Subsequent accretion then created a gas disc rotating in the direction of one of the stellar discs, and this gas then formed further generations of stars, creating a composite population in the disc co-rotating with the gas whose mean age would appear younger, as observed. Indeed, one could always invoke sufficient recent star formation to shift the inferred age from ~ 11 Gyr to ~ 2.5 Gyr. Since the line-index ages are effectively luminosity-weighted,

a relatively modest amount of star formation, creating a bright young population, might explain the observed age differential. An example of such a scenario was presented for NGC 628 by Sánchez-Blázquez et al. (2014), in which they studied the total integrated light of the galaxy to determine the mass- and luminosity-weighted fractions that were created thoughout the lifetime of the galaxy. They found that the galaxy contains an underlying old stellar population created between 8 and 17 Gyrs ago which contributes towards 95% of the total mass of the galaxy. The younger stellar population has an age of about 1 Gyr, as calculated from the MILES stellar population models, and dominates the total luminosity fo the galaxy despite consisting of only 5% of the total mass of the galaxy.

Fortunately, we have one further constraint from this analysis that we can use to assess the viability of this modified scenario. Specifically, the decomposition of the spectra into the two stellar discs also tells us how much total light should be attributed to each component. Clearly, if one of the two initially-identical discs has had significant new stars forming in it, this component will have a greater luminosity. Encouragingly, this is what we find: the decomposition of the whole outer disc spectra (the open symbols in Figure 5.4) reveals that the secondary component, which co-rotates with the gas, has a continuum level at 4400 Å (the centre of the B-band) that is 20% higher than the gas-free primary component.

So now we have an extra constraint which means that the amount of late star formation we can add is fixed by this additional 20% of B-band luminosity. We do not know the exact star formation history of any such late addition, but we can try out different possibilities. In order to narrow down the range of different and complicated star formation histories that could produce the observations outlined above, two extreme scenarios were tested – a single starburst at $\sim 11\,\mathrm{Gyr}$ followed by either continuous star formation to the present day, or a second starburst in more recent times. These star-formation histories are illustrated schematically in Fig. 5.5.

To obtain stellar spectra for such star-formation histories, the requisite com-
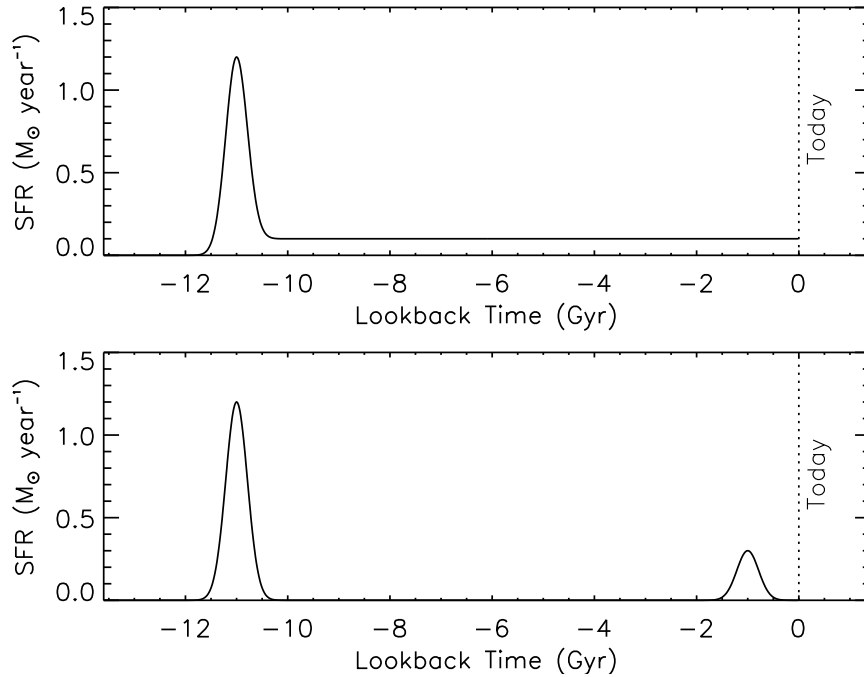
Figure 5.5: Illustrations of possible star-formation histories that could explain the observed stellar populations in terms of the separatrix-crossing model. Assuming both discs formed at the same time, ~ 11 Gyr ago, the younger stellar populations detected in the secondary disc could have been created through continuous, low-level star formation since the initial starburst (top), or through a single, more recent starburst (bottom).

posite stellar spectra were constructed from the MILES stellar library.[1] The spectra were weighted according to the mass fractions created in the initial starburst and in the later star-formation events: typically the mass fraction of the initial starburst was $\sim 0.85 - 0.99$ of the total mass created through the example star-formation histories. The luminosity of the resulting spectrum in the B-band was then compared to that of a stellar population with an age of 11 Gyr and a metallicity of -0.25, which represents the stellar population of the primary disc, to identify which simulated spectrum resulted in a secondary disc 20% brighter than the primary disc. In order to build up a better picture of how these different scenarios would affect the underlying stellar populations from the original disc, this procedure was repeated with a range of metallicities and, in the case of the second starburst scenario, ages for the later star formation.

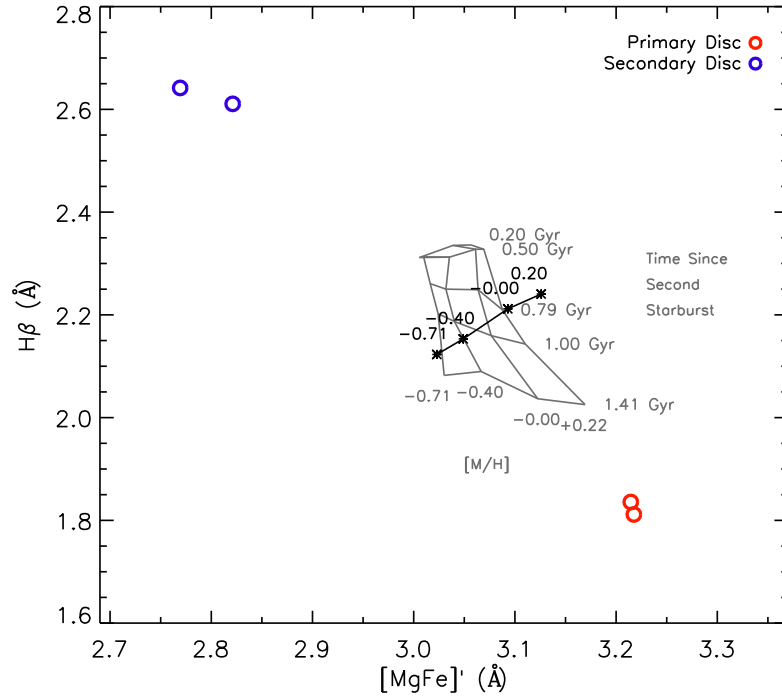Having identified the spectra created for each set of parameters that give the

---

[1] http://miles.iac.es/

Figure 5.6: Model line indices derived for different star formation histories following separatrix crossing. The black line shows the effect on the line indices of the primary disc if the initial population had continuous steady star formation of differing metallicities until the present day, while the grey grid shows the effect of a single burst of star formation at the times and metallicities indicated. The open circles are the results for the two sides of the primary and secondary discs from Fig. 5.4.

correct increase in luminosity, the line strengths were measured and compared to the measurements from the primary and secondary discs, as shown in Fig. 5.6. The points at the bottom right show the line indices measured for the primary disc, which form the presumed starting point of the stellar population of both discs at the moment of separatrix crossing. The points at the top left show the higher indices that we are trying to reach by adding subsequent star formation. The line of crosses show what happens if we invoke continuous steady star formation of different metallicities ever since the old stellar population formed: the level of this star formation is then uniquely fixed by the requirement that its addition results in an enhancement of the disc's total B-band luminosity by 20%. Similarly, the grid of points shows the change in line indices caused by the addition of a single burst of star formation of varying ages and metallicities, again

with the amplitude of the burst tuned to match the enhanced total luminosity of the disc. Since these two extreme possibilities of star formation history move the disc to the same region of the plot, it is not surprising that other more complicated possibilities also all end up in the same area. Clearly, although this additional later star formation moves the line indices in the right direction, it is nowhere near sufficient to reproduce the observed values for the younger disc.

5.5   Discussion and Conclusions

With regret, we are forced to abandon the elegance of the separatrix-crossing model entirely, and conclude that NGC 4550 formed through one of the other scenarios. The ages inferred in Section 5.3 then tell us something about the process. If formed through a carefully-controlled merger of fully-formed galaxies, these ages just reflect the ages of the progenitors. In the gas-rich accretion scenario, which now seems more natural, the ~ 2.5 Gyr age of the secondary disc tells us how long ago this gas was accreted, with the residue of this accreted gaseous material still rotating along with this component, albeit in a somewhat non-circular manner. The higher velocity dispersion of this younger disc then presumably reflects the more turbulent nature of such secondary gas accretion when compared to the more conventional formation of the older primary stellar disc. We even begin to obtain some insight into the spatial distribution of this star formation, with the age gradient in the secondary component implying that the star formation has become ever more centrally concentrated as the gas has been depleted. If this scenario is correct, the only unexplained phenomenon is why the two counter-rotating disc components have such similar spatial extents, which at this point we must simply attribute to coincidence.

Chapter 6

Conclusions and Future Work

Our understanding of the evolution of galaxy morphology and the significance of the Hubble Sequence has grown greatly over the last 30 years. For example, there is now considerable evidence that S0s tend to be found more frequently in higher density environments and towards lower redshifts, while spirals show the opposite trend. As a result, S0s are often thought of as quenched spirals, in which the star formation has been suppressed, the spiral arms have faded, and the luminosity of the bulge has been built up relative to the disc. Although the exact quenching process is still unclear, it is likely to be triggered by interactions with neighbouring galaxies or the intracluster medium in which the galaxy's gas is either used up in a final star formation event, or stripped out altogether. The stellar populations of the bulges and discs hold the answers to their individual star-formation histories, and thus the processes that created the galaxy. Therefore, to better understand the transformation, this thesis outlines two novel techniques to spectroscopically decompose a galaxy into its different components, and their application to a sample of 30 S0 galaxies from the Virgo and Fornax Clusters to study their individual stellar populations, and thus the sequence of events that led to the quenching of star formation and the formation of S0 galaxies.

6.1   Conclusions

6.1.1   Decomposition of Bulge and Disc Spectra

In Chapter 3, we presented a new technique to apply bulge–disc decomposition to long-slit spectra. The idea behind the decomposition is fairly similar to the traditional radial decomposition of light profiles obtained from photometric data. After correcting for the line-of-sight velocity distribution of the galaxy, the light profile at each finely-separated wavelength is decomposed by finding the best fit from a bulge-plus-disc model, and the individual bulge and disc spectra are created by integrating the decomposition parameters at each wavelength. The resulting high-quality spectra allow the study of the stellar populations contained within each component independently with minimal cross-contamination.

The technique has proven successful, with over half of the total sample being reliably decomposed into their bulge and disc components. As described in Chapter 3, the remaining galaxies could not be decomposed due to the presence of emission features in their central regions, additional components or structures within the galaxy that complicated their light profiles, and insufficient signal-to-noise ratios for a reliable fit. It is worth remembering at this point that the sample of galaxies used in this study consists of all the S0s in the Virgo and Fornax Clusters with inclinations of ≥ 40 degrees and brighter than $M_B = -17.3$. Therefore, since it is a representative sample of cluster S0s, no selection bias was applied by only observing those galaxies with obvious two-component structures, and so it is only to be expected that the decomposition will be unsuccessful for galaxies with more complicated morphologies. In fact, with such a sample, we have been able to ascertain that this technique works best for galaxies that are well described by a simple bulge-plus-disc model, where both components are sufficiently resolved to allow for a reliable structural fit, and where there is little indication of complicating issues, such as strong dust lanes or bars.

The technique has also been shown to be robust against modest uncertainties

in the decomposition parameters, and to retain information on the stellar populations within the bulge and disc after the kinematics corrections. Therefore, the decomposed spectra do provide a reliable representation of the luminosity-weighted stellar populations within each component, and the analysis of such spectra should help determine how the star formation in the progenitor spirals was quenched.

6.1.2 The Quenching of Star Formation in Spirals

Chapter 4 outlines the analysis of the decomposed bulge and disc spectra, in which the most prominent result is that the bulges contain systematically younger and more metal-rich stellar populations than the discs. This result contrasts with the traditional view of the progenitor spiral galaxies, in which the bulge is often considered to be old and dead while the disc hosts ongoing star formation that lights up the spiral arms. Therefore, we must deduce that at some point during the quenching process, a final star-formation event must have occurred in the bulge region while the disc is already beginning to grow old and fade.

Earlier indications of such central star formation prior to the transformation from spiral to S0 have been found through radial studies of the stellar populations within similar galaxies. For example, positive age and negative metallicity gradients along the major axes of S0s have been detected by Fisher, Franx & Illingworth (1996), Bell & de Jong (2000), Kuntschner (2000), MacArthur et al. (2004), Bedregal et al. (2011) and Prochaska Chamberlain et al. (2011). However, these studies cannot ascertain whether these gradients represent a smooth gradient over the galaxy, or whether they simply arise through the superposition of different amounts of bulge and disc light at each radius, where each component contains different stellar populations. Therefore, the strength of the spectroscopic bulge–disc decomposition method presented in this thesis becomes clear because we can now see for the first time that the bulges and discs of S0s in clusters do contain very different stellar populations. The smooth gradient sce-

nario is further eliminated in the Fornax Cluster galaxies by the lack of line index gradients detected within their bulges and discs, which suggests that any colour gradients observed are simply the result of dust reddening.

The further analysis of the bulge and disc spectra have strengthened these results by showing that both components also experienced very different star formation histories. The lack of correlation between the α-enrichment of the discs and their ages suggests that they underwent continuous star formation at a slowly declining rate during the lifetime of the progenitor spiral galaxy. As a result, the light from the disc we see today is not dominated by a single stellar population, instead consisting of multiple older stellar populations with different ages. Furthermore, the often large differences between the bulge and disc ages suggest that the quenching process must have been fairly gentle, such that it removed the gas from the disc without causing sufficient disruption to trigger significant new star formation in that part of the galaxy, even after it had commenced in the bulge. Such a scenario would also explain the enhancement of the bulge luminosity and apparent fading of the disc during the transformation, as was found photometrically by Christlein & Zabludoff (2004).

The bulges on the other hand do show a strong correlation between their ages and α-enrichments, such that the more recent star formation in younger bulges was fuelled by gas that was more polluted with iron. Since the progenitor spirals contained old, red-and-dead bulges, this correlation suggests that during the quenching scenario, the bulges accreted gas from somewhere until a final star-formation event there used it up and quenched the galaxy. The most likely origin of this accreted gas is the surrounding disc, which is backed up by the clear correlation between the bulge and disc Mgb/$\langle$Fe$\rangle$ ratios in Fig. 4.11, implying that the bulge knows about the chemical history of the surrounding disc. Furthermore, the offset from equality in this correlation further emphasises the different star-formation histories of the two components. The bulges show a higher Fe-enrichment than the surrounding discs as their light is dominated by the younger stellar population created in the most recent star-formation event. On the other

hand, the lower Fe-enrichment of the discs represents that of the multiple older stellar populations that built up during the continuous star formation activity over the lifetime of the progenitor spiral.

Together, these results have helped build up a clear picture of the quenching process that transforms spirals into S0s. The progenitor spiral consists of an old bulge surrounded by a young disc that is undergoing star formation at a slowly declining rate. At some point in the life of the spiral, an interaction with a neighbouring galaxy or the intracluster medium strips the disc of its gas, thus quenching the star formation in the spiral arms. Given the lack of significant star formation induced in the disc during the quenching, it is likely that the mechanism was a gentler process, such as ram-pressure stripping or starvation. Such gentle processes acting on the galaxy are also apparent from the discy morphologies of S0s, showing that the stellar orbits were minimally disrupted as the gas was stripped out. Similar conclusions have also been reached for the quenching processes in cluster environments by Maltby et al. (2012) and Jaffé et al. (2011). However, during the quenching, some gas from the disc is driven into the central regions of the galaxy, where it triggers a final star-formation event in the bulge that terminates the quenching process. The galaxy then fades to an S0 with a young, metal-rich bulge and an enhanced bulge-to-total light ratio.

6.1.3 Decomposition of Counter-Rotating Discs

Any theory for galaxy evolution must be able to explain the origins of the more unusual galaxies we observe in order to be considered complete. One such galaxy is NGC 4550 in the Virgo Cluster, which has two counter-rotating stellar discs of similar mass and size, and a gaseous disc, all orbiting in the same plane. The three most commonly proposed theories for the formation of this galaxy are:

- the merging of two galaxies under exactly perfect conditions to produce such a system without disrupting the circular motions of either stellar disc (Crocker et al., 2009; Puerari & Pfenniger, 2001)

- the accretion of gas into a counter-rotating disc followed by star formation that produces the second stellar disc (Thakar & Ryden, 1996, 1998)

- the natural collapse of the stellar orbits into the two discs through the separatrix-crossing model of Evans & Collett (1994).

To determine which of these scenarios best explain the origin of this unusual galaxy, Chapter 5 describes a decomposition method utilising the very different kinematics of the two discs, and the subsequent analysis of their separate stellar populations.

The stellar populations of the two discs were found to be of very different ages, where the primary disc appears to be ~ 11 Gyr old with no significant age gradient, while the secondary disc shows a mean age of ~ 2.5 Gyr with the central regions being even younger. Although such a large difference in age appears to favour the merger and gas accretion scenarios outlined above, it may still be explicable if the discs were initially formed at the same time and then only one experienced later star formation activity. Therefore, to test this theory, predictions of line indices were obtained for two extreme star-formation histories – both starting with a disc created in an initial star-formation event ~ 11 Gyr ago, with one scenario assuming continuous star formation since then, and the other assuming a single starburst more recently. In these tests, the mass fraction created in the more recent star-formation activity was restricted by the observed 20% difference in luminosity between the two discs. However, the resulting differences in the line index predictions for both scenarios were insufficient to explain the age difference detected between the two discs. Therefore, we can rule out the elegant separatrix-crossing process to explain the formation of NGC 4550, and conclude that this galaxy formed through either the accretion of gas or of another galaxy.

Interestingly, this result contrasts with the gentler gas stripping scenario that appears to trigger the formation of simple bulge-plus-disc systems in the Virgo and Fornax Clusters. Therefore, it is apparent that S0s are produced through a va-

riety of mechanisms that leave different signatures in the structure of the galaxy. These findings again emphasise the strength of such decomposition techniques in determining the star-formation histories of galaxies of different morphologies.

6.2 Future Work

The work described in this thesis has outlined two different techniques to decompose a galaxy into its individual components using its light profile and its kinematics. The natural progression for this work is to further develop these techniques in order to apply them to different galaxies with more complicated morphologies.

6.2.1 Two-Dimensional Spectroscopic Bulge–Disc Decomposition

The next natural step for the spectroscopic bulge–disc decomposition technique outlined in Chapter 3 is to remove the limitations on the complexity of the models that can be used. One way to reduce such limitations would be to increase the information we have about the spatial structure of the galaxy using wide-field integral field unit (IFU) spectroscopic data. Since IFU datacubes of a galaxy effectively produce images of that galaxy at each individual wavelength, it is possible to apply bulge–disc decomposition to each of these images with software such as GALFIT (Peng et al., 2002, 2010) or GALFITM, which was created by the MEG-AMORPH team (Measurement of Galaxy Morphology, Häußler et al., 2013; Vika et al., 2013). An initial test of such a decomposition is presented in Fig. 6.1. As with the long-slit spectroscopic decomposition, this technique will provide information on the proportion of the light that originates from the bulge and disc at each wavelength and how their parameters vary with wavelength. However, the added strength of decomposing IFU spectra is that it provides structural information from over the whole galaxy, thus allowing for more complicated models
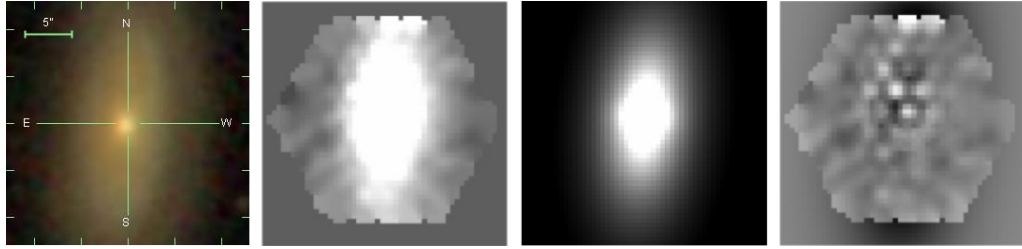
Figure 6.1: Example of bulge–disc decomposition being applied to an image of cgcg 073-090 at ~ 4919 Å from the MaNGA test data sample. From left to right are the SDSS image (DR7) of the galaxy for comparison, the original image from the MaNGA data cube, the best fit model using a sersic plus exponential profile, and the residual image after subtracting the model from the original.

to be utilized in the fits.

Development of this technique is still in the early stages, but it has already produced some promising results as a proof-of-concept, which can be seen in Fig. 6.2. The galaxy decomposed here is cgcg 073-090, and was observed as part of the initial test data for the Mapping Nearby Galaxies at APO (MaNGA, Bundy et al, Submitted to ApJ) survey.[1] The galaxy itself is classified as a red edge-on disc galaxy with no obvious spiral arms at a redshift of $z \sim 0.02$, which is small enough that the majority of the galaxy can be detected within the MaNGA field of view (22.5×22.5 arcsec; see Fig. 6.1), while being large enough that its bulge and disc structure can be seen. After correcting for the kinematics in a similar way to that described in Section 3.1, images of the galaxy over the selected wavelength range were decomposed simultaneously with the GALFITM software to obtain bulge and disc parameters at each wavelength. GALFITM uses an adapted version of GALFIT to perform automated bulge–disc decomposition on multi-waveband images while constraining variations in the free parameters to physically meaningful values. The constrained parameters included the position angle, ellipticity, bulge effective radius, bulge Sérsic index and disc scale length, where the values for these quantities were obtained from decomposing a stacked image from the IFU spectrum over the same wavelength range. The main advantage of this software over GALFIT alone is that by simultaneously

---

[1] http://www.sdss3.org/future/manga.php
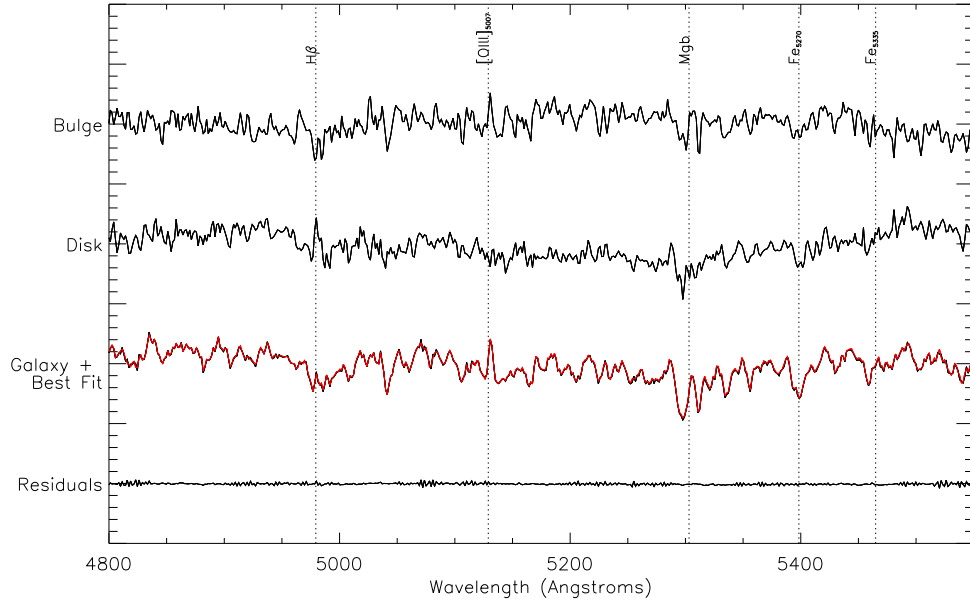
Figure 6.2: Examples of the decomposed bulge and disc spectra for cgcg 073-090 (first and second from the top respectively), using a sersic profile with Sérsic index of 2.94 for the bulge and an exponential profile for the disc. The third row gives the original integrated spectrum of the galaxy in black with the integrated bulge + disc + PSF spectrum from the best fit at each wavelength overplotted in red, and the residuals at the bottom for comparison. The vertical dotted lines mark the redshifted wavelengths of significant spectral features within this wavelength range.

decomposing multiple images at different wavelengths and constraining certain parameters, the overall signal can be improved for the individual fits, leading to more reliable and consistent results over the full wavelength range, which is especially useful for IFU images which have lower S/N per image than photometric data. The resultant bulge and disc spectra are shown in Fig. 6.2, along with the original integrated spectrum and the residuals for comparison.

This adaption of the spectroscopic bulge–disc decomposition technique described in Chapter 3 appears promising, and with the added structural information, it should prove possible to decompose galaxies with more complicated morphologies than has already been achieved. With the many wide-field IFU surveys, such as MaNGA and CALIFA (Sánchez et al., 2012), and instruments, like MUSE on the VLT (Bacon et al., 2006), now becoming available, we are entering an exciting time to probe the internal star formation histories of galax-

ies with the spectral decomposition techniques outlined here. Furthermore, with the much larger wavelength ranges offered by such data, particularly from the MaNGA survey, the stellar populations can be analysed using full spectral fitting techniques to obtain more robust estimates of ages and metallicities than can be achieved with the Lick indices alone.

6.2.2 Decomposition of the Bulge and Disc Kinematics

Another interesting step would be to combine the luminosity and kinematic decomposition techniques outlined in Chapters 3 and 5 in order to obtain information on the individual kinematics of the bulge and disc. Such information could shed further light on the role of mergers in galaxy formation. For example, if a galaxy experienced any mergers in its past, the interaction would lead to a disruption of the stellar orbits within the disc, leaving it less rotationally supported than if the star formation was simply quenched through gas stripping. Therefore, by separating the kinematics of the bulge and disc, we can better study the line-of-sight velocity distribution of the disc and look for evidence of minor mergers without any contamination from the hotter bulge kinematics.

By decomposing the light of a galaxy, either from a long-slit or IFU spectrum, two one-dimensional spectra representing the bulge and disc stellar populations can be derived. These spectra can be fitted with stellar template spectra using the PPXF software to obtain the combination of templates that best fits each spectrum, along with their relative weightings. By combining these template spectra with the correct weights, template bulge and disc spectra can be created at the resolution of the stellar library, thus removing the effects of broadening of the spectral features due to the kinematic corrections applied to the original galaxy spectrum.

Using these templates, the spatially-binned galaxy spectra can be decomposed using the modified PPXF code from Chapter 5 to fit the bulge and disc templates with independent line-of-sight velocity distributions. To further im-

prove the reliability of the decomposition, the relative weights of the bulge and disc template spectra can be restricted to lie within reasonable limits using the bulge-to-disc light ratio at that location, as predicted from the previous decomposition, as a guide. As a result, the combination of these two techniques should provide both stellar populations and kinematics information independently for the bulge and disc for the first time, allowing us to determine the significance of mergers in the transformation of spirals to S0s. In addition, such ideas are not restricted to S0 galaxies, but can equally be applied to galaxies with more complex morphologies and containing more components. For example, it would be possible to isolate the spectrum of a bar in this way using its own distinct kinematics.

6.2.3   The Effects of Environment of Galaxy Evolution

The analysis presented in this thesis has focussed entirely on the formation of S0 galaxies in local cluster environments with simple bulge-plus-disc morphologies. To build up a more representative understanding of the transformation of spirals into S0s, we really need to consider galaxies in different environments and with more complicated structures. The techniques described throughout this thesis can easily be extended to such a broad sample, thus allowing a direct comparison between the star-formation histories of a broad range of S0s to truly understand their evolution. To build up an initial sample of galaxies for such a study, a proposal has been submitted for time to observe a sample of 10 S0s in isolated and cluster environments with MUSE, the new wide-field IFU spectrograph on the VLT. The selected galaxies lie at a mean redshift of $z \sim 0.03$ to maximise the 1 arcmin by 1 arcmin field of view of MUSE, and will allow us to compare quenching mechanisms in different environments.

There is still much work to be done, but this thesis represents the first steps in spectroscopically decomposing the different components within galaxies to understand their individual star-formation histories, and thus the sequence of events

that created these galaxies. The near future should therefore prove interesting in terms of building up a full and complete understanding of the evolution of galaxy morphology through such decomposition techniques.

Appendices

Appendix A

Kinematics Plots

This appendix gives plots for the major-axis kinematics for 19 of the 21 Virgo Cluster Galaxies. VCC 1619 (NGC 4550) has been omitted as the separated kinematics of the two counter-rotating components are given in Fig. 5.3, and VCC 1833 is not included as the spectrum had insufficient signal-to-noise to obtain any reliable spatial kinematics information. In each case, the line-of-sight velocity (V_{LOS}), velocity dispersion (σ), and the shape parameters, h_3 and h_4, are plotted as functions of radius. The centre of each galaxy, as defined by the peak in the spectral luminosity, is marked by the vertical dashed line.

For comparison, kinematics from the SAURON (Emsellem et al., 2004) and ATLAS$^{\mathrm{3D}}$ (Cappellari et al., 2011) surveys have been overplotted in red for all the galaxies that overlapped with these surveys – only VCC 2092 and VCC 698 are excluded. Since these literature results are derived from IFU data, the radius of each binned spectrum was taken as the distance from the centre of the galaxy. Positive and negative radii were then assigned using the kinematic position angles for each galaxy from Krajnović et al. (2011) to identify which side of the galaxy the binned spectrum was located. Both surveys used the Sauron instrument on the WHT in La Palma, which has a field of view of 33 × 41 arcsec, and so comparisons with the long-slit kinematics can only be carried out over the inner regions of these galaxies.

In general, the long-slit kinematics agree with the IFU kinematics from the literature. Since the IFU kinematics are derived from binned spectra over the two-dimensional structure of the galaxy, those results show a larger scatter than the long-slit kinematics due to the wider range in velocities measured above and below the plane of the disc. Consequently, it is reassuring to see that the long-slit kinematics tend to follow the higher-velocity edge of the scatter in the line-of-sight velocity plots and the lower edge of the scatter in the velocity dispersion plots, as would be expected for data from along the major-axis of each galaxy.
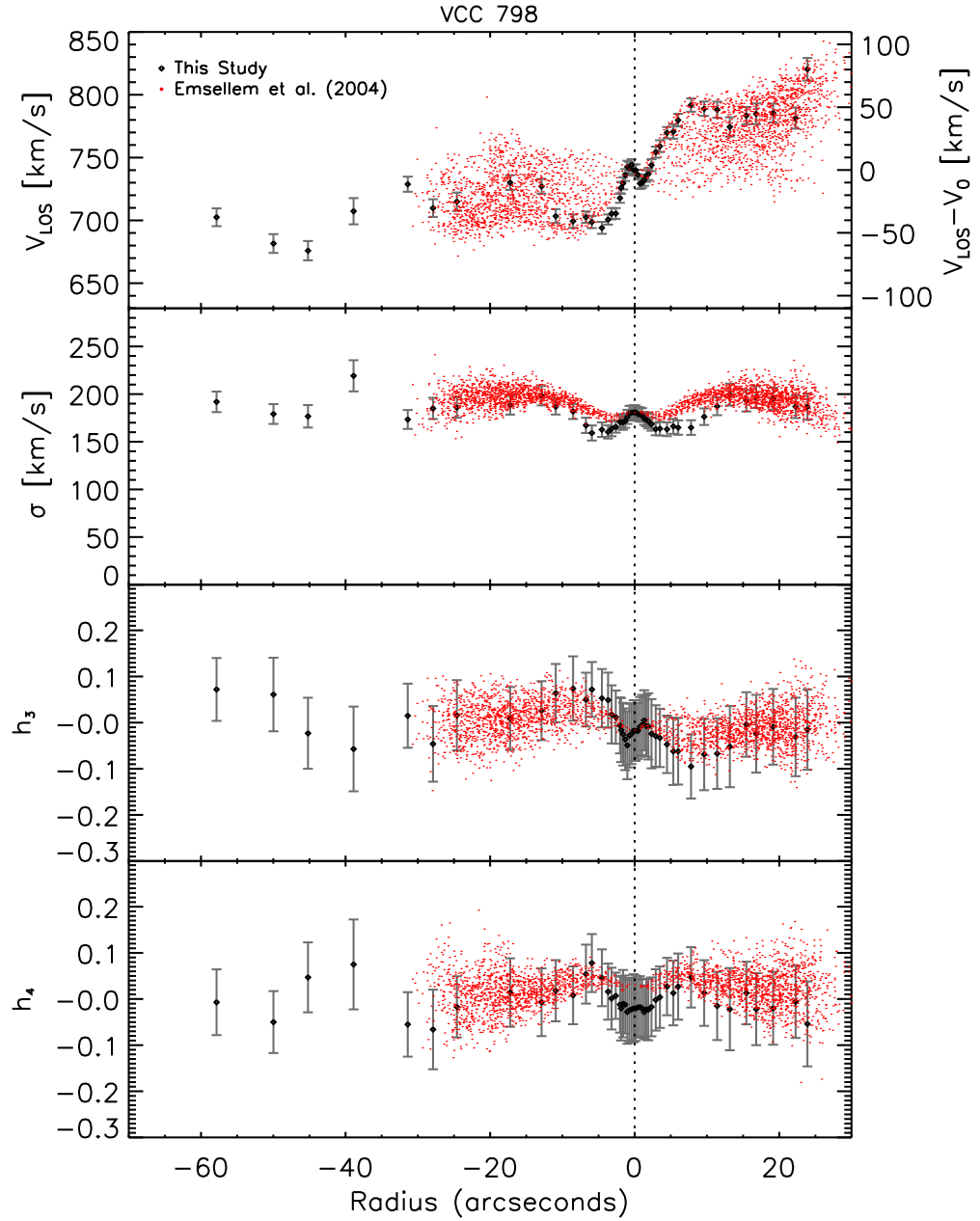
Figure A.1: The kinematics along the major-axis of VCC 798.

The line-of-sight velocity appears to abruptly change direction at radii of $\sim$ ± 1 arcsec, which may indicate the presence of a nuclear counter-rotating component, such as a kinematically-decoupled core (Franx, Illingworth & Heckman, 1989; Emsellem et al., 2004). Since the decomposition was carried out on the light profiles from a radius of 2.5 arcsec, it is unlikely that the presence of such a component would have affected the fits, and so the galaxy was successfully decomposed into bulge and disc spectra.
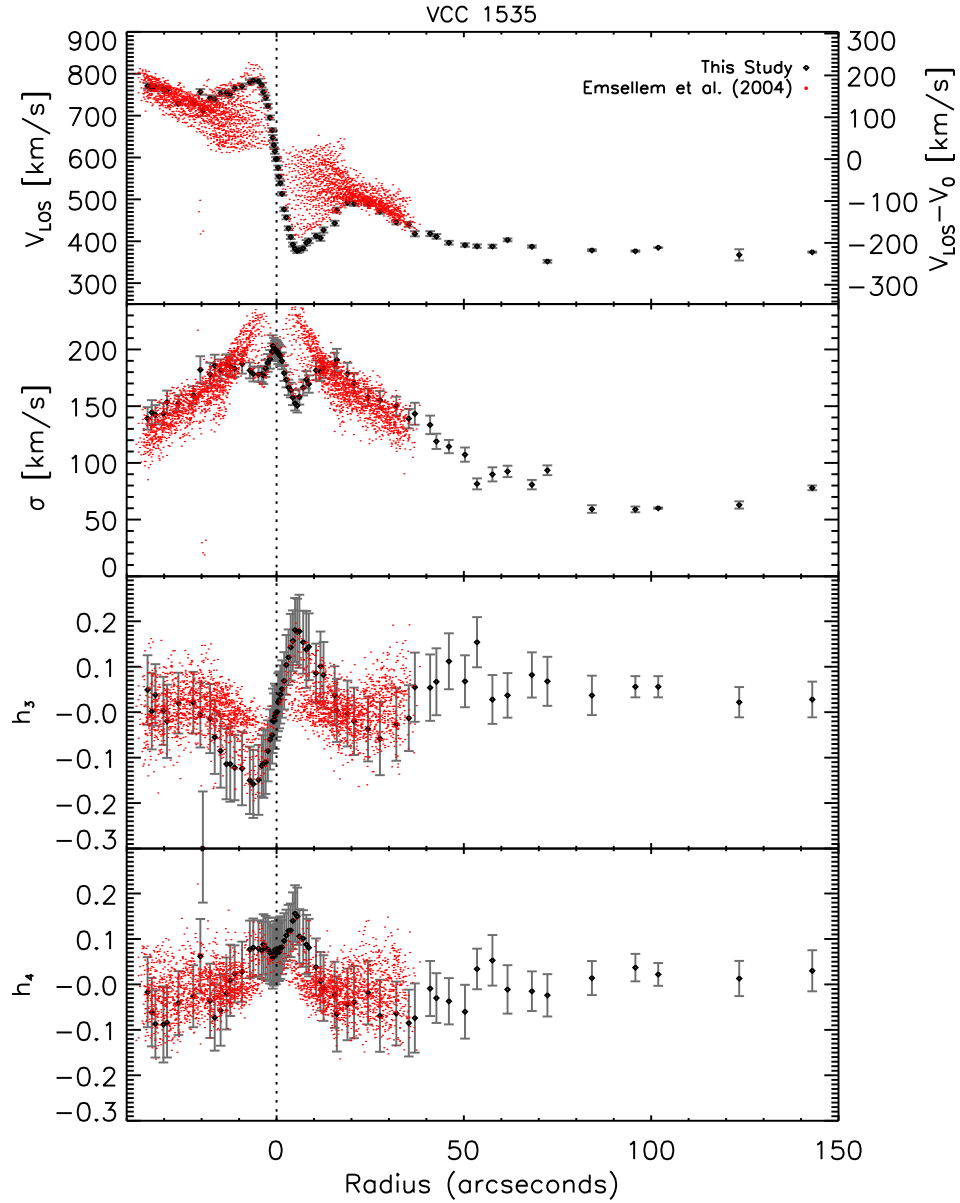
Figure A.2: The kinematics along the major-axis of VCC 1535.

The line-of-sight velocity of this galaxy gives an indication of the presence of a strong bar viewed edge-on, which is further reflected in the h_3 signature (Bureau & Athanassoula, 2005). This galaxy is listed as barred in Third Reference Catalogue of Bright Galaxies (hereafter RC3, de Vaucouleurs et al., 1991), but as an unbarred S0 in Côté et al. (2004). It was also found by Emsellem et al. (2004) and Ferrarese et al. (2006) to contain a dust disc extending to 15.6 arcsec either side of the centre of the galaxy, and the spectra showed strong Hβ and [OIII] emission in the inner parts of the galaxy. As a result, the light profile of this galaxy in Fig. B.4 clearly shows some disruption at the edge of the dust disc, and a subtle bulging at smaller radii, and as a result could not be fitted with the simple bulge-plus-disc model used in this study.
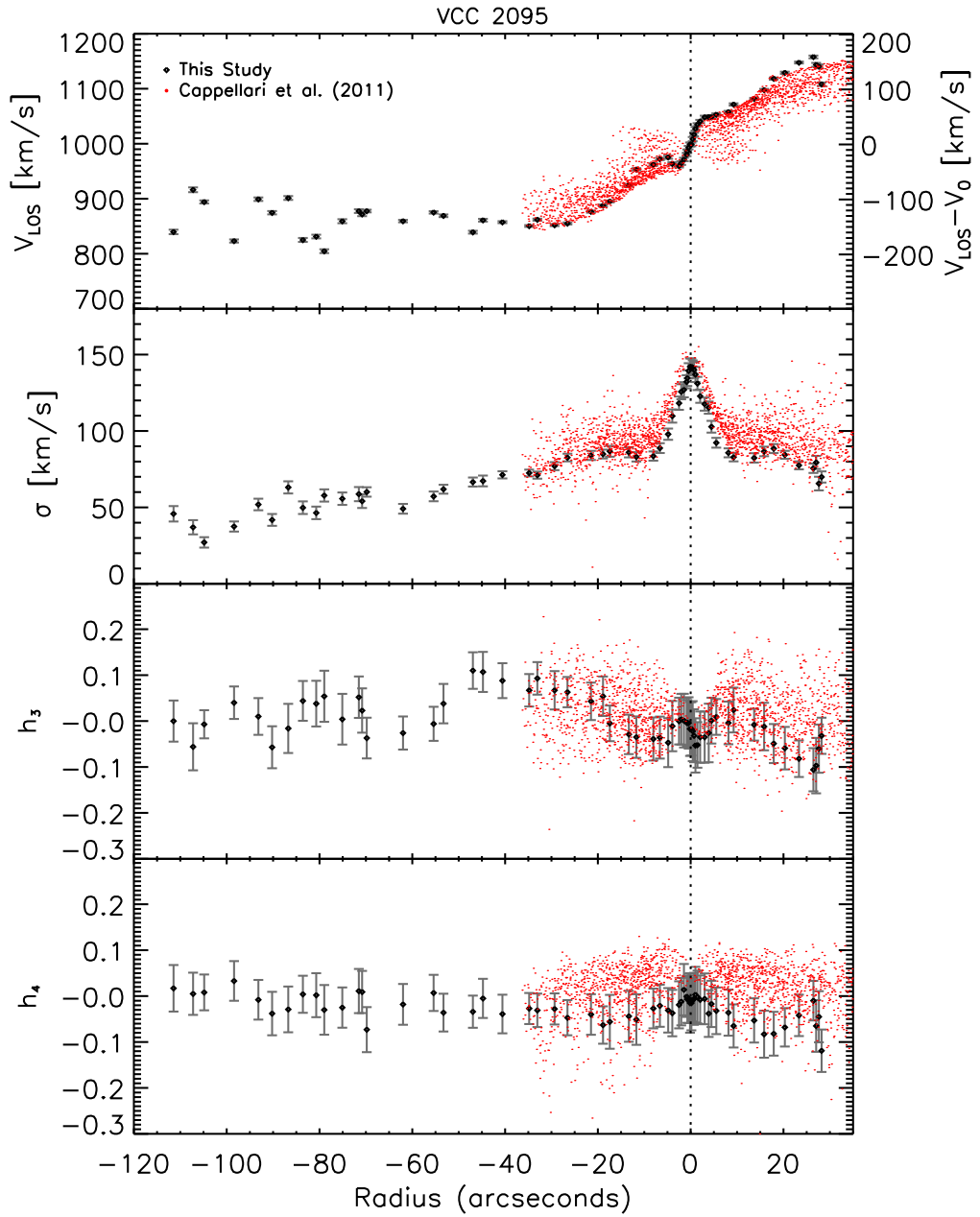
Figure A.3: The kinematics along the major-axis of VCC 2095.

This galaxy is listed as barred in RC3, and the bar signature can also be seen in the line-of-sight velocity plot. The image in Fig. 2.1 also shows the galaxy to be very edge-on, with both a thin and thick disc, and Fig. B.4 shows the effect of the multiple discs on the light profile. As a result of these factors, the light profile of the galaxy proved too complex for a simple bulge-plus-disc fit.
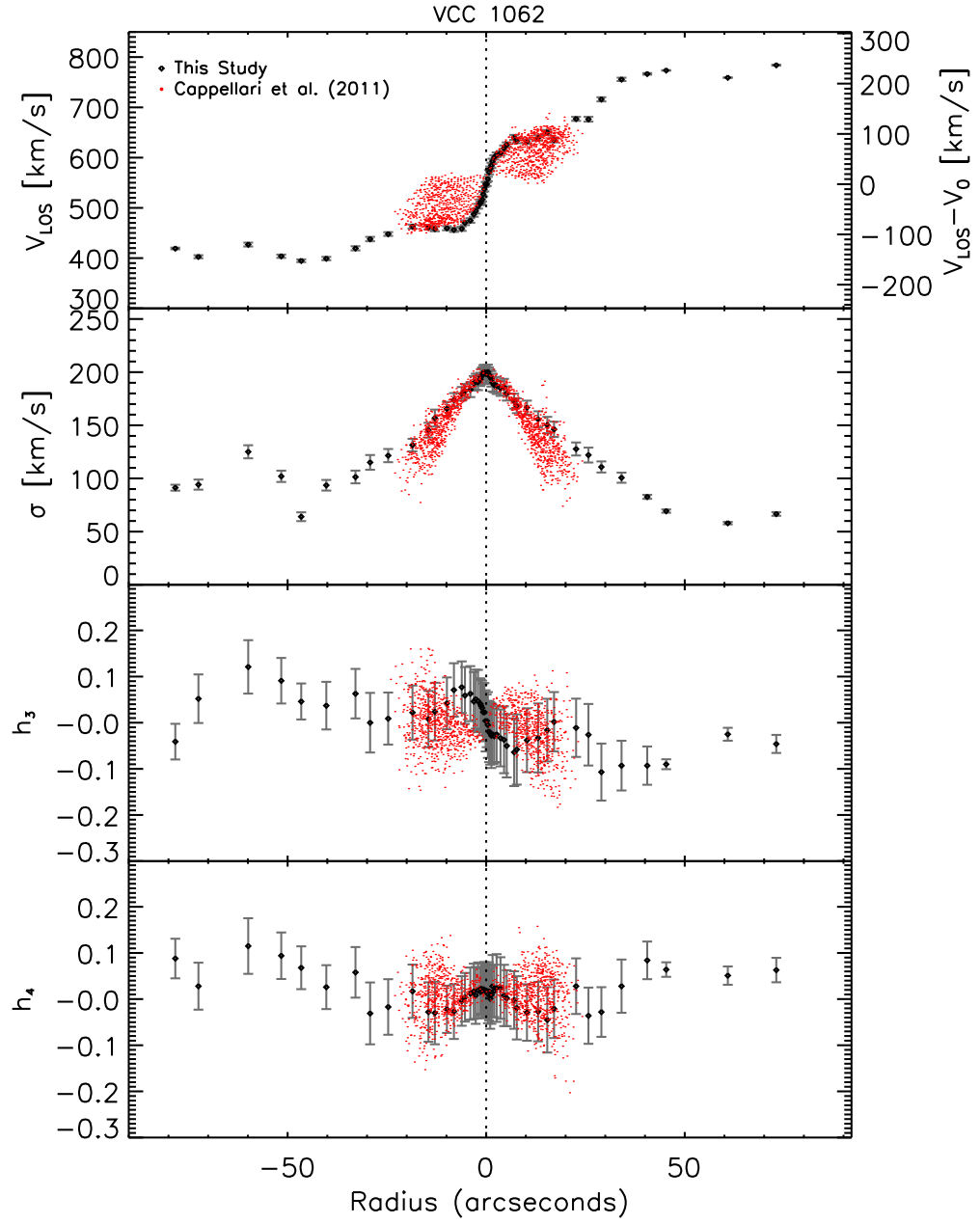
Figure A.4: The kinematics along the major-axis of VCC 1062.

This galaxy also shows evidence of a weak bar in the line-of-sight velocity and h_3 plots, and is classified as barred in RC3 and Côté et al. (2004). However, no obvious evidence of the bar was visible in the light profile, and so this galaxy was successfully decomposed.
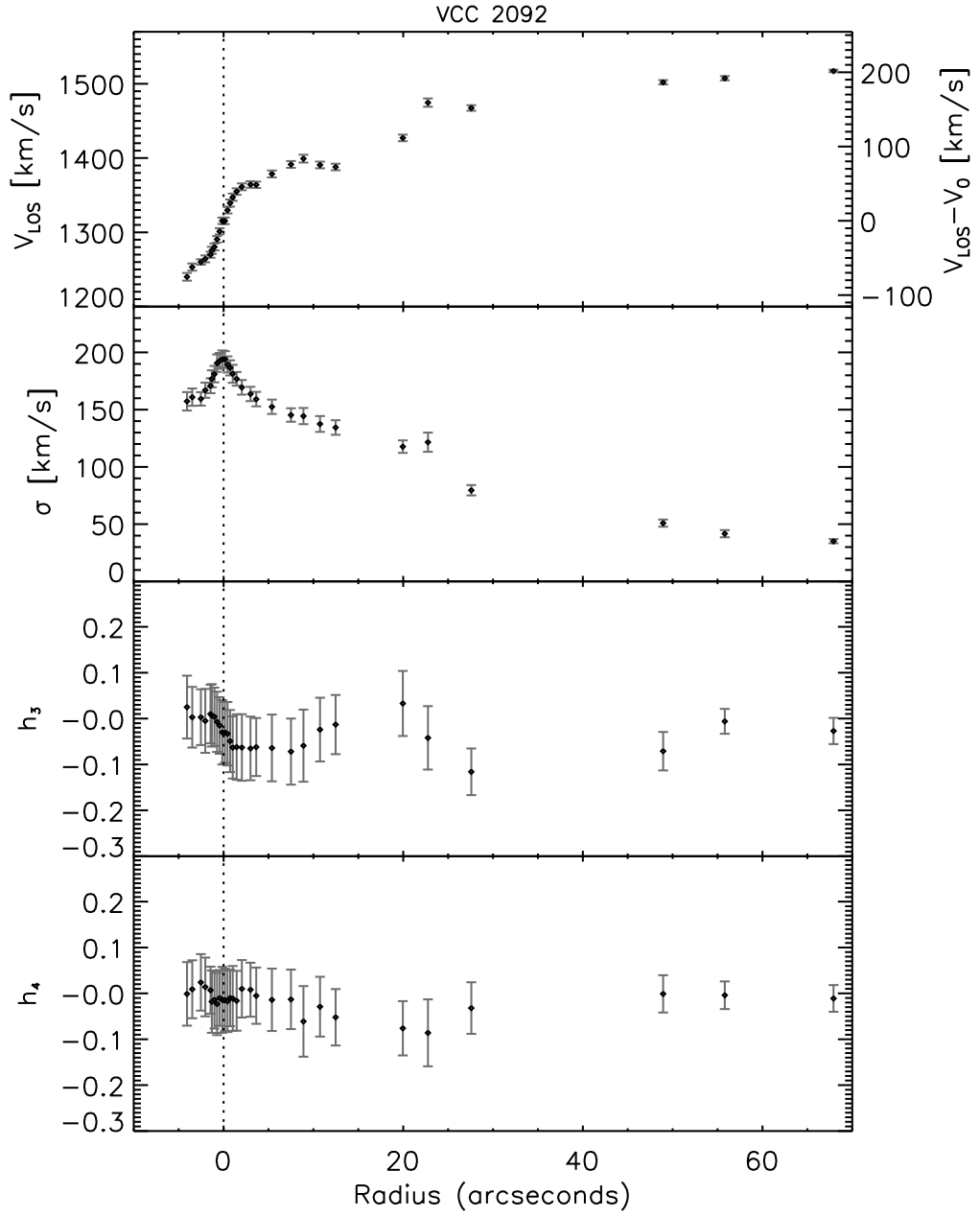
Figure A.5: The kinematics along the major-axis of VCC 2092.

A weak bar is apparent in the kinematics, and was listed in RC3 and Côté et al. (2004). This galaxy was successfully decomposed into bulge and disc components.
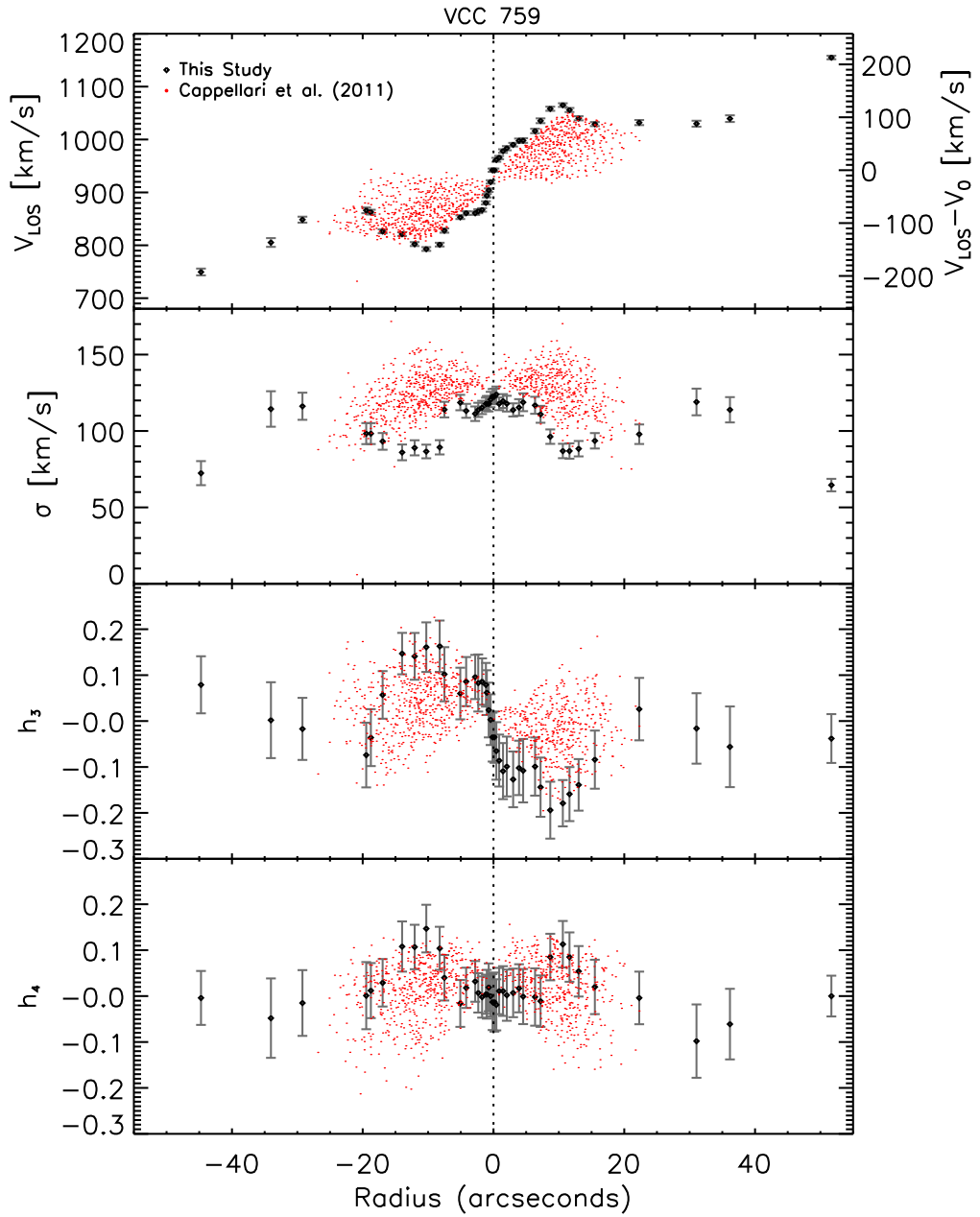
Figure A.6: The kinematics along the major-axis of VCC 759.

The kinematics for this galaxy clearly show that something strange is happening, which becomes clear when the image in Fig. 2.1 is considered. This galaxy contains a ring and a bar, and according to Ferrarese et al. (2006) there is a second nuclear ring as well. The light profile in Fig. B.4 also shows some disruption due to these additional structures. As a result, this galaxy was too complicated to be decomposed reliably with a simple bulge-plus-disc model.
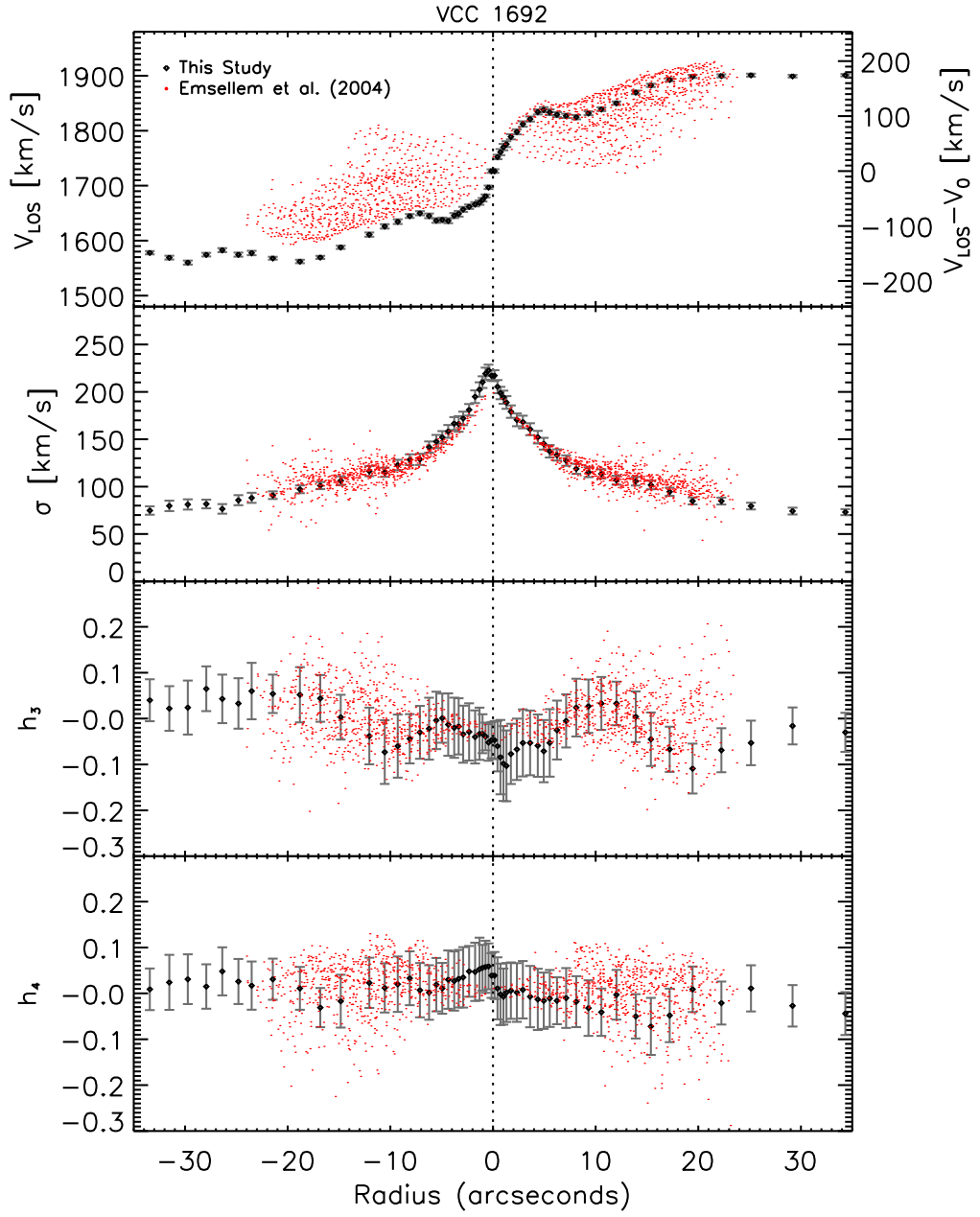
Figure A.7: The kinematics along the major-axis of VCC 1692.

This galaxy is known to have multiple components, such as a weak bar and outer and nuclear discs (van den Bosch & Emsellem, 1998). However, the light profile is not significantly affected by these structures, and so the galaxy was successfully decomposed.
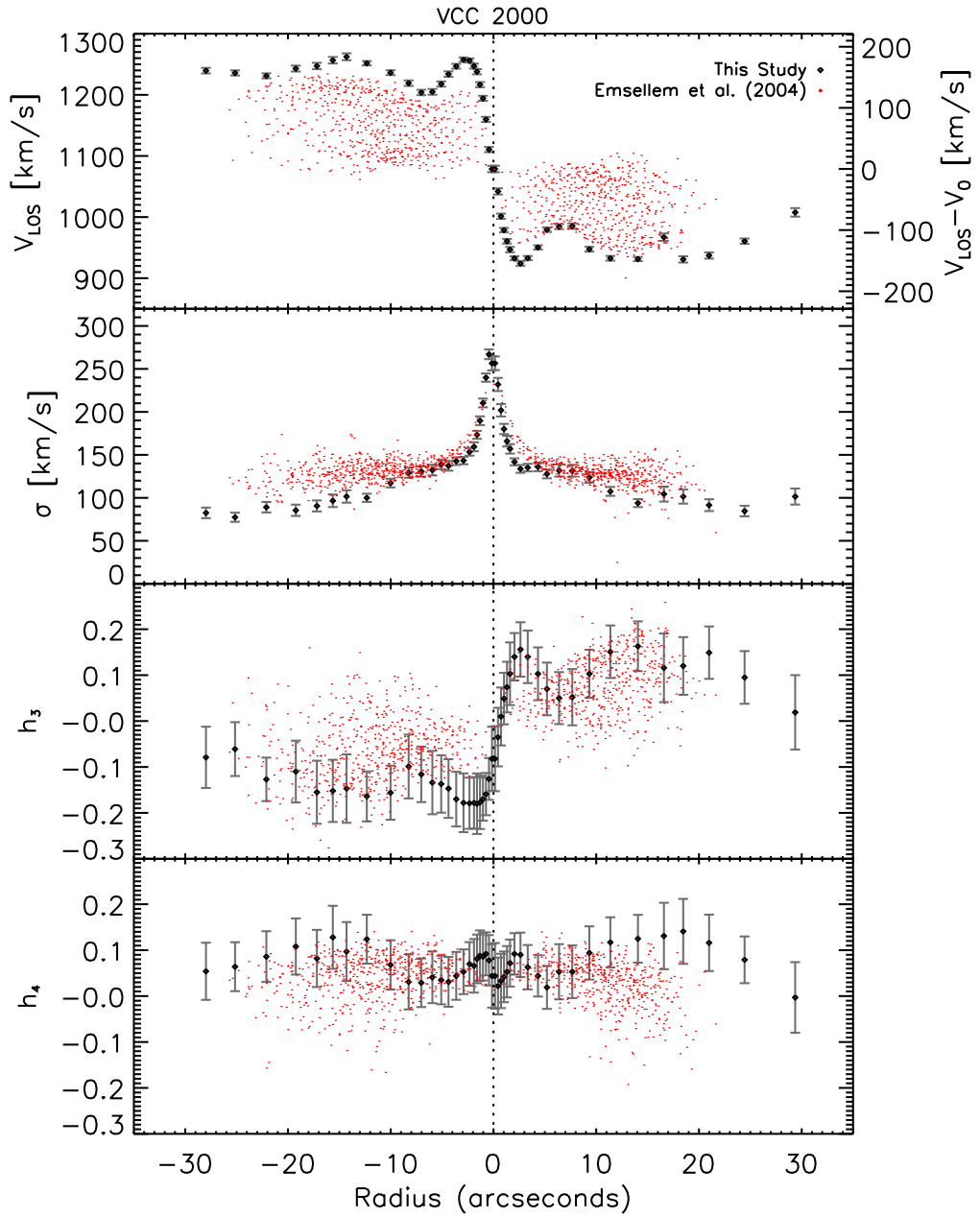
Figure A.8: The kinematics along the major-axis of VCC 2000.

The kinematics show the superposition of two rapidly rotating discs, one inside of a radius of 5 arcsec and the other outside of 7 arcsec, as described by Bender, Saglia & Gerhard (1994) and Emsellem et al. (2004). However, these features were not strong enough to significantly affect the light profile, and so the galaxy was successfully decomposed.
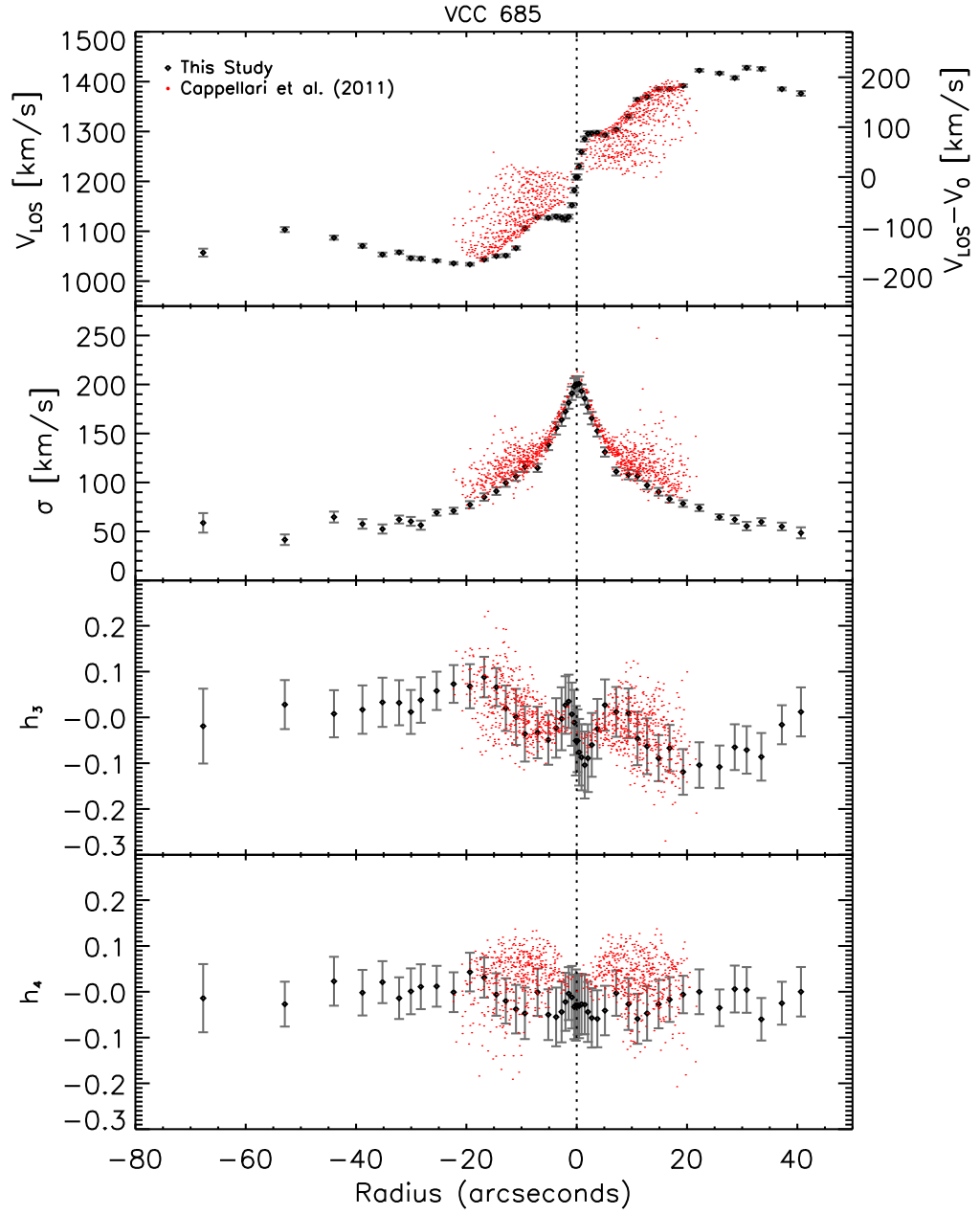
Figure A.9: The kinematics along the major-axis of VCC 685.

The kinematics reflect the rapidly rotating gas disc in the central regions of the galaxy that is decoupled from the stellar component, as described by Fisher (1997). The galaxy was successfully decomposed with a bulge-plus-disc model.
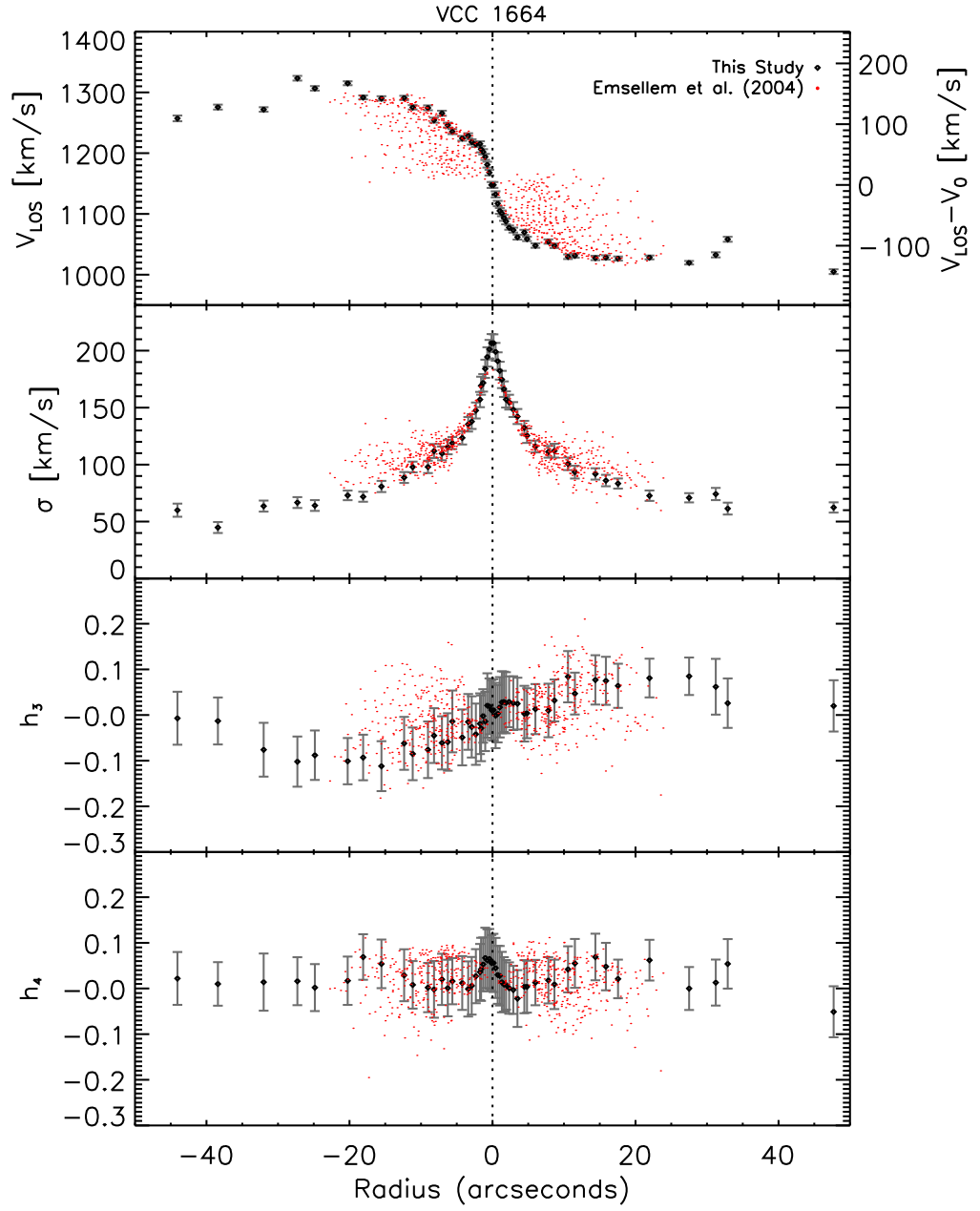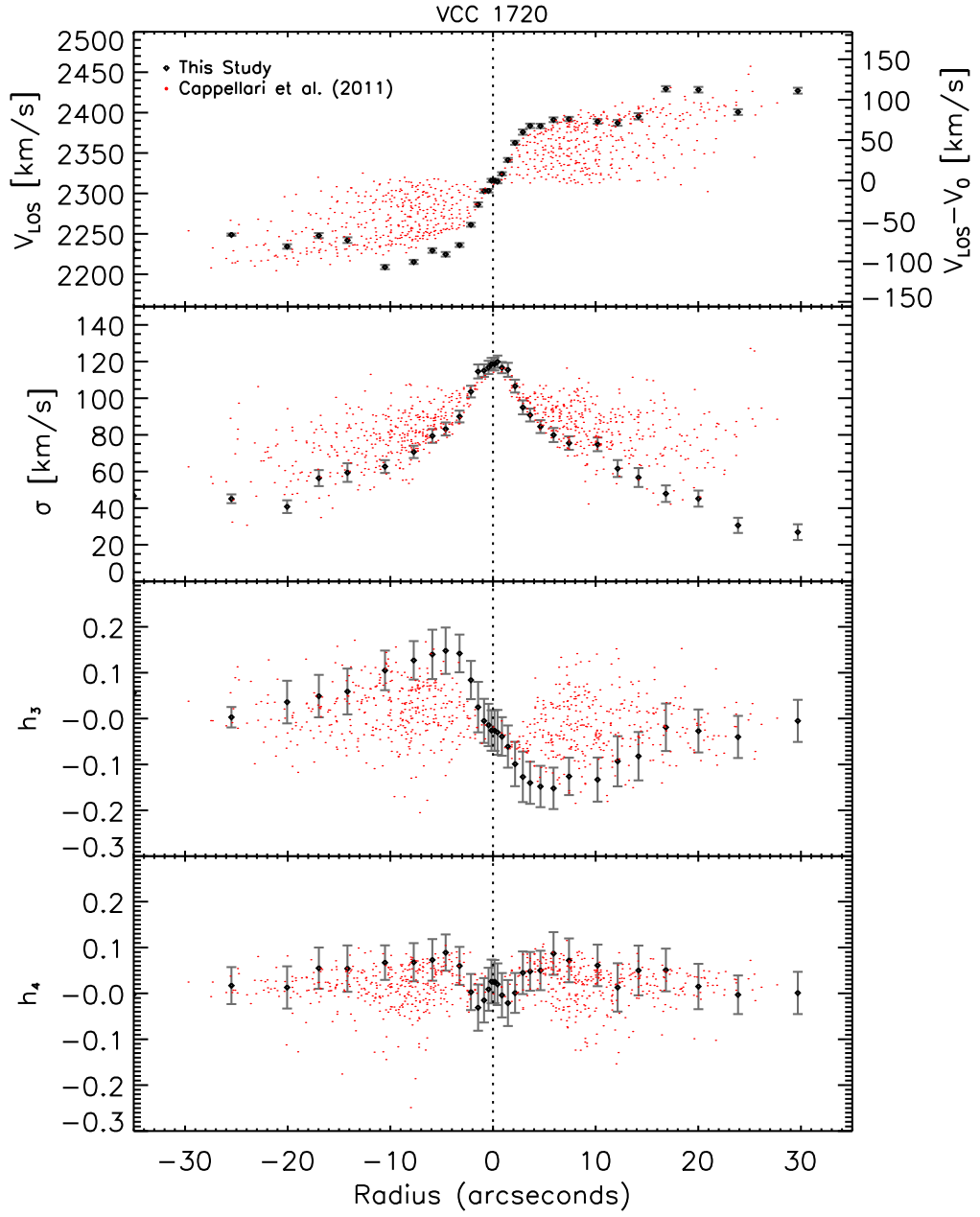
Figure A.10: The kinematics along the major-axis of VCC 1664.

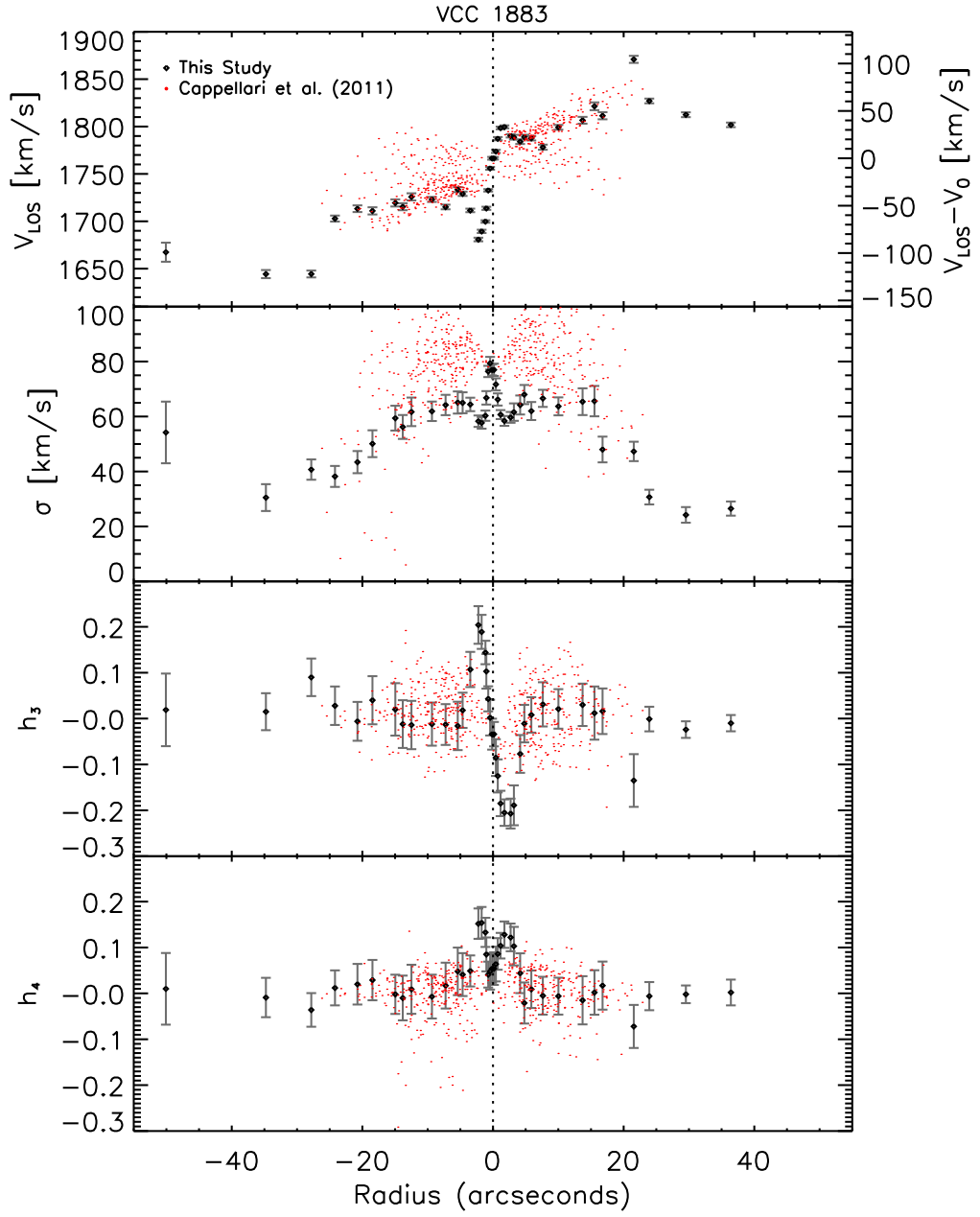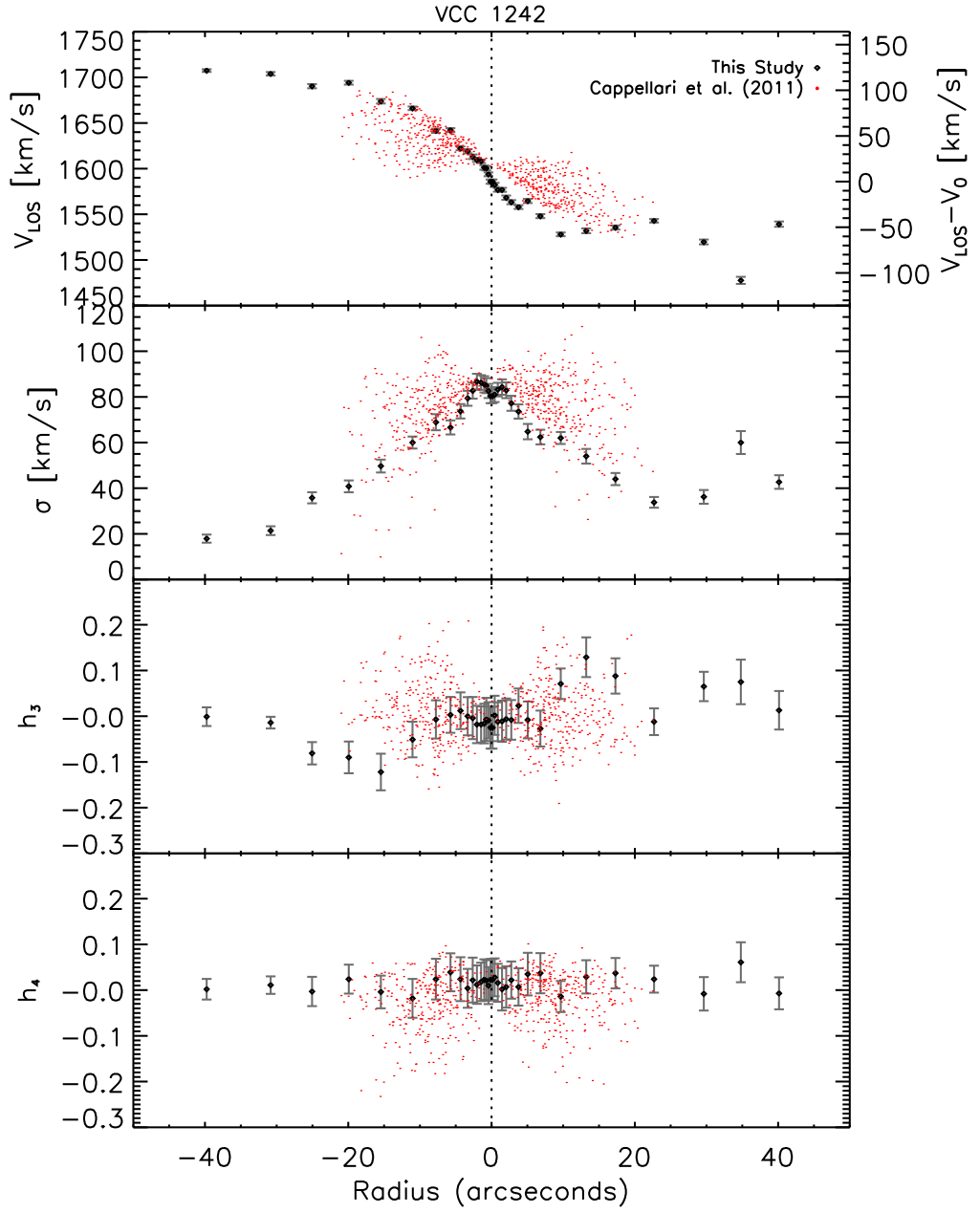This galaxy was successfully decomposed into bulge and disc components.
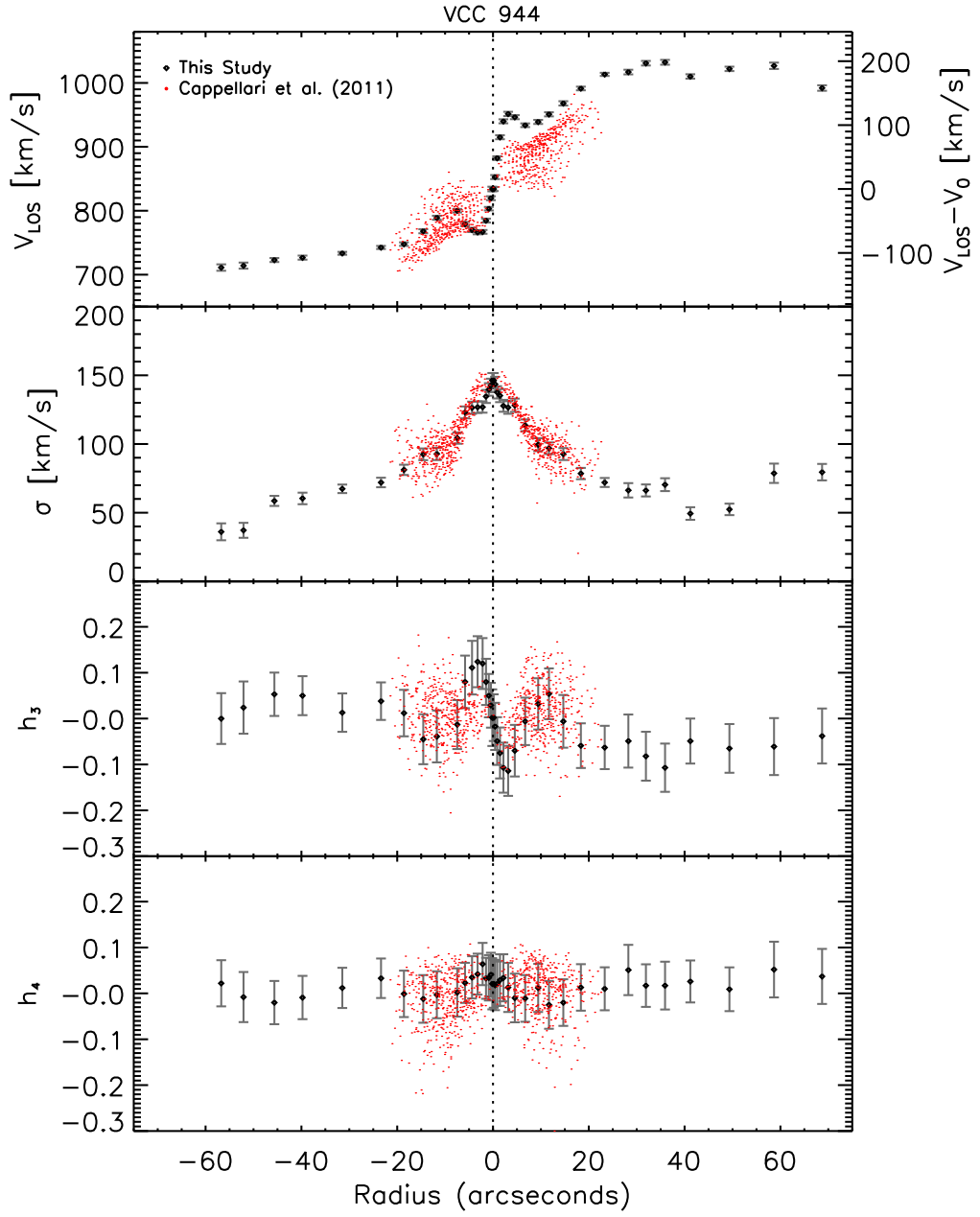
Figure A.11: The kinematics along the major-axis of VCC 944.

This galaxy shows possible indications of a weak bar, as listed in RC3, but it was not strong enough to affect the light profile. Therefore, the galaxy was successfully decomposed with a bulge-plus-disc model.
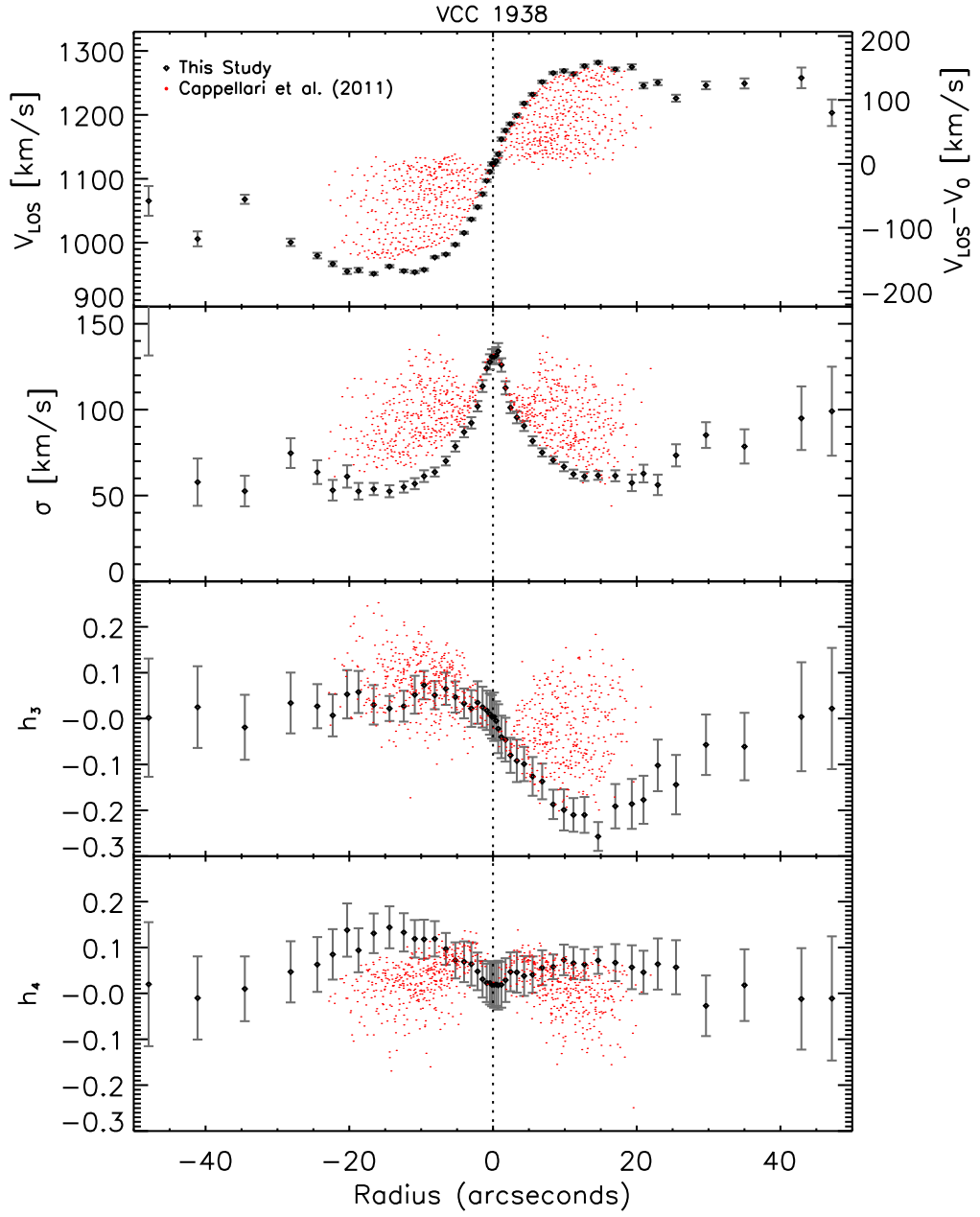
Figure A.12: The kinematics along the major-axis of VCC 1938.

The light profile for this galaxy in Fig. B.4 proved too complicated to decompose due to structures such as a thin disc embedded within a thicker disc, and dusty spiral arms within the inner disc (Ferrarese et al., 2006).

Figure A.13: The kinematics along the major-axis of VCC 1720.

This galaxy was successfully decomposed into bulge and disc components.

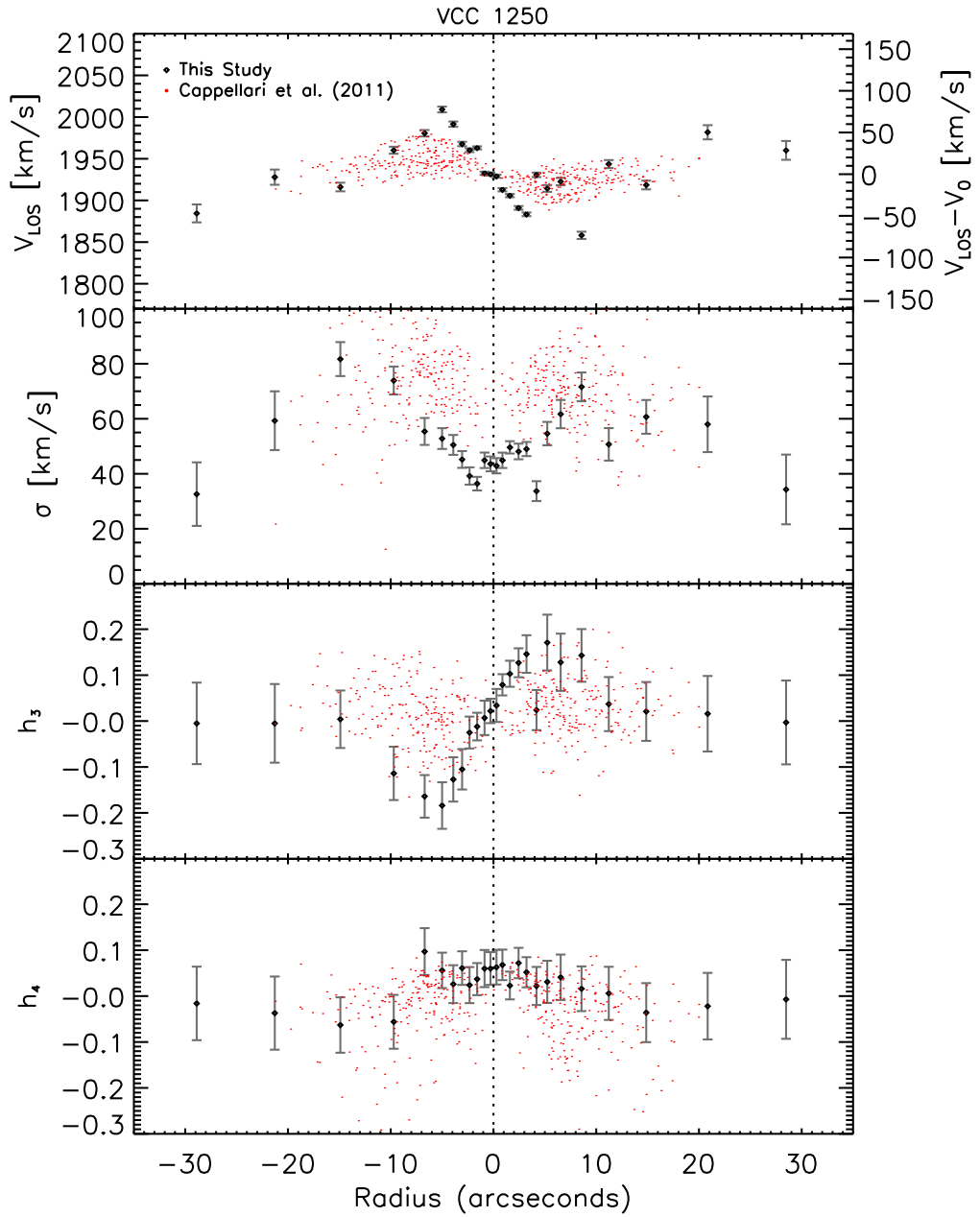**Figure A.14:** The kinematics along the major-axis of VCC 1883.

This galaxy shows evidence of a weak bar, which was identified in RC3 and Côté et al. (2004), but the light profile appeared unaffected, and so the galaxy could be successfully decomposed with a bulge-plus-disc model.

Figure A.15: The kinematics along the major-axis of VCC 1242.

This galaxy was successfully decomposed into bulge and disc components.

Figure A.16: The kinematics along the major-axis of VCC 1250.

This galaxy contains an inner, clumpy dust disc with spiral features (Ferrarese et al., 2006), which may explain the odd behaviour in the kinematics. Additionally, the spectra showed strong Hβ and [OIII] emission features in the inner regions of this galaxy, and the light profile in Fig. B.4 shows a subtle bulging at smaller radii. As a result, the galaxy could not be modelled as a bulge plus a disc.
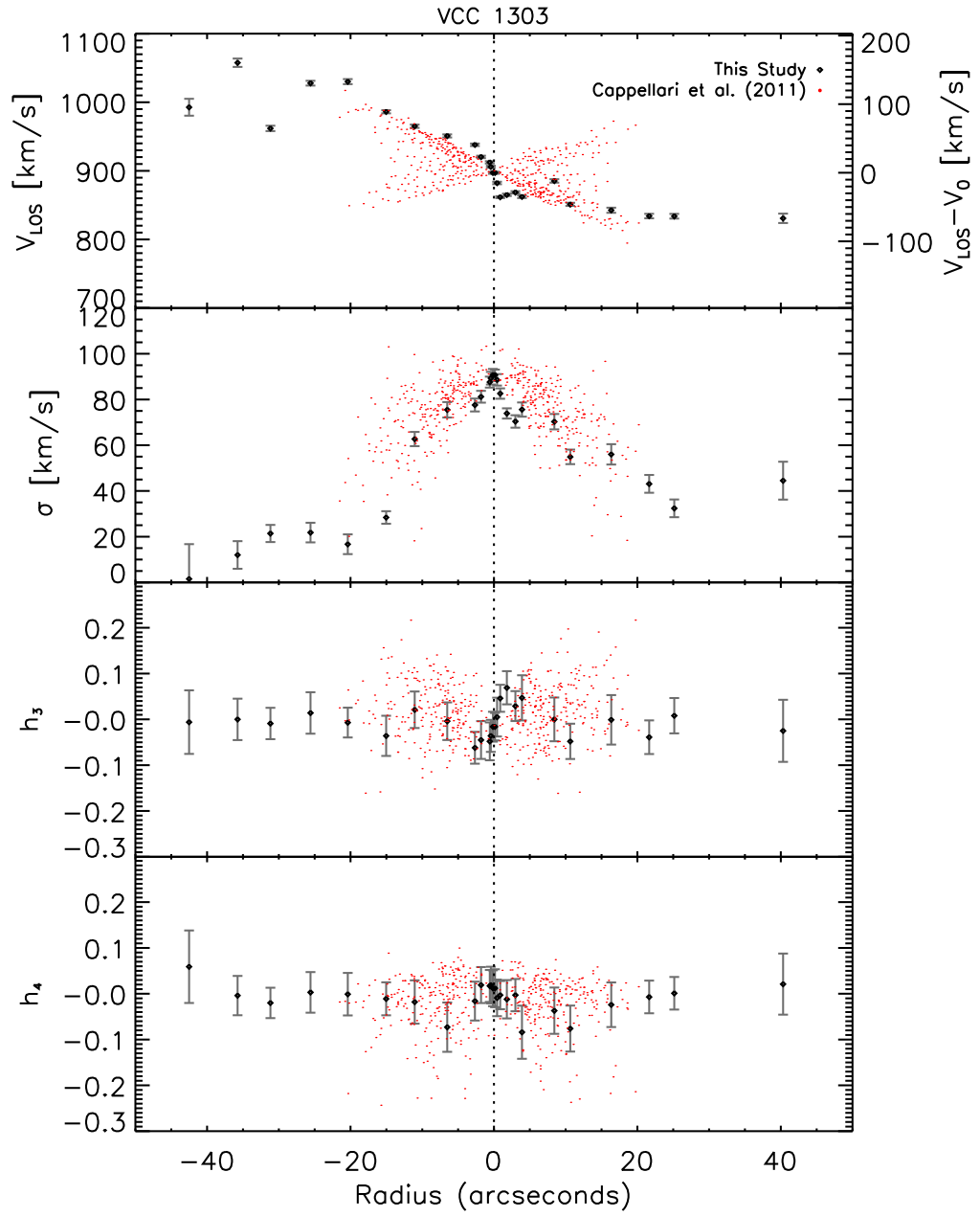
Figure A.17: The kinematics along the major-axis of VCC 1303.

This galaxy is listed as barred in RC3 and Côté et al. (2004), and evidence of a weak bar is visible in the kinematics. This galaxy was successfully decomposed into bulge and disc components.
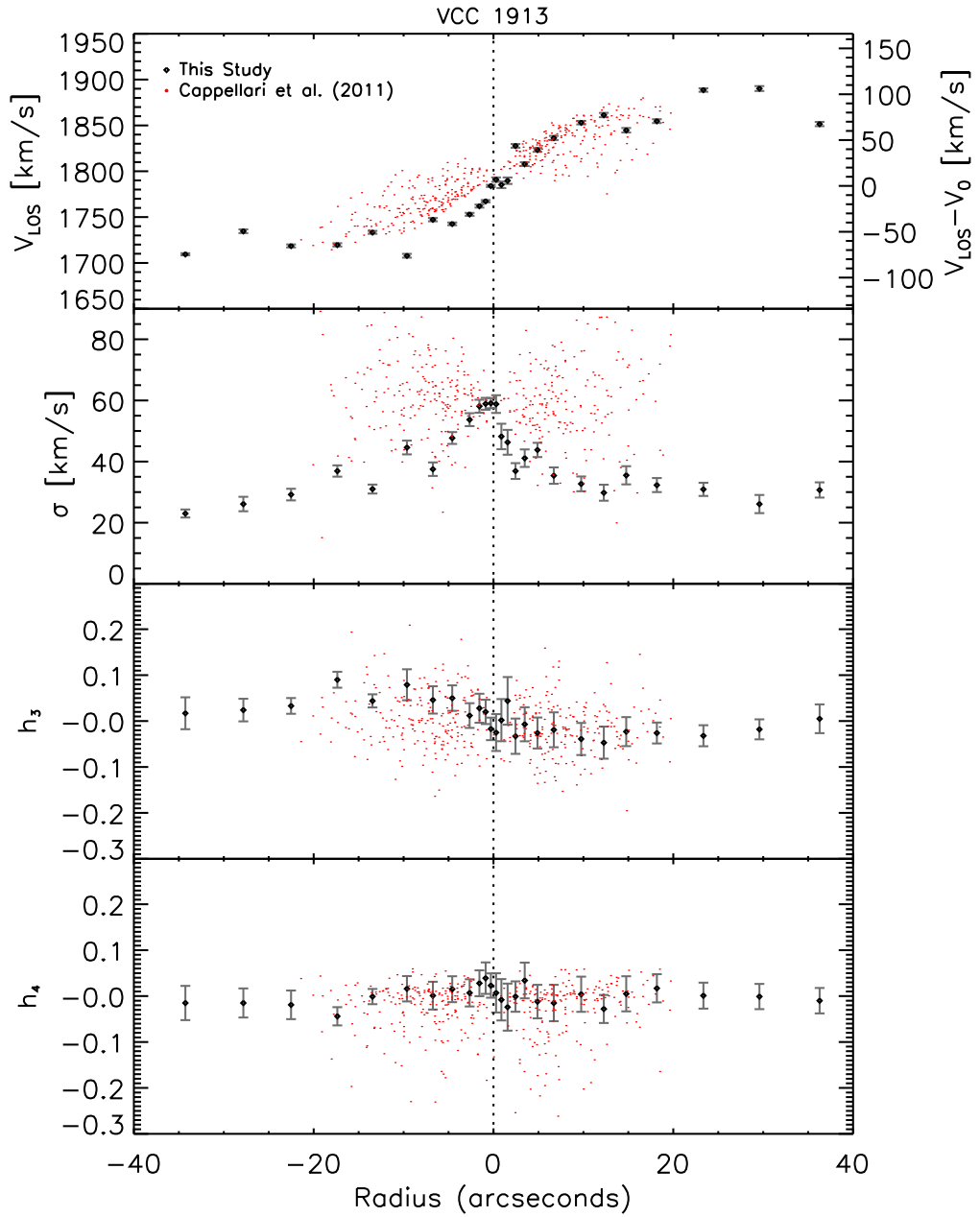
Figure A.18: The kinematics along the major-axis of VCC 1913.

The light profile of this galaxy displayed a small but sharp break in the light profile of the galaxy along both semi-major axes at a radius of around 7 arcsec, which suggests that the bulge may be truncated, as in Fig. B.4. This feature was also noted in Ferrarese et al. (2006), where the galaxy was referred to as having a 'structure-within-a-structure morphology'. Therefore, the galaxy could not be decomposed.
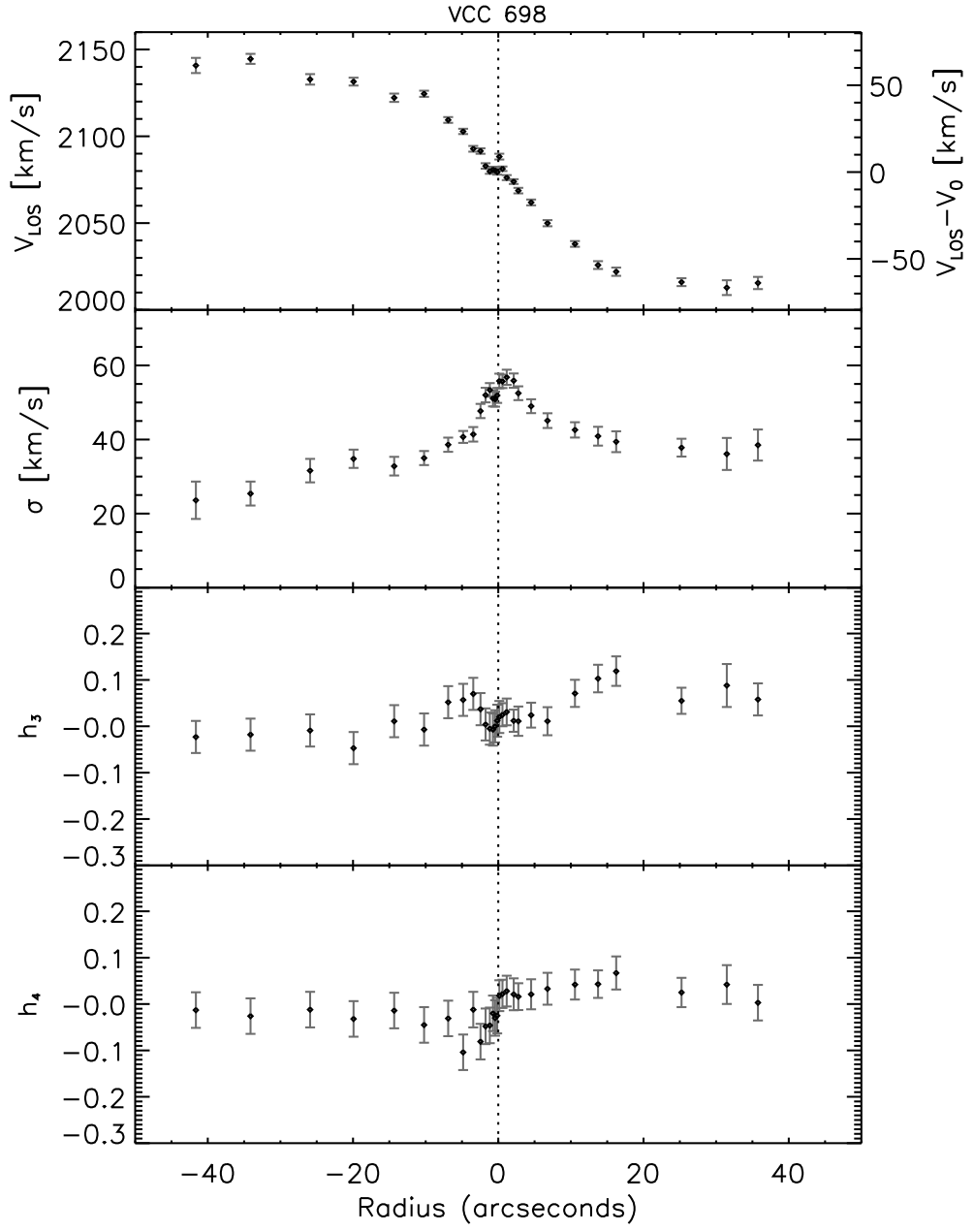
Figure A.19: The kinematics along the major-axis of VCC 698.

This galaxy was successfully decomposed into bulge and disc components.

Appendix B

Light Profile Fits

This appendix presents the best fits to the mean light profile of each galaxy that could be decomposed, with the bulge fit overplotted in blue, the disc fit in red, and the combined fit in green. In each case, the parts of the light profile that fell on the unexposed region on the CCD under the bridges were masked out, as were any stars that fell onto the slit (see for example VCC 798 and VCC 1303). The light profiles of the galaxies that couldn't be decomposed are also plotted for comparison. The galaxies were decomposed using linear flux units, whereas here they are plotted with logarithmic flux units to better illustrate the fits where applicable, or the complexities in the light profiles that may have prevented a reliable decomposition. Note that VCC 1619 (NGC 4550) has been omitted as it was decomposed using the kinematics of the two discs instead.
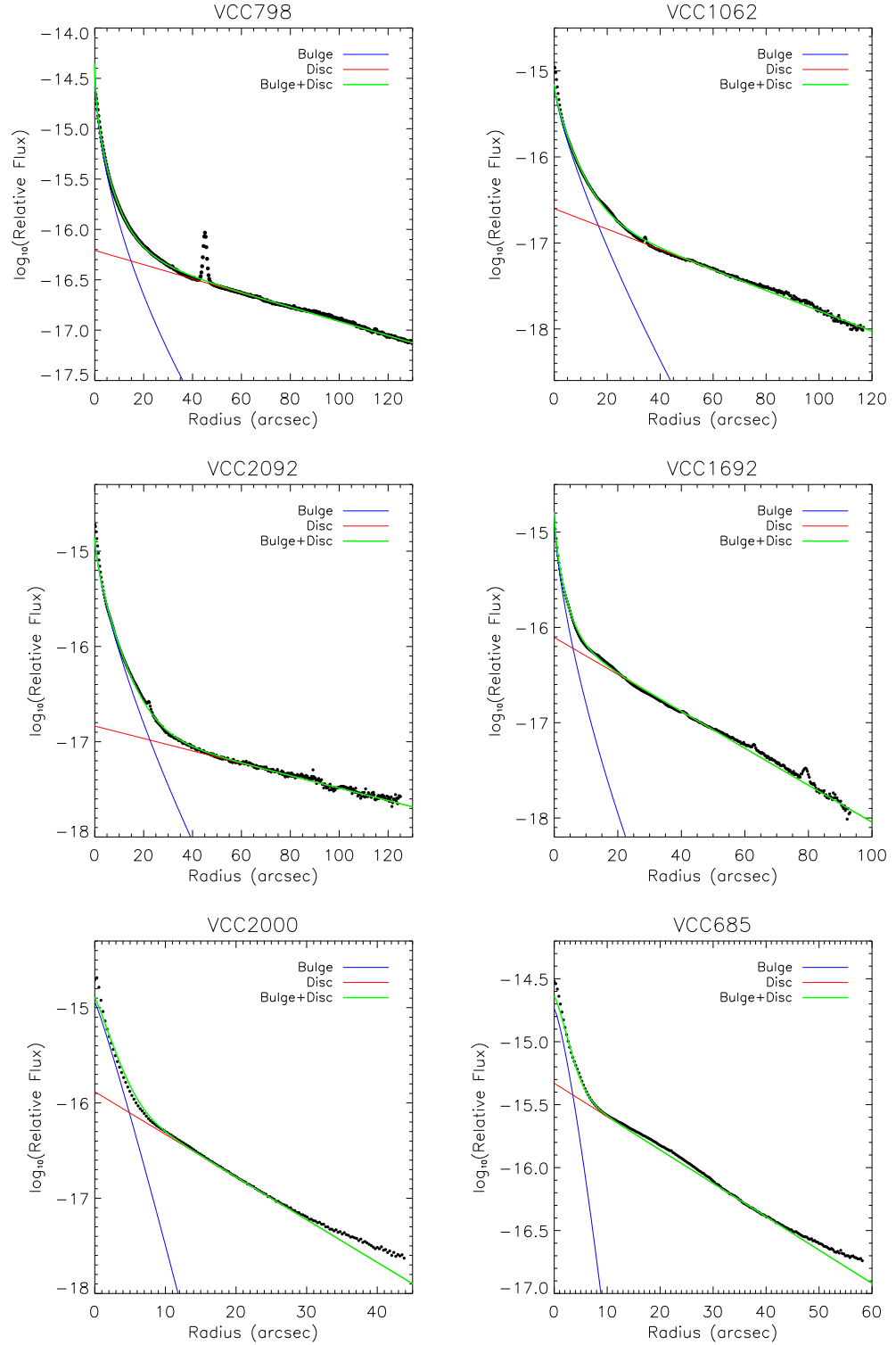
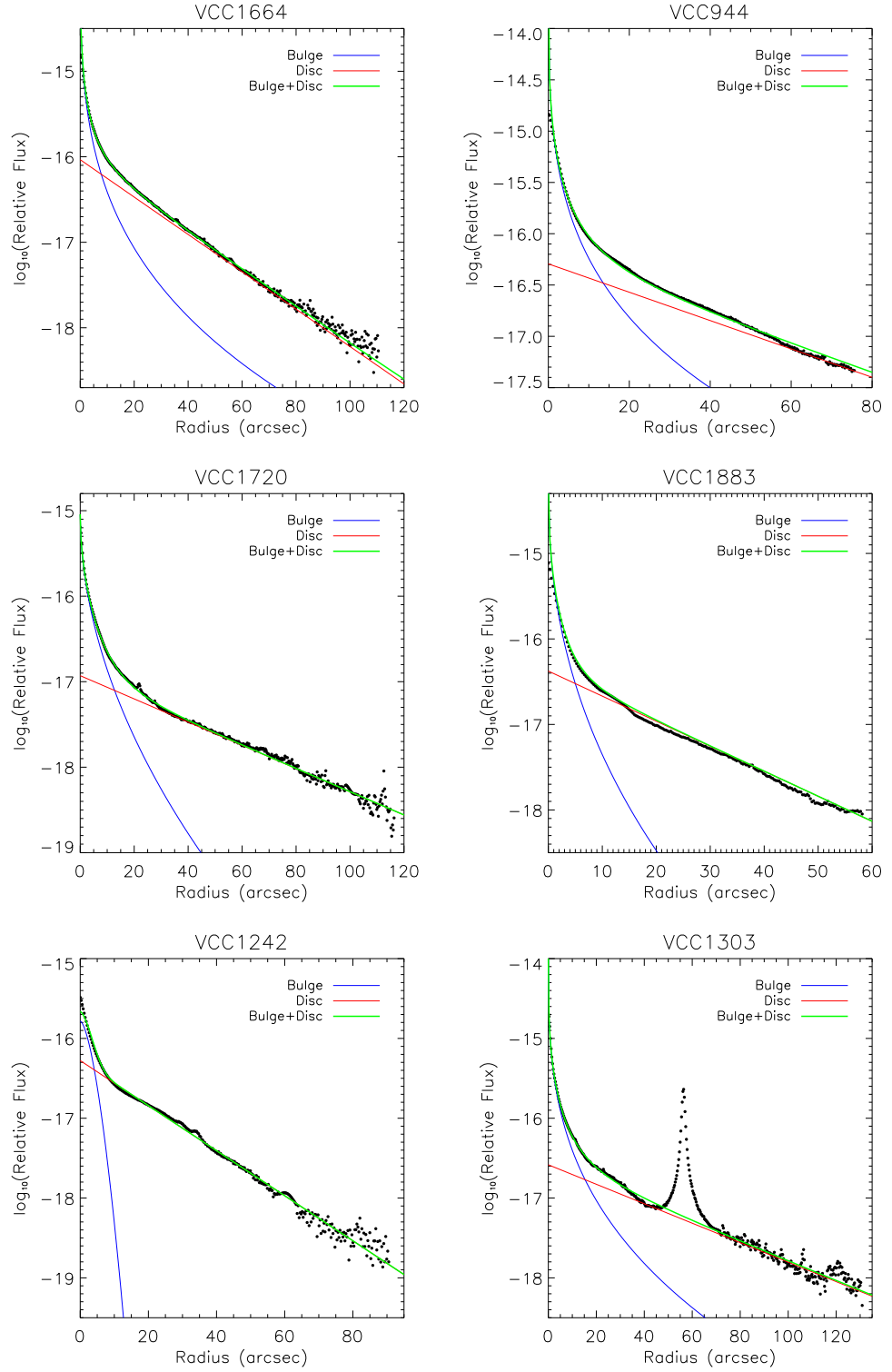**Figure B.1:** Mean light profile fits to Virgo Cluster galaxies, along with the best fit models.

Figure B.2: Mean light profile fits to Virgo Cluster galaxies, along with the best fit models.
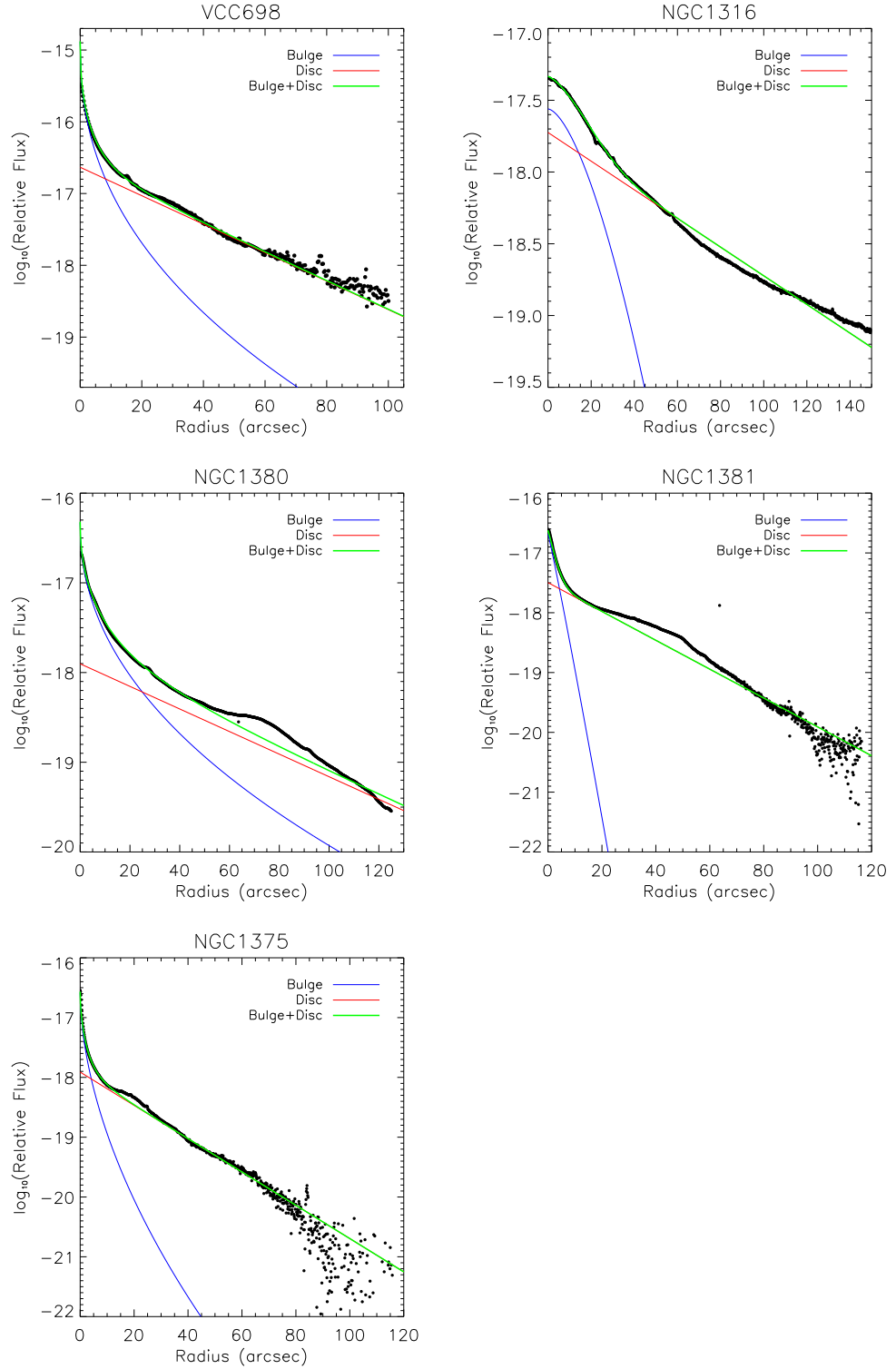
Figure B.3: Mean light profile fits to Virgo and Fornax Cluster galaxies, along with the best fit models.
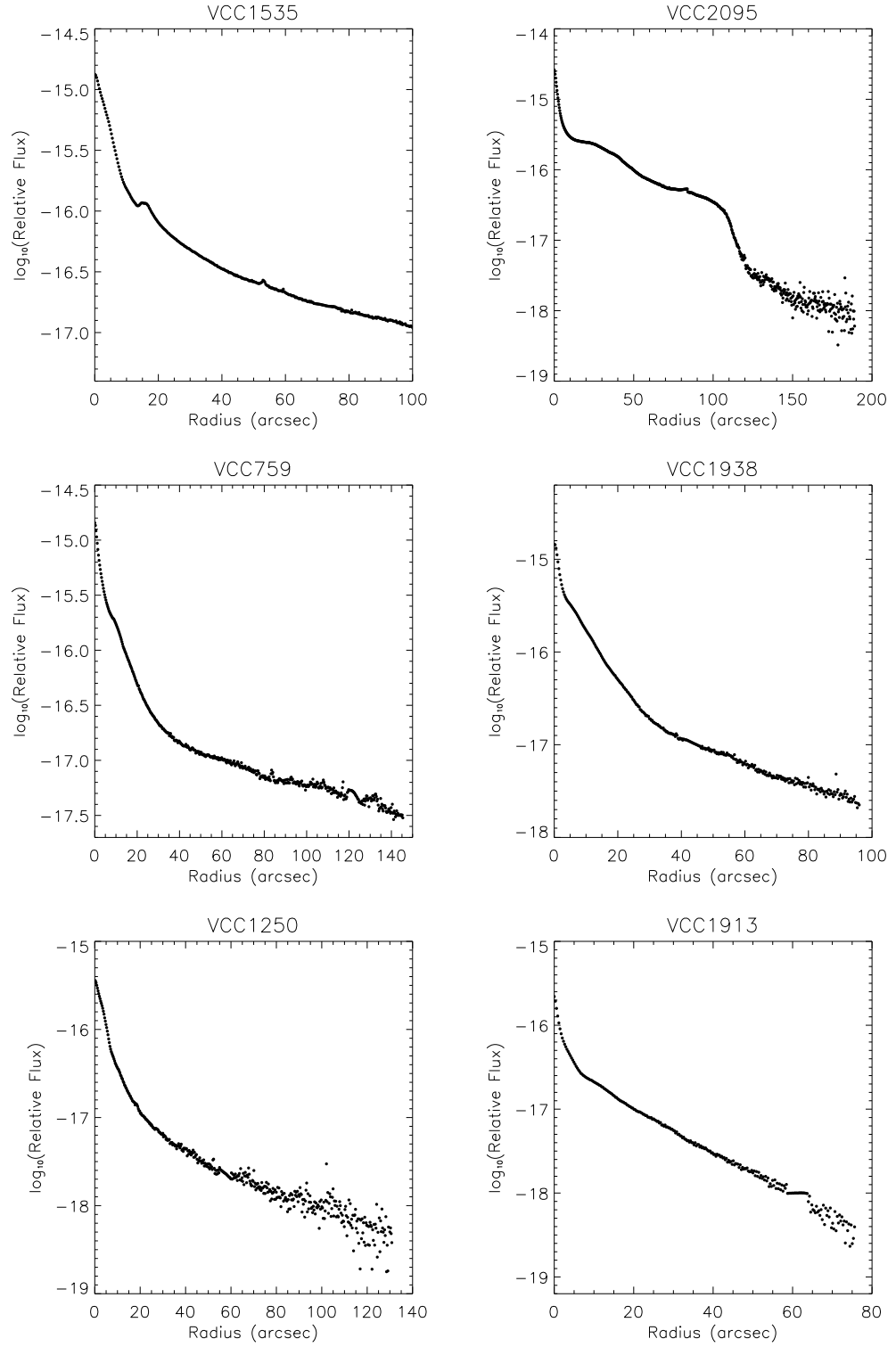
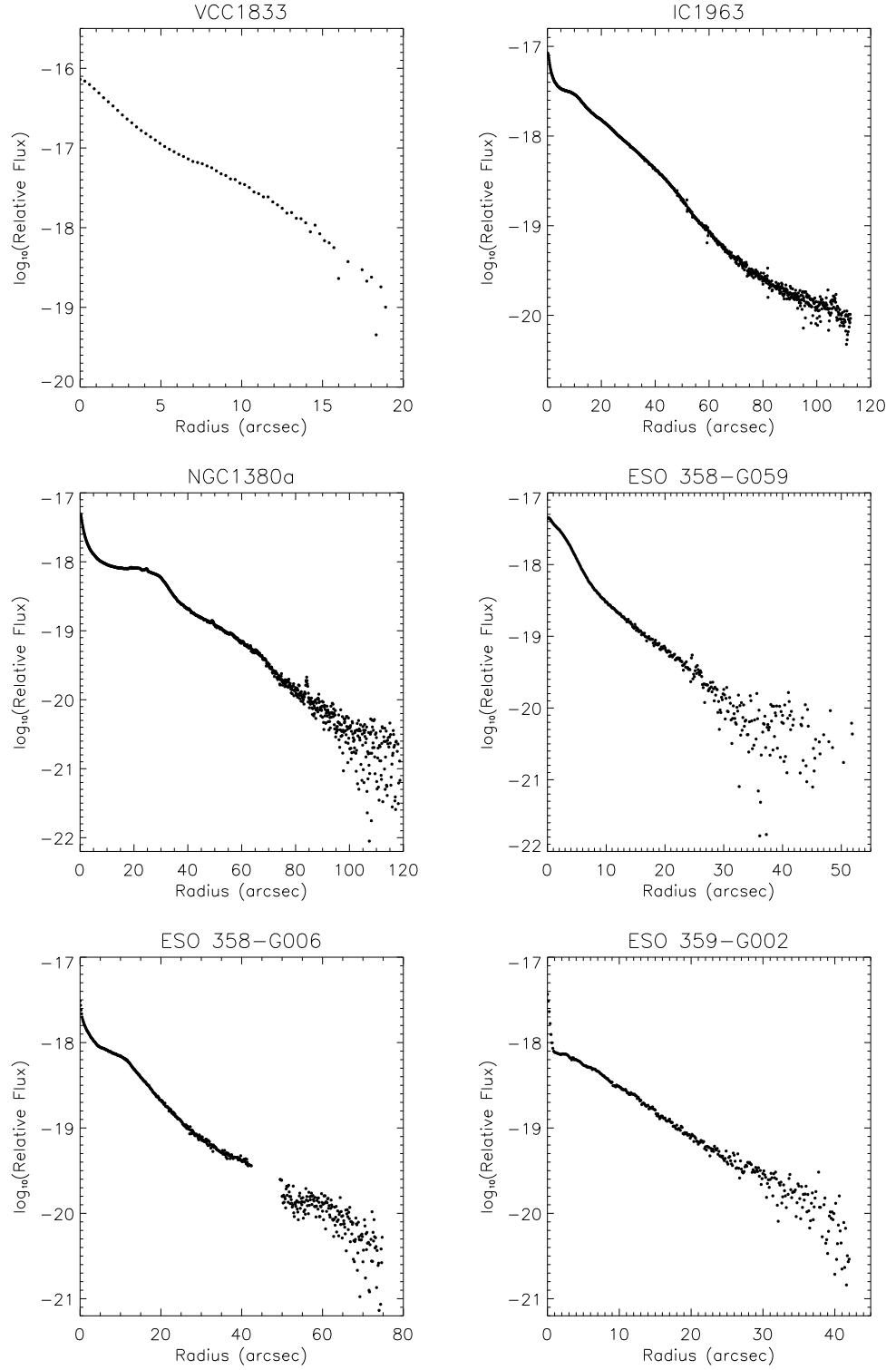**Figure B.4:** Mean light profile fits to Virgo Cluster galaxies that couldn't be decomposed.

Figure B.5: Mean light profile fits to Virgo and Fornax Cluster galaxies that couldn't be decomposed.

Bibliography

Abadi M. G., Moore B., Bower R. G., 1999, MNRAS, 308, 947

Abazajian K. N. et al., 2009, ApJS, 182, 543

Abell G. O., Corwin, Jr. H. G., Olowin R. P., 1989, ApJS, 70, 1

Aguerri J. A. L., Iglesias-Paramo J., Vilchez J. M., Muñoz-Tuñón C., 2004, AJ, 127, 1344

Aragón-Salamanca A., Bedregal A. G., Merrifield M. R., 2006, A&A, 458, 101

Athanassoula E., 2005, MNRAS, 358, 1477

Bacon R. et al., 2006, The Messenger, 124, 5

Bamford S., 2006, PhD thesis, University of Nottingham, UK

Barr J. M., Bedregal A. G., Aragón-Salamanca A., Merrifield M. R., Bamford S. P., 2007, A&A, 470, 173

Barway S., Kembhavi A., Wadadekar Y., Ravikumar C. D., Mayya Y. D., 2007, ApJ, 661, L37

Barway S., Wadadekar Y., Kembhavi A., Mayya Y. D., 2009, MNRAS, 394, 1991

Barway S., Wadadekar Y., Vaghmare K., Kembhavi A. K., 2013, MNRAS, 432, 430

Beckman J., Peletier R., Knapen J., Corradi R., Gentet L., 1996, ApJ, 467, 175

Bedregal A. G., Aragón-Salamanca A., Merrifield M. R., 2006, MNRAS, 373, 1125

Bedregal A. G., Aragón-Salamanca A., Merrifield M. R., Cardiel N., 2008, MNRAS, 387, 660

Bedregal A. G., Aragón-Salamanca A., Merrifield M. R., Milvang-Jensen B., 2006, MNRAS, 371, 1912

Bedregal A. G., Cardiel N., Aragón-Salamanca A., Merrifield M. R., 2011, MNRAS, 415, 2063

Bekki K., 1998, ApJL, 502, L133

Bekki K., Couch W. J., Shioya Y., 2002, ApJ, 577, 651

Bell E. F., de Jong R. S., 2000, MNRAS, 312, 497

Bender R., Saglia R. P., Gerhard O. E., 1994, MNRAS, 269, 785

Bertola F., Buson L. M., Zeilinger W. W., 1992, ApJ, 401, L79

Bessell M., 1990, PASP, 102, 1181

Binggeli B., Popescu C. C., Tammann G. A., 1993, A&AS, 98, 275

Binggeli B., Sandage A., Tammann G. A., 1985, AJ, 90, 1681

Binggeli B., Tammann G. A., Sandage A., 1987, AJ, 94, 251

Blakeslee J. P. et al., 2009, ApJ, 694, 556

Bothun G. D., Gregg M. D., 1990, ApJ, 350, 73

Bravo-Alfaro H., Cayatte V., van Gorkom J. H., Balkowski C., 2000, AJ, 119, 580

Bravo-Alfaro H., Cayatte V., van Gorkom J. H., Balkowski C., 2001, A&A, 379, 347

Bruzual G., Charlot S., 2003, MNRAS, 344, 1000

Bureau M., Athanassoula E., 2005, ApJ, 626, 159

Burstein D., 1979, 41, 435

Butcher H., Oemler, Jr. A., 1984, ApJ, 285, 426

Caldwell N., Rose J. A., Dendy K., 1999, AJ, 117, 140

Cappellari M., Emsellem E., 2004, PASP, 116, 138

Cappellari M. et al., 2007, MNRAS, 379, 418

Cappellari M. et al., 2011, MNRAS, 413, 813

Cardiel N., 2010, indexf: Line-strength Indices in Fully Calibrated FITS Spectra. Astrophysics Source Code Library

Carollo C. M., Stiavelli M., de Zeeuw P. T., Mack J., 1997, AJ, 114, 2366

Carroll B. W., Ostlie D. A., 1996, An Introduction to Modern Astrophysics

Cayatte V., van Gorkom J. H., Balkowski C., Kotanyi C., 1990, AJ, 100, 604

Cen R., 2014, ApJ, 781, 38

Christlein D., Zabludoff A. I., 2004, ApJ, 616, 192

Coccato L., Morelli L., Corsini E. M., Buson L., Pizzella A., Vergani D., Bertola F., 2011, MNRAS, 412, L113

Coccato L., Morelli L., Pizzella A., Corsini E. M., Buson L. M., Dalla Bontà E., 2013, A&A, 549, A3

Côté P. et al., 2004, ApJS, 153, 223

Couch W. J., Ellis R. S., Sharples R. M., Smail I., 1994, ApJ, 430, 121

Couch W. J., Sharples R. M., 1987, MNRAS, 229, 423

Crocker A. F., Jeong H., Komugi S., Combes F., Bureau M., Young L. M., Yi S., 2009, MNRAS, 393, 1255

Crowl H. H., Kenney J. D. P., van Gorkom J. H., Vollmer B., 2005, AJ, 130, 65

de Jong R. S., 1996, A&A, 313, 45

de Vaucouleurs G., 1953, MNRAS, 113, 134

de Vaucouleurs G., 1959, Handbuch der Physik, 53, 275

de Vaucouleurs G., 1991, Third Reference Catalogue of Bright Galaxies (RC3): Introduction, references, notes, and appendices, Third Reference Catalogue of Bright Galaxies (RC3): Containing Information on 23,024 Galaxies with References to Papers Published Between 1913 and 1988. Springer-Verlag

de Vaucouleurs G., de Vaucouleurs A., Corwin, Jr. H. G., Buta R. J., Paturel G., Fouqué P., 1991, Third Reference Catalogue of Bright Galaxies. Volume I: Explanations and references. Volume II: Data for galaxies between 0^h and 12^h. Volume III: Data for galaxies between 12^h and 24^h.

den Brok M. et al., 2011, MNRAS, 414, 3052

Desai V. et al., 2007, ApJ, 660, 1151

Disney M., Davies J., Phillipps S., 1989, MNRAS, 239, 939

Dressler A., 1980, ApJ, 236, 351

Dressler A., Gunn J. E., 1983, ApJ, 270, 7

Dressler A., Oemler, Jr. A., Butcher H. R., Gunn J. E., 1994, ApJ, 430, 107

Dressler A., Oemler A. J., Smail I., Barger A., Butcher H., Poggianti B. M., Sharples R. M., 1997, ApJ, 490, 577

Ellingson E., Lin H., Yee H. K. C., Carlberg R. G., 2001, ApJ, 547, 609

Emsellem E. et al., 2011, MNRAS, 414, 888

Emsellem E. et al., 2004, MNRAS, 352, 721

Evans N. W., Collett J. L., 1994, ApJ, 420, L67

Fasano G., Poggianti B. M., Couch W. J., Bettoni D., Kjærgaard P., Moles M., 2000, ApJ, 542, 673

Ferguson H. C., 1989, Ap&SS, 157, 227

Ferrarese L. et al., 2006, ApJS, 164, 334

Fisher D., 1997, AJ, 113, 950

Fisher D., Franx M., Illingworth G., 1996, ApJ, 459, 110

Franx M., Illingworth G., Heckman T., 1989, ApJ, 344, 613

Freeman K. C., 1970, ApJ, 160, 811

Fujita Y., 1998, ApJ, 509, 587

Gadotti D. A., Baes M., Falony S., 2010, MNRAS, 403, 2053

Gadotti D. A., dos Anjos S., 2001, AJ, 122, 1298

Girardi M., Biviano A., Giuricin G., Mardirossian F., Mezzetti M., 1995, ApJ, 438, 527

González J. J., 1993, PhD thesis, Univ. California, Santa Cruz

Graham A. W., 2001, AJ, 121, 820

Graham A. W., Worley C. C., 2008, MNRAS, 388, 1708

Gunn J. E., Gott J. R., 1972, ApJ, 176, 1

Hamabe M., Kormendy J., 1987, in IAU Symposium, Vol. 127, Structure and Dynamics of Elliptical Galaxies, de Zeeuw P. T., ed., p. 379

Häußler B. et al., 2013, MNRAS, 430, 330

Head J. T. C. G., Lucey J. R., Hudson M. J., Smith R. J., 2014, MNRAS

Hinz J. L., Rieke G. H., Caldwell N., 2003, AJ, 126, 2622

Hinz J. L., Rix H.-W., Bernstein G. M., 2001, AJ, 121, 683

Holmberg E., 1958, Meddelanden fran Lunds Astronomiska Observatorium Serie II, 136, 1

Hook I. M., Jørgensen I., Allington-Smith J. R., Davies R. L., Metcalfe N., Murowinski R. G., Crampton D., 2004, PASP, 116, 425

Hopkins A. M., 2004, ApJ, 615, 209

Hopkins A. M., 2007, ApJ, 654, 1175

Hoskin M., 1997, The Cambridge illustrated history of astronomy

Hubble E. P., 1926a, ApJ, 63, 236

Hubble E. P., 1926b, ApJ, 64, 321

Hubble E. P., 1927, The Observatory, 50, 276

Hubble E. P., 1929, ApJ, 69, 103

Hubble E. P., 1936, Realm of the Nebulae

Huchra J. P., 1985, in European Southern Observatory Conference and Workshop Proceedings, Vol. 20, European Southern Observatory Conference and Workshop Proceedings, Richter O.-G., Binggeli B., eds., pp. 181–200

Hudson M. J., Stevenson J. B., Smith R. J., Wegner G. A., Lucey J. R., Simard L., 2010, MNRAS, 409, 405

Jaffé Y. L. et al., 2011, MNRAS, 417, 1996

Jerjen H., 2003, A&A, 398, 63

Kannappan S. J., Guie J. M., Baker A. J., 2009, AJ, 138, 579

Kant I., 1755, Universal Natural History and Theory of Heaven

Kemp S. N., de la Fuente E., Franco-Balderas A., Meaburn J., 2005, ApJ, 624, 680

Kenney J. D. P., van Gorkom J. H., Vollmer B., 2004, AJ, 127, 3361

Kent S. M., 1985, 59, 115

Kim D.-W., Kim E., Fabbiano G., Trinchieri G., 2008, ApJ, 688, 931

Kormendy J., 1977, ApJ, 218, 333

Kormendy J., 1977, ApJ, 217, 406

Kormendy J., 1982, ApJ, 257, 75

Kormendy J., Bender R., 2012, 198, 2

Kormendy J., Illingworth G., 1982, ApJ, 256, 460

Krajnović D. et al., 2011, MNRAS, 414, 2923

Kuijken K., Fisher D., Merrifield M. R., 1996, MNRAS, 283, 543

Kuntschner H., 2000, MNRAS, 315, 184

Kuntschner H. et al., 2006, MNRAS, 369, 497

La Barbera F., de Carvalho R. R., 2009, ApJ, 699, L76

Larson R. B., Tinsley B. M., Caldwell C. N., 1980, ApJ, 237, 692

Laurikainen E., Salo H., Buta R., Knapen J. H., 2007, MNRAS, 381, 401

Lee J. C., Kennicutt R. C., Funes, José G. S. J., Sakai S., Akiyama S., 2007, ApJL, 671, L113

Levy L., Rose J. A., van Gorkom J. H., Chaboyer B., 2007, AJ, 133, 1104

Lintott C. J. et al., 2008, MNRAS, 389, 1179

MacArthur L. L., Courteau S., Bell E., Holtzman J. A., 2004, ApJS, 152, 175

Maltby D. T., Hoyos C., Gray M. E., Aragón-Salamanca A., Wolf C., 2012, MNRAS, 420, 2475

Masters K. L. et al., 2010, MNRAS, 405, 783

Mathieu A., Merrifield M. R., Kuijken K., 2002, MNRAS, 330, 251

McDonald M., Courteau S., Tully R. B., Roediger J., 2011, MNRAS, 414, 2055

Mei S. et al., 2007, ApJ, 655, 144

Michard R., Poulain P., 2000, A&AS, 141, 1

Mihos J. C., Hernquist L., 1994, ApJ, 425, L13

Möllenhoff C., 2004, A&A, 415, 63

Möllenhoff C., Heidt J., 2001, A&A, 368, 16

Möllenhoff C., Popescu C. C., Tuffs R. J., 2006, A&A, 456, 941

Moore B., Lake G., Katz N., 1998, ApJ, 495, 139

Moore B., Lake G., Quinn T., Stadel J., 1999, MNRAS, 304, 465

Neistein E., Maoz D., Rix H.-W., Tonry J. L., 1999, AJ, 117, 2666

Noordermeer E. et al., 2008, MNRAS, 384, 943

Norris M. A., Sharples R. M., Kuntschner H., 2006, MNRAS, 367, 815

Oohama N., Okamura S., Fukugita M., Yasuda N., Nakamura O., 2009, ApJ, 705, 245

Oosterloo T., van Gorkom J., 2005, A&A, 437, L19

Pastrav B. A., Popescu C. C., Tuffs R. J., Sansom A. E., 2013, A&A, 553, A80

Peletier R. F., Balcells M., 1996, AJ, 111, 2238

Peng C. Y., Ho L. C., Impey C. D., Rix H.-W., 2002, AJ, 124, 266

Peng C. Y., Ho L. C., Impey C. D., Rix H.-W., 2010, AJ, 139, 2097

Poggianti B. M. et al., 2009, ApJ, 693, 112

Poggianti B. M. et al., 2001, ApJ, 563, 118

Poggianti B. M., Smail I., Dressler A., Couch W. J., Barger A. J., Butcher H., Ellis R. S., Oemler, Jr. A., 1999, ApJ, 518, 576

Poggianti B. M. et al., 2006, ApJ, 642, 188

Pompei E., Natali G., 1997, A&AS, 124, 129

Postman M. et al., 2005, ApJ, 623, 721

Pracy M. B. et al., 2013, MNRAS, 432, 3131

Prochaska Chamberlain L., Courteau S., McDonald M., Rose J., 2011, MNRAS, 412, 423

Prugniel P., Soubiran C., 2001, A&A, 369, 1048

Puerari I., Pfenniger D., 2001, Ap&SS, 276, 909

Rasmussen J., Ponman T. J., Mulchaey J. S., 2006, MNRAS, 370, 453

Rawle T. D., Lucey J. R., Smith R. J., Head J. T. C. G., 2013, MNRAS, 433, 2667

Reynolds C. S., Ward M. J., Fabian A. C., Celotti A., 1997, MNRAS, 2911, 403

Riess A. G., Fliri J., Valls-Gabaud D., 2012, ApJ, 745, 156

Rix H.-W., Franx M., Fisher D., Illingworth G., 1992, ApJ, 400, L5

Roche N., Bernardi M., Hyde J., 2010, MNRAS, 407, 1231

Rodríguez Del Pino B., Bamford S. P., Aragón-Salamanca A., Milvang-Jensen B., Merrifield M. R., Balcells M., 2014, MNRAS, 438, 1038

Rosse T. E. O., 1850, Royal Society of London Philosophical Transactions Series I, 140, 499

Rubin V. C., Graham J. A., Kenney J. D. P., 1992, ApJ, 394, L9

Sánchez S. F. et al., 2012, A&A, 538, A8

Sánchez-Blázquez P. et al., 2006, MNRAS, 371, 703

Sánchez-Blázquez P., Rosales-Ortega F., Diaz A., Sánchez S. F., 2014, MNRAS, 437, 1534

Sarzi M. et al., 2006, MNRAS, 366, 1151

Sérsic J. L., 1968, Atlas de Galaxias Australes. Cordoba: Observatorio Astronomico

Shapley H., 1917, PNAS, 3, 479

Shapley H., Curtis H. D., 1921, Bulletin of the National Research Council, 2, 171

Sil'Chenko O. K., 2006, Astronomical and Astrophysical Transactions, 25, 199

Skrutskie M. F. et al., 2006, AJ, 131, 1163

Smail I., Kuntschner H., Kodama T., Smith G. P., Packham C., Fruchter A. S., Hook R. N., 2001, MNRAS, 323, 839

Smith G. P., Treu T., Ellis R. S., Moran S. M., Dressler A., 2005, ApJ, 620, 78

Stone R. P. S., Baldwin J. A., 1983, MNRAS, 204, 347

Stoughton C. et al., 2002, AJ, 123, 485

Suh H., Jeong H., Oh K., Yi S. K., Ferreras I., Schawinski K., 2010, ApJS, 187, 374

Sun M., Donahue M., Voit G. M., 2007, ApJ, 671, 190

Terndrup D. M., Davies R. L., Frogel J. A., DePoy D. L., Wells L. A., 1994, ApJ, 432, 518

Thakar A. R., Ryden B. S., 1996, ApJ, 461, 55

Thakar A. R., Ryden B. S., 1998, ApJ, 506, 93

Thomas D., Maraston C., Bender R., 2003, MNRAS, 339, 897

Thomas D., Maraston C., Bender R., Mendes de Oliveira C., 2005, ApJ, 621, 673

Tonry J. L., Dressler A., Blakeslee J. P., Ajhar E. A., Fletcher A. B., Luppino G. A., Metzger M. R., Moore C. B., 2001, ApJ, 546, 681

Toomre A., 1977a, in Evolution of Galaxies and Stellar Populations, Tinsley B. M., Larson D. Campbell R. B. G., eds., p. 401

Toomre A., 1977b, ARA&A, 15, 437

Trager S. C., Faber S. M., Worthey G., González J. J., 2000, AJ, 119, 1645

Trager S. C., Faber S. M., Worthey G., González J. J., 2000, AJ, 120, 165

Tran K.-V. H., Franx M., Illingworth G., Kelson D. D., van Dokkum P., 2003, ApJ, 599, 865

Trujillo I., Asensio Ramos A., Rubiño-Martín J. A., Graham A. W., Aguerri J. A. L., Cepa J., Gutiérrez C. M., 2002, MNRAS, 333, 510

Tully R. B., Fisher J. R., 1977, A&A, 54, 661

van den Bergh S., 1976, ApJ, 206, 883

van den Bosch F. C., Emsellem E., 1998, MNRAS, 298, 267

Varela J., Moles M., Márquez I., Galletta G., Masegosa J., Bettoni D., 2004, A&A, 420, 873

Vazdekis A., Sánchez-Blázquez P., Falcón-Barroso J., Cenarro A. J., Beasley M. A., Cardiel N., Gorgas J., Peletier R. F., 2010, MNRAS, 404, 1639

Veilleux S., Bland-Hawthorn J., Cecil G., Tully R. B., Miller S. T., 1999, ApJ, 520, 111

Vika M., Bamford S. P., Häußler B., Rojas A. L., Borch A., Nichol R. C., 2013, MNRAS, 435, 623

Vollmer B., 2003, A&A, 398, 525

Vollmer B., Balkowski C., Cayatte V., van Driel W., Huchtmeier W., 2004a, A&A, 419, 35

Vollmer B., Beck R., Kenney J. D. P., van Gorkom J. H., 2004b, AJ, 127, 3375

Vollmer B., Cayatte V., Boselli A., Balkowski C., Duschl W. J., 1999, A&A, 349, 411

White S. D. M., 1997, in The Evolution of the Universe: report of the Dahlem Workshop on the Evolution of the Universe, Borner G., Gottlober S., eds., p. 227

Williams M. J., Bureau M., Cappellari M., 2010, MNRAS, 409, 1330

Wolf C. et al., 2009, MNRAS, 393, 1302

Worthey G., 1994, ApJS, 95, 107

Worthey G., Faber S. M., González J. J., Burstein D., 1994, ApJS, 94, 687

Worthey G., Ottaviani D. L., 1997, ApJS, 111, 377

Wright T., 1750, An original theory or new hypothesis of the Universe